Cell

Resource

Multimodal clocks of human aging

Graphical abstract

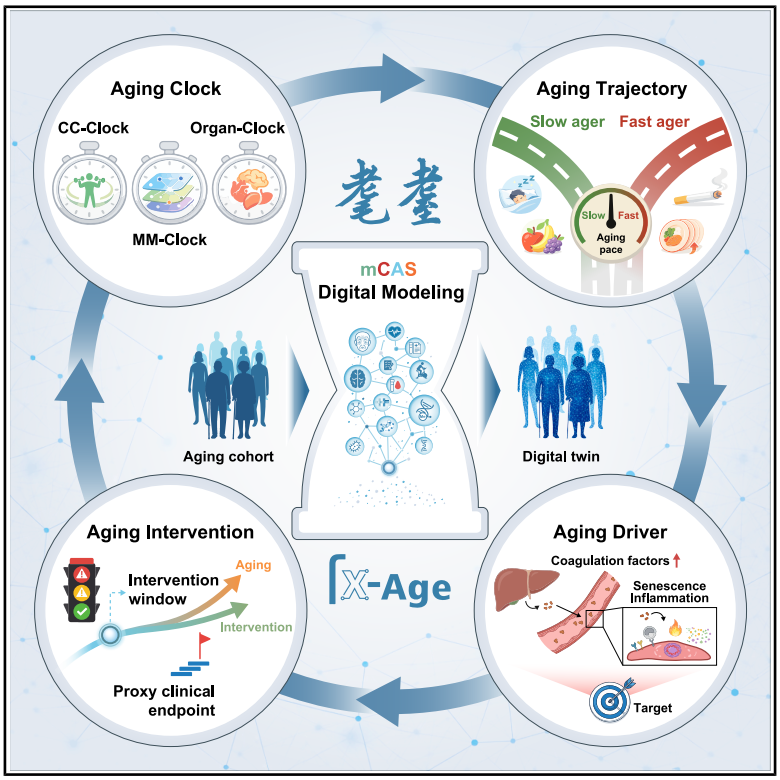

Highlights

- Multimodal clocks define a quantitative framework for human aging
- Aging biomarkers and trajectories are highly conserved across multiple centers
- Plasma proteomic signals provide a compact, sensitive readout of systemic aging
- Coagulation-factor accumulation is identified as both a biomarker and driver of aging

Authors

Jiaming Li, Beier Jiang, Wei Zhang, ..., Guoguang Zhao, Weiqi Zhang, Guang-Hui Liu

Correspondence

peigang@tongji.edu.cn (G.P.), qujing@ioz.ac.cn (J.Q.), ndyfy00266@ncu.edu.cn (W.Z.), pujun310@hotmail.com (J.P.), fengzhang@wmu.edu.cn (F.Z.), ggzhao@vip.sina.com (G.Z.), zhangwq@big.ac.cn (W.Z.), ghliu@ioz.ac.cn (G.-H.L.)

In brief

A multidimensional framework established to quantify human aging reveals highly conserved aging biomarkers and trajectories across multiple centers. By decoding the asynchrony of organ decline, the study demonstrates that the accumulation of liver-derived coagulation factors acts as a mechanistic driver of vascular and systemic aging.

Li et al., 2026, Cell *189*, 1–23
July 9, 2026
https://doi.org/10.1016/j.cell.2026.04.025

CellPress

Please cite this article in press as: Li et al., Multimodal clocks of human aging, Cell (2026), https://doi.org/10.1016/j.cell.2026.04.025

Cell

CellPress

Resource

Multimodal clocks of human aging

Jiaming Li,[1,3,31] Beier Jiang,[4,31] Wei Zhang,[5,31] Junwei Hao,[6,31] Zhili Liu,[7,31] Qianzhao Ji,[2,8,31] Yandong Zheng,[9,31] Xiaoyong Lu,[1,3,31] Zikai Zheng,[1,3,31] Shuai Ma,[2,3,8,31] Yanlin Fan,[1,31] Dan-Dan Gao,[4,31] Xiao-Wen Hou,[5,10,31] Jing Li,[11,31] Jiazhen Tang,[7,31] Yaobin Jing,[12,31] Lingling Geng,[9,31] Ruochen Wu,[2,3,31] Baohu Zhang,[2,3,31] Shuhui Sun,[13,31] Yusheng Cai,[2,31] Kaowen Yan,[2,31] Muzhao Xiong,[1,31] Chen Dong,[14,31] Xibo Ma,[15,16,31] Gang Xu,[17,18,31] Zhejun Ji,[2,8,31] Haoteng Yan,[9] Quan Zheng,[4] Honghao Huang,[5] Li Zhang,[11] Junming Li,[7] Mengmeng Jiang,[2,8] Liu-Jun Xu,[4] Yifan Chen,[5] Geyue Qu,[11] Wan Lei,[7] Hengchao Wang,[1] Jun Ping,[4] Jia Zhou,[10] Ming Yi,[11] Mingjin Jiang,[7]

(Author list continued on next page)

[1]Beijing Key Laboratory of Intelligent Governance and Application of Biological Big Data, China National Center for Bioinformation and Beijing Institute of Genomics, Chinese Academy of Sciences, Beijing 100101, China
[2]State Key Laboratory of Organ Regeneration and Reconstruction, Human Organ Physiopathology Emulation System, Institute of Zoology, Chinese Academy of Sciences, Beijing 100101, China
[3]University of Chinese Academy of Sciences, Beijing 100049, China
[4]Department of Respiratory and Critical Care, Quzhou Key Laboratory of Aging Biology and Longevity Medicine, Zhejiang-Germany Joint Laboratory on Lung Injury Repair and Regeneration, Quzhou Affiliated Hospital of Wenzhou Medical University, Quzhou People's Hospital, Quzhou 324000, China
[5]Department of Cardiology, Renji Hospital, School of Medicine, State Key Laboratory of Systems Medicine for Cancer, Shanghai Cancer Institute, Shanghai Jiao Tong University, Shanghai 200127, China
[6]Department of Neurology, Xuanwu Hospital Capital Medical University, National Clinical Research Center for Geriatric Diseases, Beijing 100053, China
[7]The First Affiliated Hospital, Jiangxi Medical College, Nanchang University, Nanchang, China
[8]Beijing Institute for Stem Cell and Regenerative Medicine, Beijing 100101, China
[9]Advanced Innovation Center for Human Brain Protection, National Clinical Research Center for Geriatric Disorders, Aging Translational Medicine Center, Beijing Municipal Geriatric Medical Research Center, Beijing Key Laboratory of Environment and Aging, Xuanwu Hospital Capital Medical University, Beijing 100053, China
[10]Central Laboratory, Ningbo Hangzhou Bay Hospital (Ningbo Branch of Renji Hospital, Shanghai Jiao Tong University School of Medicine, Shanghai), Ningbo, China
[11]Department of Geriatrics, Xuanwu Hospital Capital Medical University, National Clinical Research Center for Geriatric Diseases, Beijing 100053, China
[12]Key Laboratory of Reproductive Health Diseases Research and Translation of Ministry of Education, International Center for Aging and Cancer, Hainan Medical University, Haikou 571199, China

(Affiliations continued on next page)

SUMMARY

Human aging is characterized by complex structural and functional decline, but quantifying its heterogeneity and assessing biological age remain challenges. We present the mCAS (multicentric Chinese aging standardized cohort) developed from 2,019 Chinese individuals aged 18–91 years. Integrating high-dimensional clinical, physiological, and molecular-level data, we constructed a three-tiered aging framework: the core capacity clock (CC-clock) to quantify clinical physiological decline, the multimodal clock (MM-clock) with extensive parameter coverage and enhanced predictive precision, and organ-associated aging clocks. Cross-layer analysis demonstrates that plasma protein clocks not only capture chronological age but also serve as efficient proxies for systemic physiological capacity. Leveraging this framework for discovery, we identified the age-dependent accumulation of coagulation factors as a driver of multi-organ senescence and systemic inflammatory activation. This study provides a foundational framework that bridges molecular signatures with functional decline, identifies new biomarkers for aging assessment, and reveals a novel translational driver of aging.

INTRODUCTION

Aging, a fundamental determinant of human healthspan, is characterized by a complex biological decline that spans molecular, cellular, tissue, and systemic levels.[1–7] This decline manifests as progressive functional deterioration and includes diminished sensory and cognitive capabilities, motor slowing, immunometabolic dysregulation, and organ failure.[8–17] It is underpinned by altered gene expression, disrupted protein homeostasis, degraded organelle function, and impaired intercellular signaling.[18–24] The complexity of the molecular and physiological networks hinders our understanding of aging,[25–31] which leaves

Please cite this article in press as: Li et al., Multimodal clocks of human aging, Cell (2026), https://doi.org/10.1016/j.cell.2026.04.025

Ying Jing,[9] Wei-Dong Ye,[4] Xiao Zhang,[5,10] Xi Chu,[19] Yuting He,[7] Qian Zhao,[9] Qi Wu,[4] Meiling He,[10] Lina Ma,[11] Peng Liu,[7] Liyun Zhao,[9] Qiao-Cheng Zhai,[20] Jun Qin,[10] Jie Lu,[21] Xianhe Yang,[7] Shuo Zhang,[1,3] Yu Xiong,[4] Hua Ren,[10] Wei Yang,[11] Zhanmei Huang,[7] Jiachen Zhang,[9,22] Min Zhang,[4,23] Pei Chen,[10] Jian Dong,[19] Yu Zhang,[7] Tingting Yan,[9,22] Jin-Lin Ye,[20] Ping Huang,[10] Zhigang Qi,[21] Yong Liu,[7] Jichen Shuai,[9,22] Cheng-Shui Chen,[4] Ping Li,[5] Dawei Li,[6] Xiuhua Xu,[7] Xuexian Song,[15,16] Jingyi Li,[2,3,8] Jiale Ping,[1,3] Jinghao Hu,[9,22] Xiaoyan Sun,[1,3] Jiaqi Ai,[9,22] Zhengqin Wang,[2,3] Yuxin Zhang,[2,3] Peng Yang,[1,3] Taixin Ning,[9,22] Yan Yu,[2,3] Zan He,[9,22] Hui Zhang,[13] Tianyang Zhang,[1,3] Yuanhan Yang,[2,3] Qiaoran Wang,[1] Fangmin Lin,[2,3] Xiangmei Jin,[2] Xuewei Chen,[2] Jie Ren,[24,30,32] Moshi Song,[2,3,8,30,32] Si Wang,[9,30,32] Jiayin Yang,[17,18,30,32] Jianming Li,[7,32] Weihong Song,[25,30,32] Fuchu He,[26,27,30,32] Yun-Gui Yang,[1,3,30,32] Gang Pei,[28,30,*] Jing Qu,[2,3,8,13,30,*] Wei Zhang,[7,30,*] Jun Pu,[5,30,*] Feng Zhang,[4,30,*] Guoguang Zhao,[29,30,*] Weiqi Zhang,[1,3,30,33,*] and Guang-Hui Liu[2,3,8,30,*]

[13]Beijing Institute of Heart, Lung and Blood Vessel Diseases, Beijing Anzhen Hospital, Capital Medical University, Beijing 100029, China
[14]State Key Laboratory of Networking and Switching Technology, Beijing University of Posts and Telecommunications, Beijing 100876, China
[15]MAIS, State Key Laboratory of Multimodal Artificial Intelligence Systems, Institute of Automation, Chinese Academy of Sciences, Beijing, China
[16]School of Artificial Intelligence, University of Chinese Academy of Sciences, Beijing 100049, China
[17]Laboratory of Liver Transplantation, Key Laboratory of Transplant Engineering and Immunology, NHC, West China Hospital of Sichuan University, Chengdu, China
[18]Liver Transplant Center, Organ Transplant Center, West China Hospital of Sichuan University, Chengdu, China
[19]Health Management Center, Xuanwu Hospital, Capital Medical University, National Clinical Research Center for Geriatric Diseases, Beijing 100053, China
[20]Division of Orthopaedics, Quzhou Affiliated Hospital of Wenzhou Medical University, Quzhou People's Hospital, Quzhou 324000, China
[21]Department of Radiology and Nuclear Medicine, Xuanwu Hospital Capital Medical University, National Clinical Research Center for Geriatric Diseases, Beijing 100053, China
[22]Xuanwu Hospital Capital Medical University, Beijing 100053, China
[23]Department of Nutrition and Food Hygiene, School of Public Health, China Medical University, Shenyang 110122, China
[24]State Key Laboratory of RNA Innovation, Science and Engineering, CAS Center for Excellence in Molecular Cell Science, Shanghai Institute of Biochemistry and Cell Biology, University of Chinese Academy of Sciences, Chinese Academy of Sciences, Shanghai 200031, China
[25]Center for Geriatric Medicine, The First Affiliated Hospital and Oujiang Laboratory, Institute of Aging, Wenzhou Medical University, Wenzhou, China
[26]State Key Laboratory of Medical Proteomics, National Center for Protein Sciences (Beijing), Beijing, China
[27]International Academy of Phronesis Medicine (Guangdong), Guangzhou 510000, China
[28]The Collaborative Innovation Center for Brain Science, School of Life Sciences and Technology, Tongji University, Shanghai, China
[29]Department of Neurosurgery, Xuanwu Hospital Capital Medical University, National Clinical Research Center for Geriatric Diseases, Beijing 100053, China
[30]Aging Biomarker Consortium (ABC), Aging Biobank (ABB), Beijing, China
[31]These authors contributed equally
[32]Senior author
[33]Lead contact
*Correspondence: peigang@tongji.edu.cn (G.P.), qujing@ioz.ac.cn (J.Q.), ndyfy00266@ncu.edu.cn (W.Z.), pujun310@hotmail.com (J.P.), fengzhang@wmu.edu.cn (F.Z.), ggzhao@vip.sina.com (G.Z.), zhangwq@big.ac.cn (W.Z.), ghliu@ioz.ac.cn (G.-H.L.)
https://doi.org/10.1016/j.cell.2026.04.025

the field without precise metrics to quantify the process in humans.

Although biotechnological advancements have spurred the search for ideal aging biomarkers, the high heterogeneity of aging necessitates a composite multidimensional approach rather than a single universal marker.[32–36] Currently, a critical gap remains in distinguishing correlational "passengers" from mechanistic "drivers," which is essential for translating biomarker discoveries into therapeutic strategies.[2,32,37–39] Furthermore, while multi-omics technologies have generated vast datasets to capture this biological complexity, standardizing data and extracting reliable signals remain major hurdles.[40–42] Overcoming these challenges to systematically quantify aging requires establishing robust standard operating procedures (SOPs), advanced analytical frameworks, and cross-disciplinary collaboration.

To translate this vision into a tangible reality, the Aging Biomarker Consortium (ABC) has launched a major initiative—the "X-Age Project" (or "耄耋计划")—aiming to establish a comprehensive aging clock system for the Chinese population.[43,44] As the first proof-of-concept study for this endeavor, we establish herein a multicenter, standardized aging clock cohort. By integrating clinical, physiological, and molecular-level features with AI-driven modeling, we establish a multidimensional framework that deciphers asynchronous aging patterns and core regulatory axes, enabling the construction of a multi-organ, multilayered aging clock architecture. This framework supports precise biological age estimation, improves healthspan prediction, and provides a foundation for population-specific clinical aging metrics and geroprotective strategies.

RESULTS

Establishing a multicenter standardized cohort for human aging biomarker research

To create a standardized aging clock evaluation system for the Chinese population, we developed SOPs for recruiting naturally

aging individuals across multiple centers, which covers participant recruitment, biosample collection and storage, clinical testing, and multimodal data acquisition and analysis, to ensure consistency across sites (Figures 1A–1D and S1A; STAR Methods). Based on this framework, we established the mCAS (multicentric Chinese aging standardized cohort) from four representative cities, Beijing (BJ), Ningbo (NB), Quzhou (QZ), and Nanchang (NC), spanning different latitudes across China. Following unified inclusion and exclusion criteria (STAR Methods), a total of 2,019 healthy participants aged 18–91 years were enrolled (55% female, 45% male), spanning the full aging spectrum (Figure 1A).

We established a multilevel, multimodal assessment framework to systematically characterize aging phenotypes using predominantly non-invasive measures. Each participant completed questionnaires capturing lifestyle and nutritional factors to construct an exposome dataset and underwent behavioral and neurofunctional tests (e.g., Purdue Pegboard, grip strength, single-leg stance test, and trail making test). Comprehensive clinical assessments included anthropometry (42 parameters), cardiovascular function (63 parameters), pulmonary function (24 parameters), bone density (33 parameters), and blood testing (32 parameters) (Figure 1B; Table S1). In addition, multimodal imaging data were collected, including brain magnetic resonance imaging (MRI), carotid ultrasound, retinal imaging, facial images, and gait capture videos (Table S1).

On the day of the physical examination, fasting blood samples (whole blood, plasma, and peripheral blood mononuclear cells [PBMCs]) and fecal samples were collected from participants for multi-omics analysis, including DNA methylomics, bulk and single-cell transcriptomics of PBMCs, plasma proteomics, plasma metabolomics, and gut fecal metagenomics (Figures 1B, 1D, and S1B–S1G). Adhering strictly to unified SOPs, we generated over one billion high-quality data points (Figures 1B and 1D), which forms the foundation of a comprehensive, system-level evaluation framework of human aging.

Constructing the human core capacity clock

To systematically characterize human aging, we conducted multidomain phenotypic assessments spanning from external appearance parameters to core physiological function modules, including body morphology and composition; neural and cognitive modulation; motor coordination ability; circulatory transport; respiratory capacity; digestive, metabolic, and excretory processes; immune defense; and endocrine regulation (STAR Methods). Using standardized protocols across centers, we integrated 240 multimodal parameters, including morphology, function, imaging, and fluid biomarkers (Figure S2A). Morphological analysis showed that wrinkle area increased with age ($R = 0.76$), and a facial clock achieved high predictive accuracy ($R = 0.93$, mean absolute error [MAE] = 5.79) (Figure 2A).[45,46] Body morphology revealed age-related central obesity (increased waist-to-hip ratio and visceral fat), reduced appendicular skeletal muscle and body water, and declining bone density ($R = -0.34$) (Figures 2B, 2C, and S2B–S2D).

Neurocognitive and sensory assessments (trail making test, Purdue Pegboard, and pure-tone audiometry) demonstrated marked declines in processing speed, motor coordination, and auditory function, with task completion time doubling and hearing thresholds increasing approximately 3.5-fold from the 20s to 70s (Figures 2D–2F and S2E). MRI analysis revealed reduced inter-regional brain connectivity, particularly within language and memory circuits, and decreased cerebrospinal fluid volume (Figures 2G–2I, S2G, and S2H). A machine-learning-based brain-age model effectively captured these structural and functional shifts ($R = 0.94$, MAE = 5.79) (Figure 2J).

Motor function declined across all tests, with gait instability and reduced speed as sensitive markers (Figures 2K, 2L, and S2I). We constructed behavioral clocks based on motor features (motorClock, $R = 0.75$, MAE = 8.99; videomotorClock, $R = 0.62$, MAE = 10.65) (Figure 2M). Cardiovascular assessment revealed age-related diastolic/systolic dysfunction, arterial stiffness (pulse wave velocity increased ~1.9-fold), carotid remodeling, and retinal microvascular degeneration (Figures 2N, 2O, S2J, and S2K). Cardiovascular and retinal clocks achieved high predictive accuracy ($R = 0.90$ and 0.94) (Figure 2P). Pulmonary function tests showed declines in forced vital capacity (FVC), forced expiratory volume in 1 s (FEV_1), and mid-expiratory flow, with maximal oxygen uptake at age 80 reduced to 75% of that at age 20 (Figures 2Q and S2L).

Metabolic and organ function assessments identified age-related glycemic and lipid dysregulation, impaired liver synthetic function (decreased cholinesterase and albumin), and renal decline (increased urea in urine and decreased urine specific gravity), accompanied by an increase in chloride and a decrease in phosphorus with age (Figures 2R and S2M). Immune aging was characterized by increased neutrophil percentage and cytomegalovirus (CMV) immunoglobulin G (IgG) levels, with reduced lymphocyte counts (Figure 2S). Endocrine aging was marked by dramatic reproductive hormone shifts: in women, Anti-Müllerian hormone declined ~500-fold and follicle-stimulating hormone increased ~11-fold from the 20s to 70s ($R = -0.82$ and 0.71) (Figures 2T and S2E).

Integrating core aging-related parameters, we constructed the core capacity clock (CC-clock), which captures physiological decline across eight functional modules ($R = 0.88$, MAE = 6.23) (Figure 2U). Key contributors (e.g., FEV_1, systolic blood pressure [SBP], single-leg stance time, Purdue score, peak expiratory flow, and alkaline phosphatase) highlight vulnerable functional capacities in aging (Figure 2V).

Multi-omics signatures of human aging

To characterize aging dynamics and identify molecular aging markers, we performed integrative analyses of multi-omics data. We first defined a dyshomeostasis index (DHI) to quantify the global increase in physiological instability during aging. Using this framework, we found that core physiological capacity parameters were relatively stable in youth but became increasingly variable with age (Figure 3A). Similarly, key stability-related features across methylomics, transcriptomics, proteomics, and microbiomics from the same cohort showed age-associated increases in systemic disorder (Figure 3A). Consistent with prior reports of age-related increases in tissue structural and epigenetic entropy,[47–50] DHI captures the progressive loss of homeostasis and its association with functional decline.

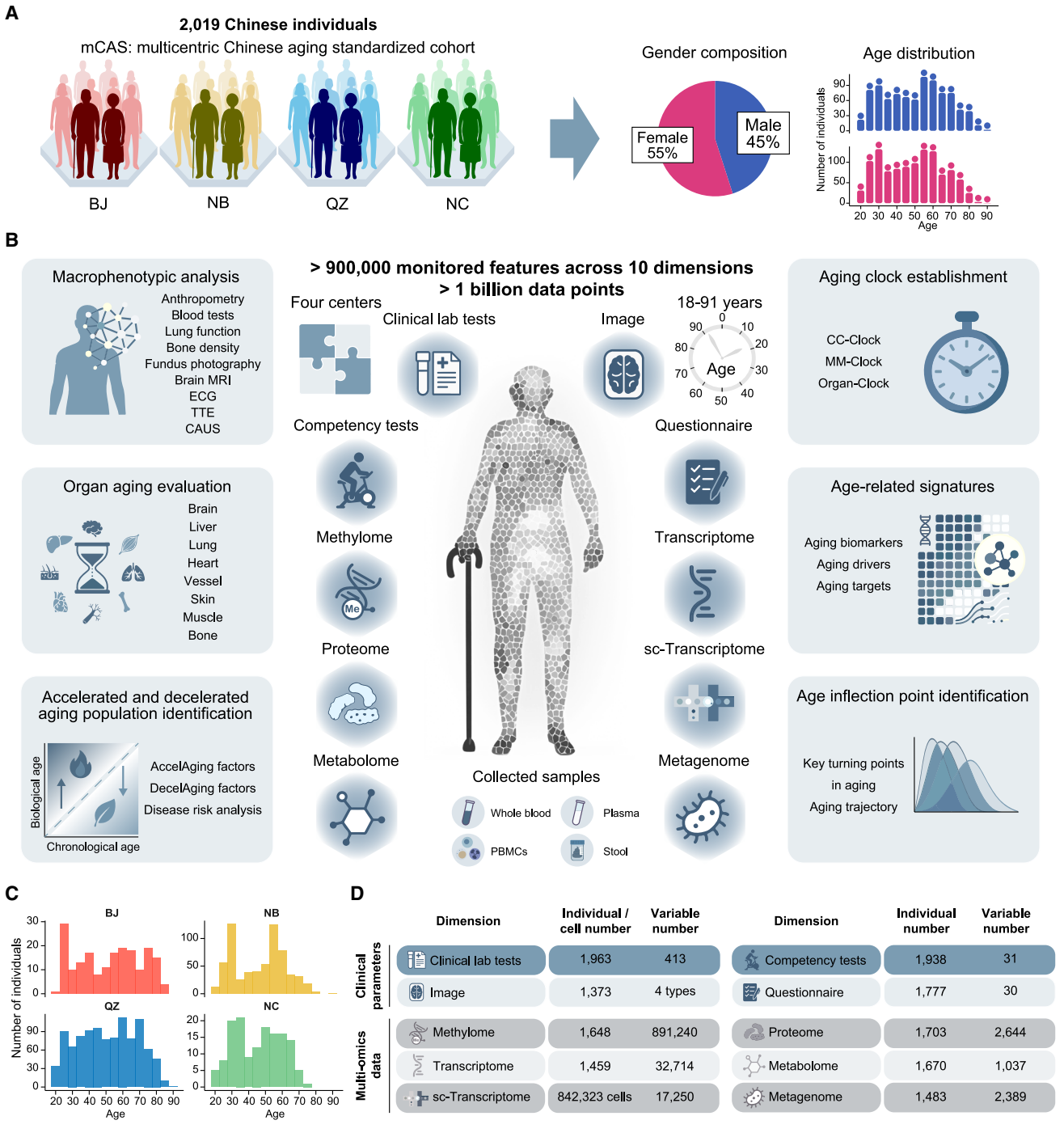

Figure 1. Establishment of a multicenter standardized aging cohort

(A) Overview of the multicenter aging cohort across four cities in China (Beijing [BJ], Ningbo [NB], Quzhou [QZ], and Nanchang [NC]), comprising 2,019 individuals aged 18–91 years, with a balanced sex distribution.

(B) Schematic of the aging clock cohort framework, integrating 10 major data dimensions including clinical lab tests, imaging, competency tests, questionnaires, and six omics layers (methylome, transcriptome, sc-transcriptome, proteome, metabolome, and metagenome). The framework enables multilevel aging clock modeling, stratification of aging trajectories (accelerated and decelerated aging), and identification of age-related biomarkers, mechanistic regulators, and inflection points. ECG, electrocardiogram; TTE, transthoracic echocardiography; CAUS, carotid artery ultrasonography. CC-clock, core capacity clock; MM-clock, multimodal clock; AccelAging, accelerated aging; DecelAging, decelerated aging. sc, single cell.

(C) Age-distribution histograms of participants across the four centers.

(D) Overview of participants or cell numbers and variable counts across each data dimension.

See also Figure S1.

Please cite this article in press as: Li et al., Multimodal clocks of human aging, Cell (2026), https://doi.org/10.1016/j.cell.2026.04.025

CellPress

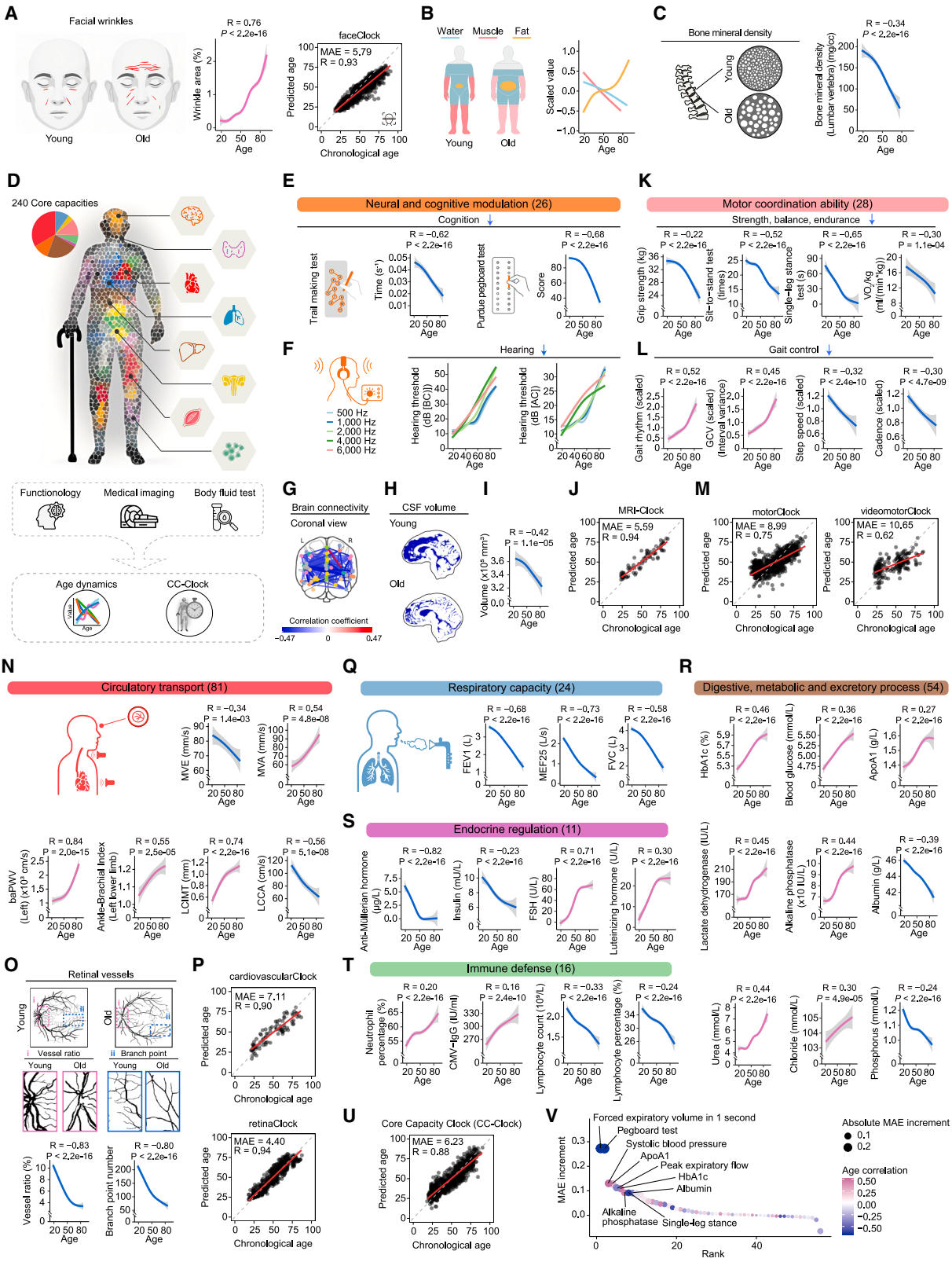

(legend on next page)

Please cite this article in press as: Li et al., Multimodal clocks of human aging, Cell (2026), https://doi.org/10.1016/j.cell.2026.04.025

To identify aging molecular signatures, we assessed multi-omics associations with chronological age. While the methylome harbored the highest number of age-related features, the proteome and metabolome showed stronger relative changes (Figures 3B and 3C; Table S1). Consistent with previous studies,[47] age-associated methylation was predominantly decreased, which is consistent with global hypomethylation, with hypomethylated sites enriched in innate immunity and hypermethylated sites linked to development (Figure 3D). Notably, *ELOVL2*, which contains the most strongly associated age-upregulated methylation site, emerged as a consistent epigenetic marker of aging across multiple independent cohorts (Figure 3C).[51,52] Cross-cohort comparisons indicated the highest concordance in clinical traits, followed by proteins, while transcriptomic signals were more heterogeneous (Figure S3A),[53] which reflects both conserved and population-specific aging features.

Based on PBMC transcriptomic profiling, we identified key age-associated features, including upregulation of *CDKN2A*, *MiR34AHG*, *FIGN*, and *SYT11*, and downregulation of naive immune cell-associated genes such as *NRCAM* (neuronal cell adhesion molecule), *CACHD1*, *ROBO1*, and *CD248* (Figure 3C).[54–59] These changes were validated by quantitative reverse-transcription polymerase chain reaction (RT-qPCR) (Figure 3E). Immune cell deconvolution based on single-cell transcriptome and flow cytometry further confirmed an age-related decline in naive $CD8^+$ and $CD4^+$ T cell subsets, and an increase in $CD27^-$, $CD28^-$, and $CD57^+$ T cells across centers, which are markers of senescent or exhausted immune phenotypes (Figures 3F–3H and S3B–S3I). Pathway analysis revealed age-related upregulation of inflammatory signaling and downregulation of RNA processing and ribosome biogenesis pathways (Figure 3D). Additionally, aging was associated with decreased heterochromatin-related gene expression and increased DNA damage response, supported by reduced H3K9me3 and elevated phosphorylated histone H2AX (γH2AX) levels, which are consistent across centers (Figures 3I, S3J, and S3K).[60,61]

Proteomic profiling revealed enhanced coagulation activation and extracellular matrix (ECM) remodeling with age (Figure 3D). Key proteins such as surfactant protein B (SFTPB) and LTBP2 showed age-related increases (Figure 3C), while SFTPB is a marker of pulmonary stress[62–64] and LTBP2 is implicated in fibrotic remodeling.[65,66] These changes aligned with lung function decline observed in clinical phenotyping (Figure 2Q), supporting the use of circulating proteins to monitor pulmonary aging.

Through metabolomic profiling, we identified age-related shifts characterized by activation of the urea cycle and downregulation of ammonia recycling as well as glycine and serine metabolism (Figure 3D). For example, N2, N5-diacetylornithine accumulated with age, while plasma tryptophan levels declined. We further identified reductions in steroid hormones (Figure 3C; Table S1), which indicates impaired endocrine function. In

Figure 2. Age-related changes in human core physiological capacities

(A) Representative pictures showing the facial wrinkles of the young and the old (left). The graph's curve shows the increased ratio of wrinkles with age (middle). Dot plot showing the correlation between predicted age of the faceClock and chronological age (right). MAE, mean absolute error.
(B) Characteristics of human body composition (muscle, water, and fat) in young and old individuals (left). A curve graph showing the loss of muscle (skeletal muscle mass [lower limit standard], pink) and water (total body water, blue) with age, while there is an increase in fat (visceral fat area, yellow) with age (right).
(C) Characteristics of bone mineral density of lumbar vertebrae during aging. The graph's curve shows the loss of lumbar vertebral bone mineral density with age.
(D) A schematic diagram showing the core physiological function modules, totaling 240 clinical parameters.
(E) Age-related increased time required for the trail making test (left) and decreased score of the Pegboard test (right).
(F) Age-related increased bone conduction (BC) hearing threshold (left) and air conduction (AC) hearing threshold (right).
(G) The correlation between the strength of functional connectivity groups (coronal plane) in different brain regions with age.
(H) Representative images of the volume of cerebrospinal fluid (CSF) in the young and the old.
(I) Age-related decreases in the volume of CSF.
(J) The correlation between predicted age from the MRI-Clock and chronological age based on the brain MRI.
(K) Age-related decreases in strength, balance, and endurance, including the grip strength test, the 30-s sitting and stand test, the single-leg stance test, and the maximum oxygen consumption from a stationary bike.
(L) Age-related increases in gait variability (gait rhythm and gait cycle variability) and decreases in motor ability (step speed and cadence) with age.
(M) The correlation between predicted age and chronological age based on behaviors (left) and video behaviors (right).
(N) The characteristics of cardiovascular function change with age. MVA, mitral valve A-wave flow velocity; baPWV, brachial-ankle pulse wave velocity; LCIMT, left carotid intima-media thickness; MVE, mitral valve E-wave flow velocity; LCCA, left common carotid artery flow velocity.
(O) Representative images of the number of point branches and vessel density of retinal vessels in young and old people. The graph's curve shows the decreasing ratio of vessels (i) and the number of branch points (ii) with age.
(P) Correlation between predicted age and chronological age based on cardiovascular function (top) and retinal imaging (bottom).
(Q) Age-related decreased lung function features, including forced expiratory volume in 1 s (FEV_1), forced vital capacity (FVC), and maximum expiratory flow rate (MEF25) when 75% of the gas is forcefully exhaled and 25% remains.
(R) Age-related changes of the indicated clinical measurements in blood and urea in urine.
(S) Age-related changes in hormone levels. FSH, follicle-stimulating hormone.
(T) Age-related changes of immune cells in the blood.
(U) The correlation between predicted age and chronological age based on the core capabilities of the human body.
(V) The feature-importance analysis of CC-clocks.
In (A), (J), (M), (P), and (U), correlation coefficients (Pearson's correlation) and MAE are denoted. Red lines represent the linear fitting results. For curve plots showing the single-feature value, Spearman's rank correlation coefficient (rho) and adjusted *p* value were indicated. Benjamini-Hochberg was used to calculate the adjusted *p* value. The trend lines (red, increased with age; blue, decreased with age) represent the generalized additive model fits obtained from the scatterplot.
See also Figure S2 and Table S1.

Please cite this article in press as: Li et al., Multimodal clocks of human aging, Cell (2026), https://doi.org/10.1016/j.cell.2026.04.025

CellPress

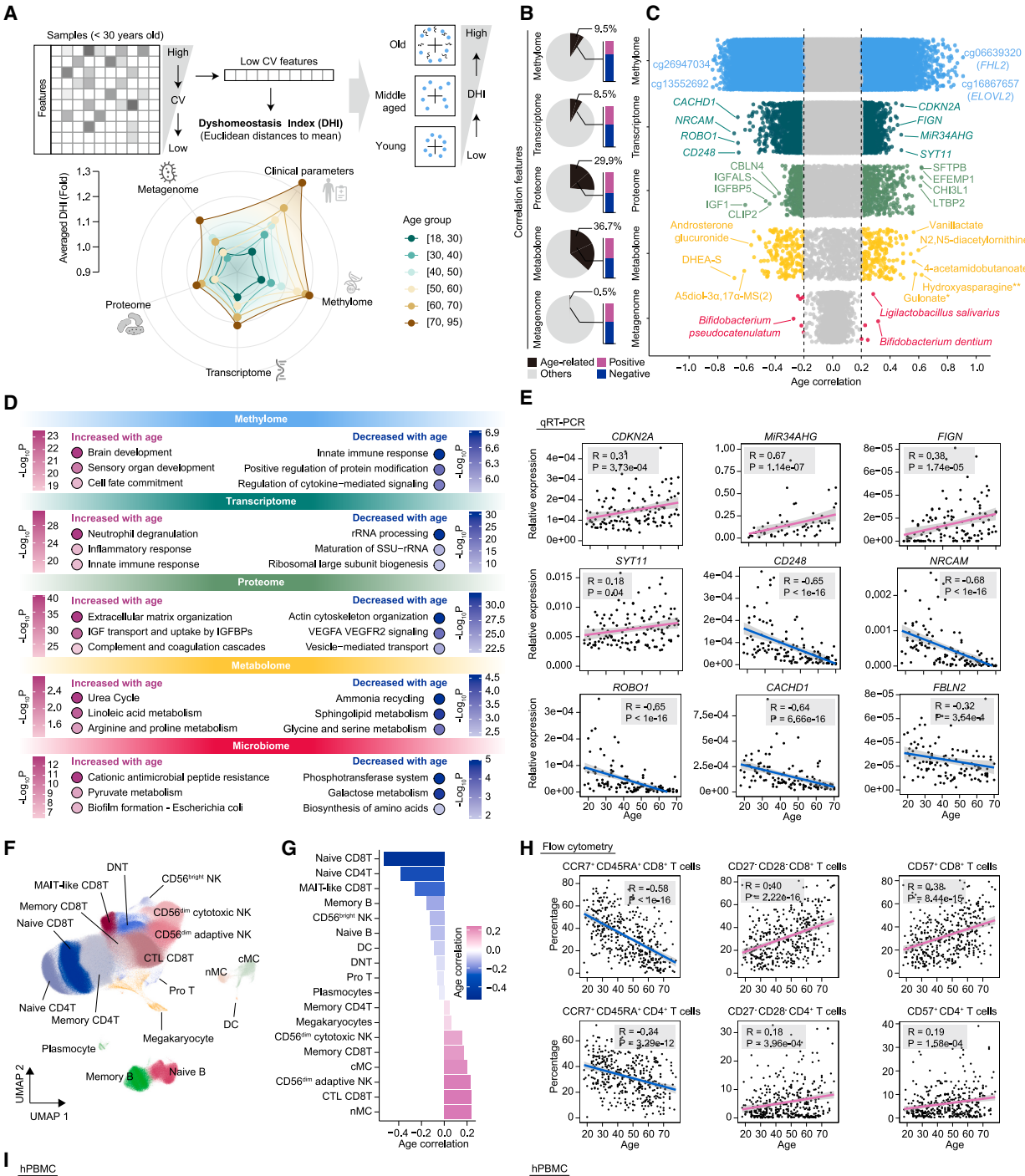

(legend on next page)

Please cite this article in press as: Li et al., Multimodal clocks of human aging, Cell (2026), https://doi.org/10.1016/j.cell.2026.04.025

parallel, gut microbiome analysis revealed age-related alterations in microbial composition, including increased abundance of antibiotic-resistant strains such as *Klebsiella pneumoniae* (Table S1).[67,68]

Construction and integration of the multimodal aging clock

We then constructed aging clocks across multiple omics layers, with the methylation clock showing the best performance (R = 0.97, MAE = 2.72), followed by protein (R = 0.90, MAE = 5.53), transcript (R = 0.90, MAE = 5.75), and metabolite clocks (R = 0.89, MAE = 5.73), while the microbiome clock performed relatively weakly (R = 0.57, MAE = 11.49). All models showed consistent performance across centers (Figure S4A). Compared with established epigenetic clocks (Hannum, Horvath, and Levine),[69–72] our methylation clock achieved a lower MAE (3.58–8.17) (Figure S4B), suggesting population-specific differences.

To understand the biological significance of these omics-based aging clocks, we performed feature-importance analysis of key features for each clock (Figures 4C and 4D; Table S2; STAR Methods). The results highlighted several known or potential aging-related molecules across the omics. In the methylation clock, *TRIM59* and *TSPO* were the most contributive sites (Figure 4C). In the transcript clock, key features were associated with cell migration and nucleosome assembly, including *FIGN* and *NAP1L2* (Figure 4C). In the protein clock, CILP2, an ECM protein implicated in the degradation of osteoarthritic cartilage, emerged as the most contributive feature to the clock (Figure 4C). In the metabolite clock, cystine, which is indicative of oxidative stress,[73,74] and vanillylmandelate, a methoxyphenol biomarker of psychological stress and neuroendocrine tumors,[75,76] contributed most to the prediction (Figure 4C).

To integrate multilevel data, we constructed a multimodal clock (MM-clock). We introduced attention and inception mechanisms to achieve joint integration of multimodal data (Figures 4A and S4C; STAR Methods). Specifically, we input features of each omics into independent attention modules to learn their importance weights, which enhances the model's adaptability to omics heterogeneity. We then used the inception structure to integrate higher-order representations of different modalities. The MM-clock (R = 0.95, MAE = 3.87) outperformed the CC-clock, transcriptome clock, and proteome clock, indicating high complementarity among different modalities in characterizing the aging clock (Figure 4B).

To characterize dynamic multi-omics changes during aging, we applied generalized additive models and joint clustering, identifying six trajectory patterns (crest 1, crest 2, decline 1, decline 2, decline 3, and incline) (Figures 4E and S4D; Table S3). These revealed two major inflection periods (~40–50 and ~60–70 years). The first was marked by hormonal fluctuations and lipid accumulation, while the second featured increased blood pressure, reduced bone density, and pronounced activation of the coagulation cascade (e.g., F5, F7, F9, and F13B) (Figures 4E and 4F). Consistently, coagulation factors showed higher attention weights in the MM-clock for older individuals, suggesting a potential role of coagulation-related signals in aging (Figure S4E).

Construction of organ-associated aging clocks

To quantify organ-associated aging, we implemented a three-tiered strategy integrating clinical, molecular, and multimodal data to construct clocks for six organs (Figure 5A). The first layer (organ clinical-clocks) used organ-associated clinical markers (e.g., Purdue Pegboard for brain, wrinkle index for skin, and FEV_1 for lung), which capture physiological aging but have limited precision due to their low dimensionality (Figures 5B and 5C; Table S1). The second layer (organ protein clocks) leveraged plasma proteins as remote indicators of organ health,[77,78] identifying key biomarkers such as ADAMTS13 (a disintegrin and metalloproteinase with thrombospondin type 1 motif 13) (liver),[79] NRCAM (brain),[80,81] and ABI3BP (ABI family member 3 binding protein) (skin)[82] (Figure 5B; Table S2), which show a strong concordance with clinical predictions (Figure S4F). The third layer integrated structural, functional, and molecular features via an elastic net framework to build organ multimodal clocks (organ MM-clocks), which outperformed single-layer models across multiple organs (Figures 5B and 5C).

Figure 3. Multi-omics molecular signatures of human aging

(A) (Top) The strategy to evaluate the change of feature stability in multi-omics datasets with age. (Bottom) Age-related increased dyshomeostasis index (DHI). CV, coefficient of variation.

(B) (Left) The ratio of multi-omics age-related features in total detected features. (Right) The ratio of positively and negatively age-correlated multi-omics features. For better visualization, the same threshold (Spearman's correlation, $|R| > 0.2$, adjusted p value < 0.05) was applied to all datasets.

(C) The age-related features of multi-omics data. The top features (ranked by correlation coefficient) are denoted. Asterisks denote putatively annotated metabolites lacking authentic standard validation; * and ** indicate high- and moderate-confidence annotations, respectively.

(D) The enriched pathways that increased and decreased with age for multi-omics data.

(E) RT-qPCR analysis of age-related genes (*CDKN2A*, *MiR34AHG*, *FIGN*, *SYT11*, *CD248*, *NRCAM*, *ROBO1*, *CACHD1*, and *FBLN2*) in human PBMCs. $n > 120$ individuals. *18S* and *ACTB* were used as controls.

(F) Uniform manifold approximation and projection (UMAP) plot showing the cell-type distribution of human PBMCs based on single-cell RNA sequencing (scRNA-seq) data. cMC and nMC, classical and non-classical monocyte; Pro T, proliferative T cell; NK, natural killer; DC, dendritic cell; CTL, cytotoxic; MAIT, mucosal-associated invariant T cell; DNTs, double-negative T cells.

(G) The Spearman's correlation between cell-type proportion, deconvoluted with bulk RNA-seq, and age.

(H) Flow cytometry detection of specific cell populations in $CD4^+$ T cells or $CD8^+$ T cells in PBMCs. $n = 397$ individuals randomly selected with approximately balanced representation across centers.

(I) Immunofluorescence (IF) staining of H3K9me3 and γH2AX in human PBMCs. Representative images and quantitative data for the mean fluorescence intensity of H3K9me3 (left) and percentage of γH2AX-positive cells (right) are shown. $n = 200$ individuals randomly selected with approximately balanced representation across centers. Scale bars, 10 μm. Values were normalized to the mean value of the youngest group (<30 years of age).

See also Figure S3 and Table S1.

Please cite this article in press as: Li et al., Multimodal clocks of human aging, Cell (2026), https://doi.org/10.1016/j.cell.2026.04.025

CellPress

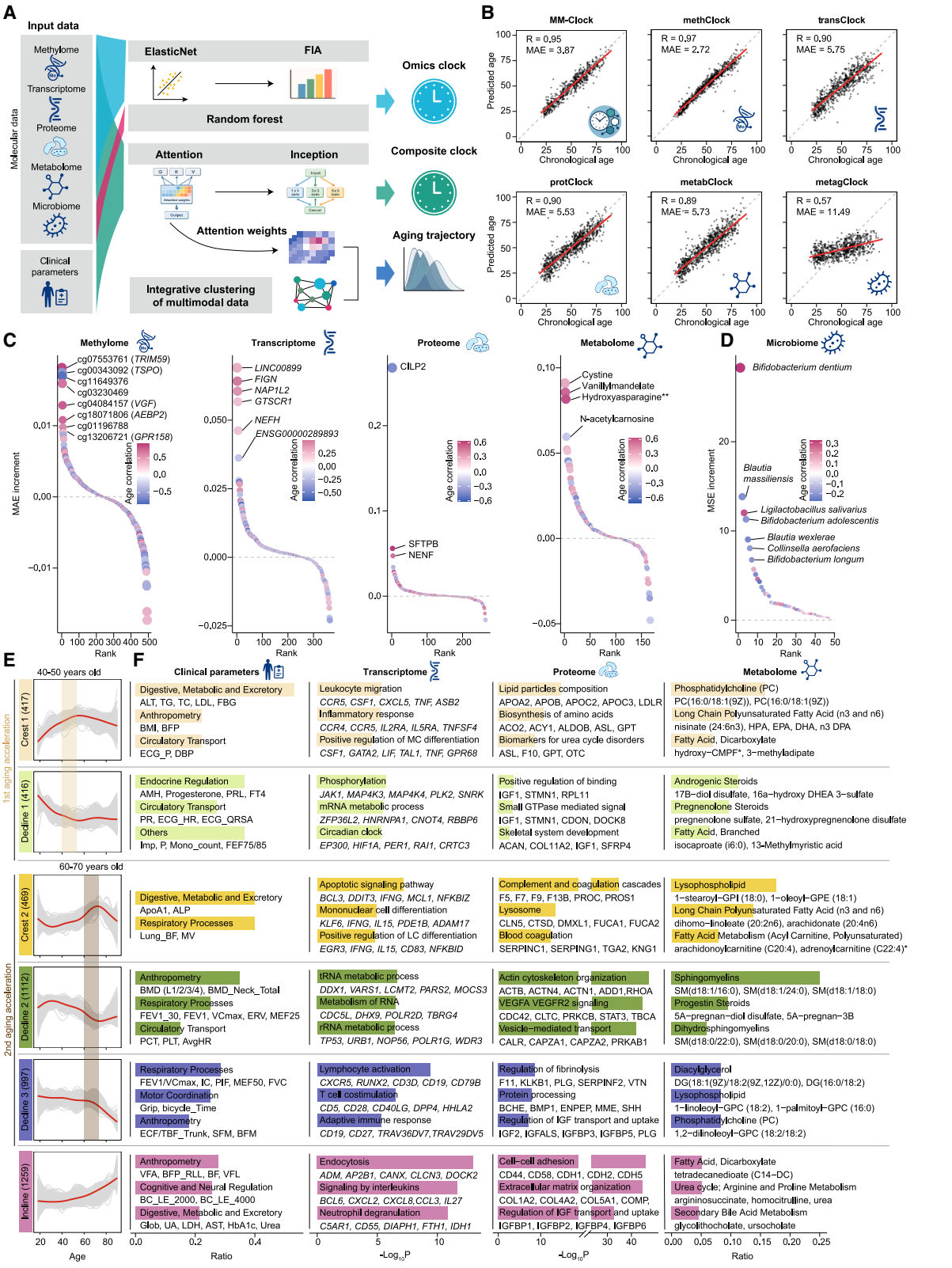

(legend on next page)

Please cite this article in press as: Li et al., Multimodal clocks of human aging, Cell (2026), https://doi.org/10.1016/j.cell.2026.04.025

Feature-importance analysis pinpointed system-specific aging drivers, such as SFTPB for the lung, ECM proteins for the skin, and aspartate aminotransferase (AST) and FABP1 for the liver (Figure 5D; Table S2). Systematic analysis across organs revealed pronounced aging asynchrony, with the liver exhibiting a critical inflection point at approximately age 40, earlier than the brain (age 50). This suggests that the liver, as a systemic metabolic and detoxification hub, is more sensitive to the early aging process (Figure S4G).

Development of a simplified aging clock system

To enhance clinical applicability, we simplified the aging clocks via feature-importance analysis (Figure 5E), reducing feature dimensions by 28.6%–63.9% without compromising performance (R, MAE) (Figures 5F and 5G). We developed protein-based proxies for clinical and organ-level clocks, leveraging their functional relevance and accessibility (Figure 5E). A set of 100 proteins recapitulated the 56-parameter CC-clock, and 108 proteins approximated the MM-clock (Figures 5H and S5B). In contrast, methylation-based proxies required more features (151–194 sites) and showed lower feature consistency despite similar accuracy (Figures 5I and S5C).

Additionally, methylation proxy models relied on a larger number of C–phosphate–G (CpG) sites with less overlap, whereas protein-based proxy models required fewer proteins and exhibited greater consistency (Figure S5D). Accordingly, the number of CpG features increased rapidly with additional proxy clocks, whereas the protein-based models expanded more slowly, which suggests that a smaller protein set captures shared aging information (Figure 5J). We identified "core anchors" such as chitinase 3 like 1 (CHI3L1), insulin-like growth factor binding protein 5 (IGFBP5), latent transforming growth factor beta binding protein 2 (LTBP2), and ADAMTS13 as key features across multiple protein proxies, whereas *SFMBT1* and *KLF14* (KLF transcription factor 14) characterized methylation models (Table S2). Functional enrichment highlighted ECM remodeling and inflammatory pathways as central themes (Figure S5E). In functional validation, the protein-proxy clock showed higher sensitivity in distinguishing fast versus slow agers, capturing more pronounced clinical differences, including reduced serum albumin, elevated AST/alkaline phosphatase (ALP), and impaired lung function (FEV_1 and maximum vital capacity [VC_{max}]) (Figures 5L and S5F). These clinical signatures consistently mirrored damage in liver- and lung-specific organ clocks, which reinforces the link between systemic acceleration and organ-specific decay (Figure S5F).

Multidimensional aging clocks reveal key regulators of aging asynchrony

To assess the practical utility of our framework, we calculated the pase of individual age as the deviation between predicted biological age and chronological age (Figure 6A). Among all omics-based predictors, the proteome clock demonstrated the highest correlation with the CC-clock, outperforming the methylome and transcriptome clocks (Figures 6B, 6C, and S6A). These findings align with the role of proteins as the primary executors of biological function, positioning them as superior "vitality biomarkers" that mirror systemic physiological status.

We defined the top and bottom 20% of aging pace as "fast" and "slow" agers, selecting individuals with consistent trends across $\geq$3 clocks (STAR Methods) (Figures 6D and S6B). Earlier bedtime, frequent walking, regular fruit consumption, and caregiving for grandchildren were associated with slower aging, whereas smoking, higher meal frequency, and short sleep (<6 h) accelerated aging (Figures 6E, 6F, S6C, and S6D; Table S4). For example, heavy smoking (>20 cigarettes/day) advanced lung age by ~4 years, while optimal bedtime (21:00–23:00) delayed CC-clock age by >3 years (Figures 6E and 6F). In addition, slow agers showed better motor coordination, lung function, and platelet levels, with an up to 15-year delay in brain/motor clocks (Figure 6G), whereas fast agers had higher blood pressure, waist-to-hip ratio, and ALP, with elevated blood pressure linked to >6-year acceleration in vessel and CC-clocks (Figure 6H).

Proteome clock analysis identified IGFBP5 as the top marker for decelerated aging and cartilage intermediate layer protein (CILP) as the strongest correlate for accelerated aging (Figure S6E; Table S5). Functionally, accelerated-aging proteins were enriched in coagulation, adhesion, and matrix remodeling, whereas decelerated-aging proteins were mapped to nucleotide and carboxylic acid metabolism (Figures 6I and 6J). Clinically, accelerated-aging proteins correlated positively with age-related risk factors (e.g., SBP, LDL, and C-reactive protein [CRP]), while decelerated-aging proteins aligned with protective traits such as bone density and lung function, indicating tight coupling with systemic aging phenotypes (Figures S6F and S6G).

We performed Mendelian randomization to further assess causal links between protein biomarkers and disease (STAR

Figure 4. Construction and integration of multimodal aging clocks

(A) A diagram showing the establishment of single-omics aging clocks and composite clocks using a deep-learning approach.

(B) The predicted age of the MM-clock, methClock, transClock, protClock, metabClock, metagClock, and their linear relationship with chronological age. Correlation coefficients (Pearson's correlation) and MAE are denoted. Red lines represent the linear fitting results.

(C) Feature-importance analysis of multi-omics clocks.

(D) Feature-importance analysis of the metagenomics clock. MSE, mean squared error.

(E) Smoothed fitting curve plots showing scaled predicted values of age-associated features across five omics layers, which are ordered and grouped into six distinct aging trajectory clusters. Red and gray lines represent the fitted lines from generalized additive models for a cluster and a feature, respectively.

(F) Representative functional terms, pathways, and key features enriched in each trajectory cluster, organized by omics layer. For the clinical parameter and metabolome layers, the proportion of features within each cluster is shown. For transcriptome and proteome layers, enriched terms and biological processes are displayed.

Asterisks denote putatively annotated metabolites lacking authentic standard validation; * and ** indicate high- and moderate-confidence annotations, respectively.

See also Figure S4 and Tables S2 and S3.

Please cite this article in press as: Li et al., Multimodal clocks of human aging, Cell (2026), https://doi.org/10.1016/j.cell.2026.04.025

CellPress

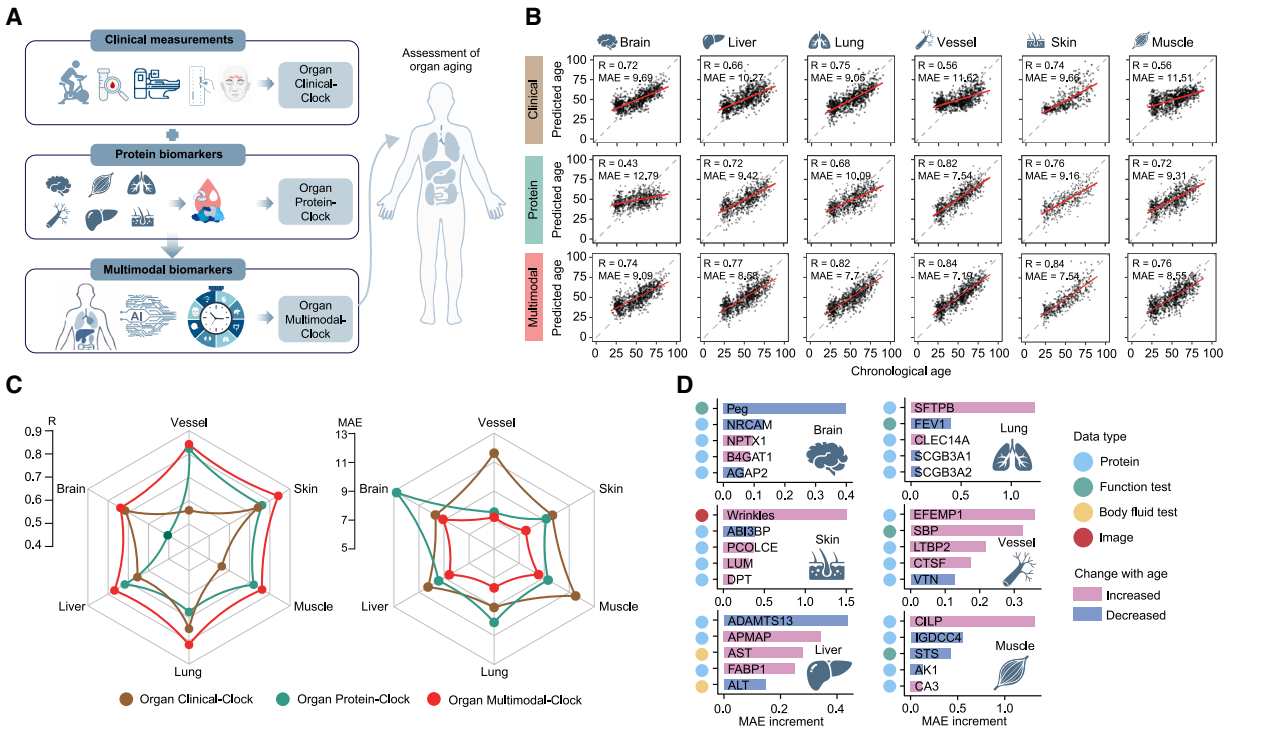

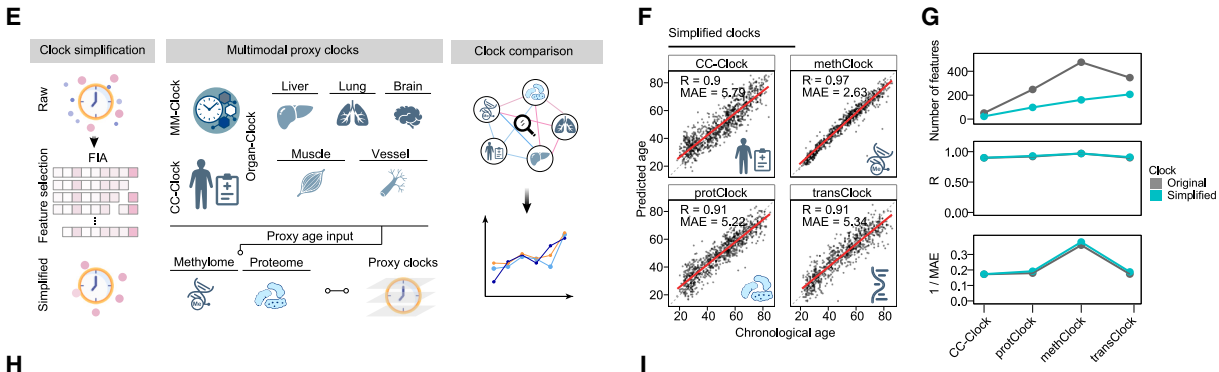

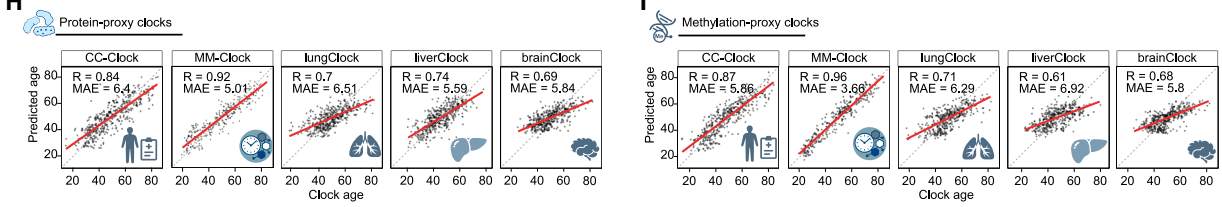

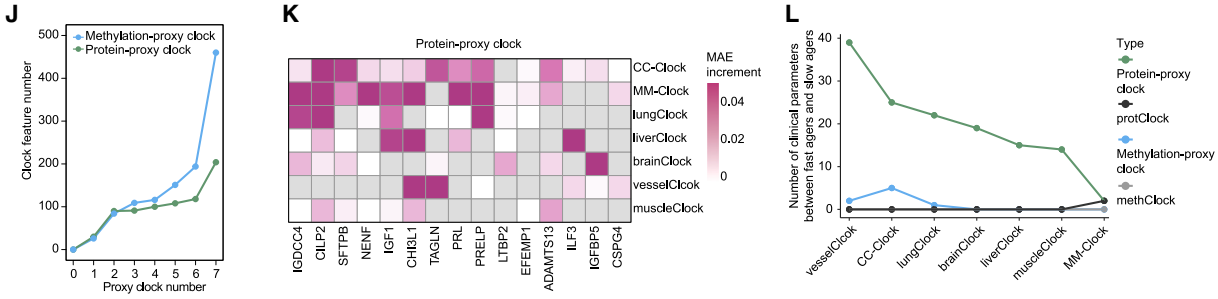

(legend on next page)

Please cite this article in press as: Li et al., Multimodal clocks of human aging, Cell (2026), https://doi.org/10.1016/j.cell.2026.04.025

Methods). Over 123 proteins linked to accelerated aging showed potential causal associations with ~240 diseases, primarily involving cardiovascular, digestive, and musculoskeletal systems (e.g., hypertension, gallstones, and osteoporosis) (Figures 6K and S6G), whereas decelerated-aging proteins showed limited disease associations (Figure S6H). Notably, several accelerated-aging proteins, including F9, F8, IGFBP1, and VWF, exhibited broad multi-disease effects (Figure 6L), with F9 linked to vascular conditions (e.g., hyperlipidemia, thrombosis, and aortic disease) and F8 to circulatory disorders (Figures 6L and S6I).

Coagulation factors as integrative biomarkers and mediators of vascular and systemic aging

Our prior findings revealed that coagulation factors displayed a "co-enhancement" pattern with multiple core aging phenotypes in the elderly, are associated with accelerated metrics of various aging clocks, and exhibited causal links with several aging-related diseases in Mendelian randomization analyses. These observations suggest that coagulation factors may not only serve as biomarkers of aging but also actively drive systemic aging. In line with this, stratification by age-accumulated coagulation-factor score showed that individuals with higher scores exhibited worse aging-related clinical parameters and accelerated aging across multiple clocks (Figures S7A–S7C; STAR Methods).

To evaluate this hypothesis, we analyzed the age-related changes of coagulation-pathway-related proteins in multicenter data and found that over 20 coagulation-related proteins are widely upregulated with age, such as F5, F7, F8, F9, F10, F13B, tissue factor pathway inhibitor (TFPI), and fibrinogen gamma chain (FGG) (Figure 7A). This finding was subsequently validated in an independent cohort using ELISA, with the most prominent increases observed for F13B, F9, F10, and TFPI (Figure 7B). Given that the liver is the primary source of coagulation factors,[83] we performed immunofluorescence staining on human liver tissues and revealed a marked increase in the number of F9-, F10-, and F13B-positive cells in aged liver tissues, which suggested a liver-derived contribution to their accumulation in aging plasma (Figures 7C–7E).

Functionally, the treatment of human aortic endothelial cells with age-relevant concentrations of F9, F10, F13B, and TFPI induced a pronounced senescence phenotype (Figures 7F–7N). This was characterized by the upregulation of senescence markers (increased senescence-associated β-galactosidase [SA-β-Gal] positivity, P21 levels, and DNA damage marked by γH2AX), coupled with the suppression of proliferation and homeostatic functions (reduced marker of proliferation Ki-67 [Ki67]-positive cells, decreased expression of nuclear lamina protein LAP2, and lower heterochromatin levels marked by H3K9me3) (Figures 7G–7I, 7N, and S7D–S7F). In addition, endothelial tube formation capacity was impaired (Figures 7J, 7N, and S7G), accompanied by upregulation of adhesion molecules (vascular cell adhesion molecule 1 [VCAM1] and intercellular adhesion molecule 1 [ICAM1]) and the chemokine monocyte chemotactic protein 1 (MCP-1) (Figures 7K and S7H). Consistently, monocyte recruitment and adhesion to endothelial cells were enhanced (Figures 7L, 7N, and S7I). Furthermore, coagulation-factor treatment induced the expression of pro-inflammatory and senescence-associated secretory phenotype (SASP) factors, including interleukin (IL)-6, IL-8, IL-1β, matrix metallopeptidase (MMP) 2, and MMP9 (Figures 7K, 7M, 7N, S7H, and S7J).

To further evaluate the *in vivo* effects of coagulation factors, we focused on F13B for causal validation due to its pronounced age-related increase (Figure 7O). Administration of recombinant F13B induced marked multi-organ senescence, characterized by elevated P21-positive cells in liver, heart, aorta, and kidney (Figure 7P). Notably, the liver showed the strongest response, which also showed increased γH2AX, reduced H3K9me3, and enhanced immune cell infiltration (Figures S8A and S8B). Moreover, F13B treatment amplified immune-inflammatory activation, as evidenced by increased $CD45^+$ and $F4/80^+$ immune cells and elevated expression of IL-6, IL-1β, S100A8, and mouse mammary tumor virus (MMTV) (a proxy for endogenous retrovirus activation associated with aging)[23,84] (Figures 7Q and S8C–S8I). These findings indicate that F13B can induce coordinated cellular senescence and inflammation across organs *in vivo*, which supports its role as a potential driver of systemic aging.

Figure 5. Organ-specific and proxy aging clocks

(A) Schematic workflow for building organ-associated multimodal aging clocks. The process involves the following sequence: (1) constructing clinical clocks based on organ-associated clinical parameters; (2) building up protein clocks through analysis of human organ and plasma proteomics data; (3) creating an integrated organ-associated multimodal aging clock combining protein profiles with clinical data.

(B) The predicted age with organ clinical-clock, organ protein-clock, organ MM-clock, and their linear relationship with chronological age.

(C) Performance comparison of three aging clocks, including the organ clinical-clock, organ protein-clock, and organ MM-clock.

(D) Feature-importance analysis of organ MM-clocks. There are four categories: blue representing plasma proteins, green indicating functional tests, yellow denoting body fluid assays, and red signifying imaging examinations.

(E) Schematic diagram of the construction process of simplified clocks, the development of proxy clocks, and the comparison among different clocks.

(F) The predicted age of simplified CC-clock, methClock, protClock, transClock, and their relationships with chronological age.

(G) Line plots comparing the number of parameters, correlation coefficients (Pearson's correlation), and 1/MAE values for the original and the simplified clocks.

(H and I) The predicted age of prot-proxy (H) and meth-proxy (I) clocks and their relationship with the original clock age.

(J) The number of features required for constructing different numbers of proxy clocks.

(K) The key features of protein-proxy clocks based on feature-importance analysis, with color intensity indicating the importance of the features.

(L) The number of different clinical parameters between fast agers and slow agers in various types of clocks (methylation-proxy clock, methClock, protein-proxy clock, and protClock) in various proxied clocks (CC-clock, lungClock, muscleClock, liverClock, MM-clock, vesselClock, and brainClock).

In (B), (F), (H), and (I), correlation coefficients (Pearson's correlation) and MAE are denoted. Red lines represent the linear fitting results.

See also Figures S4 and S5 and Table S2.

Please cite this article in press as: Li et al., Multimodal clocks of human aging, Cell (2026), https://doi.org/10.1016/j.cell.2026.04.025

CellPress

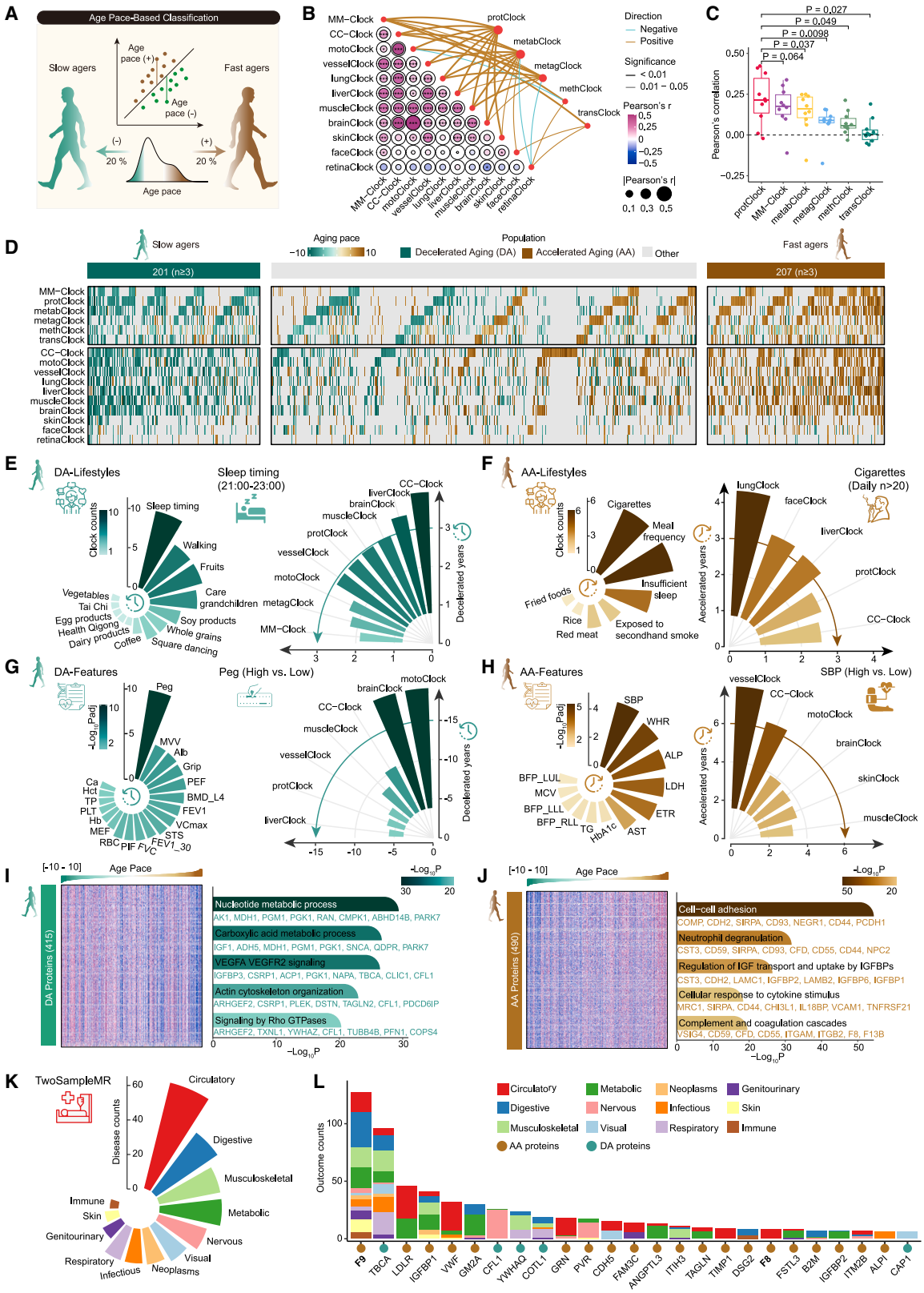

(legend on next page)

DISCUSSION

This study establishes a multidimensional aging reference system for the Chinese population, which integrates clinical phenomics, organ function, and multi-omics molecular profiles. Based on this framework, we developed CC-clock, MM-clock, and organ-associated aging clocks, providing a computational and multidimensional representation of individual aging states, conceptually approximating a digital human framework. These clocks capture the heterogeneity and asynchrony of aging and identify the accumulation of coagulation factors as an aging biomarker and potential driver of vascular degeneration. Overall, our work links molecular aging programs to organ-level functional decline, thus enabling a more comprehensive and quantitative assessment of human aging.

Traditional aging biomarkers primarily focus on single dimensions, such as cellular or molecular aspects.[85–91] For instance, epigenetic clocks rely on genomic DNA methylation patterns,[69,70,92–96] and while effective at predicting chronological age, they lack the ability to capture multidimensional physiological aging.[97–101] Our MM-clock integrates clinical parameters, functional readouts, and multi-omics data to model aging across multiple dimensions and extract core signals from heterogeneous noise. We further developed a proteome-based mini MM-clock for clinical use. Trajectory analysis revealed nonlinear aging dynamics with two major inflection periods (~40–50 and ~60–70 years): the first is characterized by hormonal fluctuations and lipid accumulation and the second by increased blood pressure, reduced bone density, and activation of the coagulation cascade. These inflection points may represent critical windows for geroprotective interventions, where intrinsic capacity and physiological resilience emerge as key determinants of healthy aging trajectories.

Our study establishes the age-dependent activation of the coagulation pathway as a primary driver—not merely a marker—of systemic aging. By integrating proteomics, Mendelian randomization, and functional validation, we identify liver-derived coagulation factors (e.g., F9 and F13B) as key components of a ''systemic aging driver module.'' Consistent with this finding, previous reports indicate that coagulation activity and thromboinflammatory responses increase with age.[102–108] These factors link the liver-vasculature-inflammation axis, driving endothelial senescence and multi-organ decline. Targeting the tissue-specific production or downstream pathways of these factors offers a dual-benefit strategy: mitigating age-related thrombosis while reversing vascular and systemic aging.

In summary, this work establishes a framework for quantitatively assessing human aging and potentially developing clinical endpoints for geroprotective interventions.[109–111] By establishing a non-invasive, pan-body, and multidimensional reference of human aging features, we have taken a step toward understanding, measuring, and intervening in human aging, which we hope will contribute to the journey of extending healthspan.

Limitations of the study

While our study advances the field of aging biomarkers, limitations remain. Key priorities include longitudinal validation across aging transitions, expanded cohort diversity, and integration of genomic/exposomic data. Organ-clock tissue specificity inferred from plasma requires caution, and cross-center data consistency demand attention to technical batch effects. The causal role of coagulation factor accumulation, though supported, requires further validation for clinical translation. Despite these early stage limitations, this study provides a foundation for scientifically measuring aging and pursuing related interventions.

RESOURCE AVAILABILITY

Lead contact

Further information and requests for resources and reagents should be directed to and will be fulfilled by the lead contact, Guang-Hui Liu (ghliu@ioz.ac.cn).

Materials availability

This study did not generate new, unique reagents.

Data and code availability

The data are stored and can be accessed in the Aging Biobank database of China National Center for Bioinformation (https://cbb.cncb.ac.cn/abb). In addition, all RNA-seq raw data can be accessed in the GSA-Human database: HRA011466 and HRA017906. Raw DNA methylation, proteomics, and metabolomics analysis data are deposited in the OMIX database under the following accession numbers: OMIX010076, OMIX016647, and OMIX010131. Raw metagenomic data are deposited in the GSA database under CRA: 025612.

Figure 6. Identification and characterization of accelerated and decelerated agers

(A) Schematic diagram illustrating the classification of fast agers and slow agers based on age pace.

(B) The correlation analysis based on individual age pace for the indicated aging clocks generated by multimodal information.

(C) The Pearson correlation between micro-clocks and macro-clocks. *p* values were calculated with a two-sided Wilcoxon signed-rank test.

(D) The classification of fast agers and slow agers for each aging clock. Representative fast agers are defined as individuals with consistent trends of accelerated aging and decelerated aging ($|\Delta clocks| \geq 3$). Δclock refers to the difference between the number of times an individual is identified as a fast and slow ager across all aging clocks.

(E and F) The DecelAging (DA)-related (E) and AccelAging (AA)-related (F) lifestyles. The DA- and AA-related lifestyles were identified using logistic regression, adjusted for age and sex.

(G and H) The DA- (G) and AA- (H) related clinical parameters. The DA- and AA-related clinical parameters were identified using logistic regression, adjusted for age and sex. The abbreviations for clinical parameters are listed in Table S1.

(I and J) The relative expression of DA- (I) and AA- (J) related proteins along with age pace. The bar plot on the right shows the enriched pathways for the proteins.

(K) The number of disease chapters with positively causal associations between age-associated AA and DA proteins. The protein-disease pairs were identified using Mendelian randomization analysis.

(L) Potential causal proteins for disease analyzed by Mendelian randomization, colored by disease chapter. Brown points below the bars indicate AA-related proteins, and green points indicate DA-related proteins.

See also Figure S6 and Tables S4 and S5.

Please cite this article in press as: Li et al., Multimodal clocks of human aging, Cell (2026), https://doi.org/10.1016/j.cell.2026.04.025

CellPress

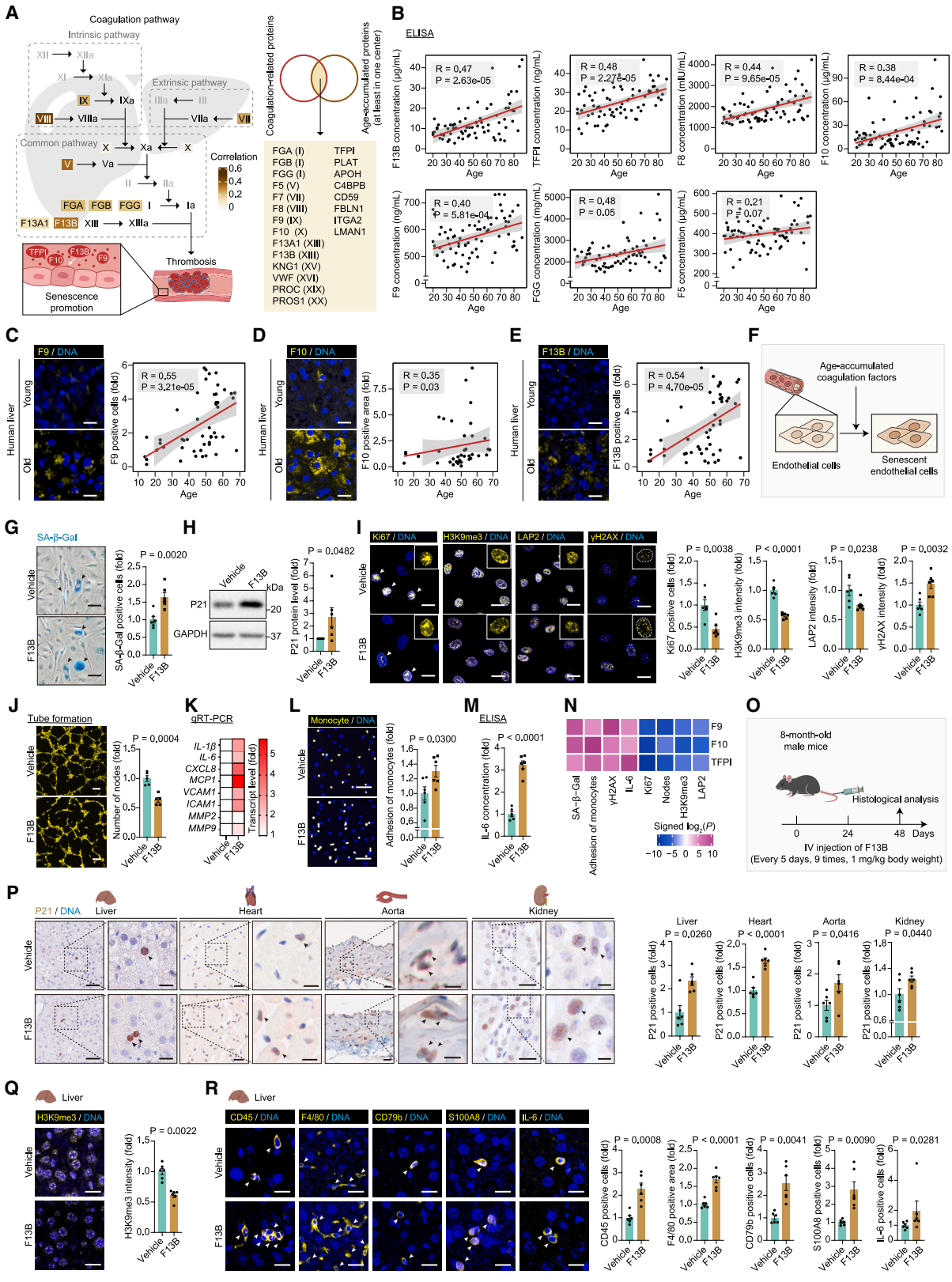

(legend on next page)

The code used in this study is available at https://github.com/Jiam1ng/mCAS.

ACKNOWLEDGMENTS

We would like to thank all the volunteers for their contribution to the study; the members of the Aging Biomarker Consortium for their invaluable feedback and guidance for the study; Zhongjun Guan, Binru Han, Xiao Zhou, Jieyu Wang, Xiuhong Nie, Yingqi Xing, Yingmin Chen, Li Yang, Wenjia Xu, Wei Wang, Zhanhao Zhang, Chao Wang, Mengyun Li, Xiaoxiao Wu, Wenwen Zhao, Junping Li, Wenjie Ying, Yanwen Chen, Tianxiang Yu, Wen-Jing Qiu, Li-Feng Xu, Xin-Qing Jiang, Zheng-Kai Wang, Si-Jia Chen, and Ya-Bing Hu for assisting with clinical laboratory testing; Jiaxin Xu for helping with histological staining; Yizhou Gao, Honghao Zhang, and Kunlin Du for assisting with questionnaire data entry; Jingyi Jia, Jiayi Liu, and Feifei Liu for their support in animal management; Lei Bai, Jing Lu, Liyun Zhao, Jing Chen, Qun Chu, Ying Yang, Luyang Tian, Shangyi Qiao, Xiuping Li, and Xuewei Chen for their administrative support; and Xili Chu and Guoli Chu for assisting with microscopic imaging. This work was supported by the National Natural Science Foundation of China (82488301), the National Key Research and Development Program of China (2022YFA1103700), the National Natural Science Foundation of China (82125011 and 82361148131), post-subsidy funds from the National Clinical Research Center, Ministry of Science and Technology of China (303-01-001-0272-01), the National Key Research and Development Program of China (2021YFA1101401, 2022YFA1103800, 2025YFC2511600, 2024YFC2706600, 2023YFC3605400, and 2023YFC3504301), the National Natural Science Foundation of China (82322025, 82422031, 82330044, 32341001, 32121001, 82192863, 82361148130, 82350710800, 82501885, 82271600, 82371570, 82401822, 82571781, 92468303, 82501882, 82501879, 32400968, 82471594, 82471586, 82170347, and 82421001), the Non-Communicable Chronic Diseases-National Science and Technology Major Project (2024ZD0530400), the Program of the Beijing Natural Science Foundation (JQ24044, Z240018, F251011, Z230011, 5264028, 5242024, and 5264026), the Shenzhen Medical Research Fund (C2406001, B2504003 and D2401003), the CAS Project for Young Scientists in Basic Research (YSBR-076, YSBR-012, and YSBR-036), the Strategic Priority Research Program of the Chinese Academy of Sciences (XDA0460403-05, XDC0200000, and XDB1470000), the New Cornerstone Science Foundation through the XPLORER PRIZE (2021-1045), the CAS Youth Interdisciplinary Team, Key Laboratory of Alzheimer's Disease of Zhejiang Province (ZJAD-2024001), the Beijing Nova Program (20250484873 and 20240484493), the Hainan Provincial Natural Science Foundation of China (825QN316), the Young Elite Scientists Sponsorship Program by CAST (YESS20240793), the Initiative Scientific Research Program, Institute of Zoology, CAS (2023IOZ0202, 2024IOZ0103, 2023IOZ0102, and 2024IOZ0101), the Excellent Young Talents Program of Capital Medical University (12500825), the Xuanwu Hospital Elite Cultivation Program (YC20250109), the Beijing Anzhen Hospital High Level Research Funding (2024AZB3002), Key Research and Development Project of Hainan Province (2023ICAC-YANFA), HNMU Start-up Package-ICAC (RP2500000375), the Space Medical Experiment Project of CMSP (HYZHXMH01012), the Natural Science Foundation of Zhejiang Province (ZCLKLY25H2901), the Key Science and Technology Projects of Quzhou City (2022K46), the STI2030-Major Projects (2021ZD0201801), the PWD&RPP-MRI (JYY2023-13), and the Shanghai Municipal Health Commission (2022JC013, 2023ZZ02021, 2022ZZ01008, and GWVI-11.1-26).

AUTHOR CONTRIBUTIONS

G.-H.L., Weiqi Zhang, G.Z., F.Z., J.P., Wei Zhang (author 107), J. Qu, and G.P. conceptualized the work and supervised the overall experiments. B.J., Wei Zhang (author 3), J. Hao, Z.L., X.-W.H., Jing Li, J.T., S.S., Y. Cai, K.Y., M.X., Jiaming Li, H.Y., Q. Zheng, H.H., L.Z., Junming Li, L.-J.X., Y. Chen, G.Q., W.L., Jun Ping, J. Zhou, M.Y., Mingjin Jiang, Ying Jing, W.-D.Y., X.Z., X. Chu, Y.H., Q. Zhao, Q. Wu, M.H., L.M., P. Liu, L. Zhang, Q.-C.Z., J. Qin, J. Lu, X.Y., S.Z., Y.X., H.R., W.Y., Z. Huang, J. Zhang, M.Z., P.C., J.D., Yu Zhang., T.Y., J.-L.Y., P.H., Z.Q., Y.L., J.S., C.-S.C., P. Li, D.L., X.X., Jiale Ping, J. Hu, X. Sun, J.A., Z.W., Yuxin Zhang, P.Y., T.N., Y. Yu, Z. He, H.Z., T.Z., Y. Yang., Q. Wang, F.L., X.J., X. Chen, and Jingyi Li participated in volunteer recruitment and sample collection and preparation. G.X. and J.Y. provided human liver samples. Jiaming Li, Q.J., Y. Zheng, X.L., and Z.Z. performed multimodal data analysis with guidance from S.M. and C.D. X.M. and X. Song analyzed the video data. Y.F. performed cell experiments. D.-D.G. performed ELISA experiments. Yaobin Jing and Y.F. performed the F13B injection on mice. Yaobin Jing, Y.F., R.W., B.Z., Y. Yu, Q. Wang., H.Z., X.S., J.H., P.Y., Y. Yang, L. Zhao,

Figure 7. Coagulation factors drive vascular and systemic aging

(A) Schematic of the coagulation cascade, with proteins showing age-associated changes highlighted in color (across the full cohort), and a heatmap showing age correlations of indicated coagulation-related proteins in plasma of individuals from different centers measured by mass spectrometry.
(B) ELISA analysis of indicated coagulation-related proteins (F13B, TFPI, F8, F10, F9, FGG, F5, and VWF) in human plasma. $n = 72$ individuals.
(C) IF staining analysis of F9 in human livers. $n = 50$ individuals. Scale bars, 10 μm.
(D) IF staining analysis of F10 in human livers. $n = 39$ individuals. Scale bars, 10 μm.
(E) IF staining analysis of F13B in human livers. $n = 50$ individuals. Scale bars, 10 μm.
(F) Schematic of coagulation-factor treatment in human aortic endothelial cells (HAECs).
(G) SA-β-Gal staining of HAECs treated with F13B. $n = 6$ independent experiments. Scale bars, 50 μm.
(H) Western blot analysis of P21 expression in HAECs treated with F13B. Glyceraldehyde-3-phosphate dehydrogenase (GAPDH) was used as a loading control. $n = 6$ independent experiments.
(I) IF staining analysis of Ki67, H3K9me3, LAP2, and γH2AX in HAECs treated with F13B. $n = 6$ independent experiments. Scale bars, 20 μm.
(J) Tube formation analysis of HAECs treated with F13B. $n = 5$ independent experiments. Scale bars, 200 μm.
(K) RT-qPCR analysis of SASP-related genes in HAECs treated with F13B. $n = 3$ independent experiments.
(L) Monocyte adhesion ability analysis of HAECs treated with F13B. $n = 6$ independent experiments. Scale bars, 100 μm.
(M) ELISA analysis of IL-6 expression in cell culture supernatant of HAECs treated with F13B (lower-middle) or TFPI. $n = 6$ independent experiments.
(N) Heatmap showing the effects of three coagulation factors (F9, F10, and TFPI) on endothelial senescence and inflammatory features in HAECs. Colors represent signed $\log_2$-transformed p values, where pink indicates a increase and blue indicates a decrease relative to control.
(O) Schematic of *in vivo* F13B injection in 8-month-old mice (every 5 days, 9 doses), with histological assays after the final dose.
(P) Immunohistochemistry (IHC) staining of P21 in mouse liver, heart, aorta, and kidney tissues. $n = 6$ mouse. Scale bars, 60 and 20 μm (liver), 25 and 10 μm (aorta), 20 and 10 μm (heart and kidney).
(Q) IF staining analysis of H3K9me3 in mouse liver. $n = 6$ mouse. Scale bars, 20 μm.
(R) IF staining analysis of CD45, F4/80, CD79b, S100A8, and IL-6 in mouse liver tissues. $n = 6$ mouse. Scale bars, 20 μm.
For (C)–(E), values were normalized to the mean value of individuals <30 years of age. For (B)–(E), the correlation between protein expression levels and age was evaluated via Spearman's correlation analysis. For (G)–(N) and (P)–(R), data are presented as the mean ± SEM. Intergroup differences were assessed by means of a two-tailed unpaired Student's t test, while a two-tailed unpaired Wilcoxon test was used for P21 (P) or IL-6 (R) positive cell percentage in liver and (Q), and a two-tailed unpaired Welch's test was used for (R) (CD79b or S100A8 positive cell percentage in liver).
See also Figures S7 and S8 and Table S6.

J.S., T.N., J. Zhou, and S.Z. participated in the sample collection of mouse tissues. Yaobin Jing, G.-H.L., Z.J., B.Z., D.-D.G., and R.W. conducted mouse tissue staining experiments. Yaobin Jing, R.W., and B.Z. performed experimental validation on human PBMCs. Z.J. and Mengmeng Jiang performed human liver-staining experiments. H.Y. and H.W. helped with the data analysis. Weiqi Zhang and Jiaming Li wrote the first draft. G.-H.L., Weiqi Zhang, G.Z., F.Z., Jun Ping, Wei Zhang (author 107), J. Qu., G.P., Y.-G.Y., F.H., W.S., Jianming Li, J.Y., S.W., M.S., and J.R. revised the manuscript and provided valuable suggestions for the study. All authors reviewed and agreed to submit the manuscript.

DECLARATION OF INTERESTS

The authors declare no competing interests.

DECLARATION OF GENERATIVE AI AND AI-ASSISTED TECHNOLOGIES IN THE WRITING PROCESS

During the preparation of this work, the authors used generative AI tools to assist with language editing and the creation of schematic illustrations. After using these tools, the authors carefully reviewed and edited the content and take full responsibility for the content of the publication.

STAR★METHODS

Detailed methods are provided in the online version of this paper and include the following:

- KEY RESOURCES TABLE
- EXPERIMENTAL MODEL AND STUDY PARTICIPANT DETAILS
  - Ethical statement
  - Human participants
- EXPERIMENTAL MOUSE MODELS
- METHOD DETAILS
  - Establishment of the standard cohort for the aging study
  - Collection and storage of biological samples
  - DNA methylation microarray
  - RNA isolation and bulk RNA-sequencing
  - Proteomics analysis
  - Untargeted metabolomic analysis
  - Metagenome DNA extraction and sequencing
  - Single-cell RNA sequencing (scRNA-seq) for PBMCs
  - Quantified reverse-transcription PCR (RT-qPCR)
  - Recombinant protein treatment in mice
  - Flow cytometric analyses
  - Immunofluorescence (IF) and immunohistochemistry (IHC) stainingr
  - Western blotting
  - Hematoxylin-eosin (HE) staining
  - Cell culture
  - HAEC tube-formation assay
  - Cell-adhesion assay
  - SA-β-Gal staining
  - Enzyme-linked immunosorbent assay (ELISA)
  - Quality control and preprocessing of physical examination data
  - Anthropometric and body composition measurements
  - Facial image acquisition
  - Facial wrinkle detection
  - Face-Clock construction
  - Neural and cognitive regulation
  - Magnetic resonance imaging analyses
  - Functional connectivity computation
  - MRI-Clock construction
  - Motor coordination assessment
  - Gait feature analysis
  - Cardiovascular aging clock construction
  - Retinal color fundus image collection
  - Retinal blood vessel segmentation
  - Retina aging clock construction
  - Pulmonary function testing
  - Core capacity clock (CC-clock) construction
  - DNA methylome data analysis
  - Transcriptome data analysis
  - Proteomics data analysis
  - Metabolomics data analysis
  - Metagenomic data analysis
  - Dyshomeostatic index (DHI) calculation
  - Aging-related differential feature identification
  - scRNA-seq data analysis
  - Bulk RNA-seq deconvolution for PBMC cell types
  - Pathway enrichment analysis
  - Single-layered multi-omics aging clock construction
  - Multimodal clock (MM-clock) construction
  - Feature importance analysis
  - Generalized additive model (GAM) fitting and trajectory clustering
  - Organ-associated aging clock construction
  - Fluctuation wave analysis of aging-associated clinical indicators and proteins
  - Proxy clock construction
  - Fast ager and slow ager classification
  - AA- and DA-related lifestyle identification
  - Clinical and proteomic characterization of fast and slow agers
  - Mendelian randomization analysis
  - Age-accumulated coagulation factor score calculation

SUPPLEMENTAL INFORMATION

Supplemental information can be found online at https://doi.org/10.1016/j.cell.2026.04.025.

Received: May 19, 2025
Revised: December 5, 2025
Accepted: April 10, 2026

REFERENCES

1. Kroemer, G., Maier, A.B., Cuervo, A.M., Gladyshev, V.N., Ferrucci, L., Gorbunova, V., Kennedy, B.K., Rando, T.A., Seluanov, A., Sierra, F., et al. (2025). From geroscience to precision geromedicine: Understanding and managing aging. Cell *188*, 2043–2062. https://doi.org/10.1016/j.cell.2025.03.011.
2. Moqri, M., Herzog, C., Poganik, J.R., Justice, J., Belsky, D.W., Higgins-Chen, A., Moskalev, A., Fuellen, G., Cohen, A.A., et al.; Biomarkers of Aging Consortium (2023). Biomarkers of aging for the identification and evaluation of longevity interventions. Cell *186*, 3758–3775. https://doi.org/10.1016/j.cell.2023.08.003.
3. Partridge, L., Deelen, J., and Slagboom, P.E. (2018). Facing up to the global challenges of ageing. Nature *561*, 45–56. https://doi.org/10.1038/s41586-018-0457-8.
4. Li, Y., Tian, X., Luo, J., Bao, T., Wang, S., and Wu, X. (2024). Molecular mechanisms of aging and anti-aging strategies. Cell Commun. Signal. *22*, 285. https://doi.org/10.1186/s12964-024-01663-1.
5. Guo, J., Huang, X., Dou, L., Yan, M., Shen, T., Tang, W., and Li, J. (2022). Aging and aging-related diseases: from molecular mechanisms to interventions and treatments. Signal Transduct. Target. Ther. *7*, 391. https://doi.org/10.1038/s41392-022-01251-0.
6. Khan, S.S., Singer, B.D., and Vaughan, D.E. (2017). Molecular and physiological manifestations and measurement of aging in humans. Aging Cell *16*, 624–633. https://doi.org/10.1111/acel.12601.
7. Yurkovich, J.T., Evans, S.J., Rappaport, N., Boore, J.L., Lovejoy, J.C., Price, N.D., and Hood, L.E. (2024). The transition from genomics to phenomics in personalized population health. Nat. Rev. Genet. *25*, 286–302. https://doi.org/10.1038/s41576-023-00674-x.

8. Aging; Biomarker Consortium, Bao, H., Cao, J., Chen, M., Chen, M., Chen, W., Chen, X., Chen, Y., Chen, Y., Chen, Y., et al. (2023). Biomarkers of aging. Sci. China Life Sci. *66*, 893–1066. https://doi.org/10.1007/s11427-023-2305-0.

9. Francisco, V., Pino, J., González-Gay, M.Á., Lago, F., Karppinen, J., Tervonen, O., Mobasheri, A., and Gualillo, O. (2022). A new immunometabolic perspective of intervertebral disc degeneration. Nat. Rev. Rheumatol. *18*, 47–60. https://doi.org/10.1038/s41584-021-00713-z.

10. Das, S., Ahmad, Z., Suryawanshi, A., and Kumar, A. (2022). Innate immunity dysregulation in aging eye and therapeutic interventions. Ageing Res. Rev. *82*, 101768. https://doi.org/10.1016/j.arr.2022.101768.

11. Janssen, T.A.H., Lowisz, C.V., and Phillips, S. (2025). From molecular to physical function: The aging trajectory. Curr. Res. Physiol. *8*, 100138. https://doi.org/10.1016/j.crphys.2024.100138.

12. Inoue, R., and Nishimune, H. (2023). Neuronal Plasticity and Age-Related Functional Decline in the Motor Cortex. Cells *12*, 2142. https://doi.org/10.3390/cells12172142.

13. Li, K.Z.H., and Lindenberger, U. (2002). Relations between aging sensory/sensorimotor and cognitive functions. Neurosci. Biobehav. Rev. *26*, 777–783. https://doi.org/10.1016/s0149-7634(02)00073-8.

14. Seidler, R.D., Bernard, J.A., Burutolu, T.B., Fling, B.W., Gordon, M.T., Gwin, J.T., Kwak, Y., and Lipps, D.B. (2010). Motor control and aging: links to age-related brain structural, functional, and biochemical effects. Neurosci. Biobehav. Rev. *34*, 721–733. https://doi.org/10.1016/j.neubiorev.2009.10.005.

15. Yin, C., Imms, P., Cheng, M., Amgalan, A., Chowdhury, N.F., Massett, R.J., Chaudhari, N.N., Chen, X., Thompson, P.M., Bogdan, P., et al. (2023). Anatomically interpretable deep learning of brain age captures domain-specific cognitive impairment. Proc. Natl. Acad. Sci. USA *120*, e2214634120. https://doi.org/10.1073/pnas.2214634120.

16. Aging Biomarker Consortium, Huang, N., Ge, M., Liu, X., Tian, X., Yin, P., Bao, Z., Cao, F., Shyh-Chang, N., Dong, B., et al. (2024). A framework of biomarkers for skeletal muscle aging: a consensus statement by the Aging Biomarker Consortium. Life Med. *3*, lnaf001. https://doi.org/10.1093/lifemedi/lnaf001.

17. Aging Biomarker Consortium, Yu, J., Zhang, Y., Zhang, T., Bi, Y., Chen, Y., Chen, Z., Dai, Z., Guo, F., Guo, L., et al. (2025). A framework of biomarkers for adipose tissue aging: a consensus statement by the Aging Biomarker Consortium. Life Med. *4*, lnaf027. https://doi.org/10.1093/lifemedi/lnaf027.

18. López-Otín, C., Blasco, M.A., Partridge, L., Serrano, M., and Kroemer, G. (2023). Hallmarks of aging: An expanding universe. Cell *186*, 243–278. https://doi.org/10.1016/j.cell.2022.11.001.

19. Lu, Y.R., Tian, X., and Sinclair, D.A. (2023). The Information Theory of Aging. Nat Aging *3*, 1486–1499. https://doi.org/10.1038/s43587-023-00527-6.

20. Liu, B., Qu, J., Zhang, W., Izpisua Belmonte, J.C., and Liu, G.H. (2022). A stem cell aging framework, from mechanisms to interventions. Cell Rep. *41*, 111451. https://doi.org/10.1016/j.celrep.2022.111451.

21. Gorgoulis, V., Adams, P.D., Alimonti, A., Bennett, D.C., Bischof, O., Bishop, C., Campisi, J., Collado, M., Evangelou, K., Ferbeyre, G., et al. (2019). Cellular Senescence: Defining a Path Forward. Cell *179*, 813–827. https://doi.org/10.1016/j.cell.2019.10.005.

22. Sun, S., Li, J., Wang, S., Li, J., Ren, J., Bao, Z., Sun, L., Ma, X., Zheng, F., Ma, S., et al. (2023). CHIT1-positive microglia drive motor neuron ageing in the primate spinal cord. Nature *624*, 611–620. https://doi.org/10.1038/s41586-023-06783-1.

23. Liu, X., Liu, Z., Wu, Z., Ren, J., Fan, Y., Sun, L., Cao, G., Niu, Y., Zhang, B., Ji, Q., et al. (2023). Resurrection of endogenous retroviruses during aging reinforces senescence. Cell *186*, 287–304.e26. https://doi.org/10.1016/j.cell.2022.12.017.

24. Brunet, A., Goodell, M.A., and Rando, T.A. (2023). Ageing and rejuvenation of tissue stem cells and their niches. Nat. Rev. Mol. Cell Biol. *24*, 45–62. https://doi.org/10.1038/s41580-022-00510-w.

25. Aging Biomarker Consortium, Zhang, L., Guo, J., Liu, Y., Sun, S., Liu, B., Yang, Q., Tao, J., Tian, X.-L., Pu, J., et al. (2023). A framework of biomarkers for vascular aging: a consensus statement by the Aging Biomarker Consortium. Life Med. *2*, lnad033. https://doi.org/10.1093/lifemedi/lnad033.

26. Aging Biomarker Consortium, Jia, Y.-J., Wang, J., Ren, J.-R., Chan, P., Chen, S., Chen, X.-C., Chhetri, J.K., Guo, J., Guo, Q., et al. (2023). A framework of biomarkers for brain aging: a consensus statement by the Aging Biomarker Consortium. Life Med. *2*, lnad017. https://doi.org/10.1093/lifemedi/lnad017.

27. Aging Biomarker Consortium, Fu, X., Wang, S., Wu, Y., Sun, Y., Liu, W., Xi, X., Li, G.-L., Liu, K., Yuan, W., et al. (2025). A biomarker framework for auditory system aging: the Aging Biomarker Consortium consensus statement. Life Med. *4*, lnaf011. https://doi.org/10.1093/lifemedi/lnaf011.

28. Oh, H.S.H., Rutledge, J., Nachun, D., Pálovics, R., Abiose, O., Moran-Losada, P., Channappa, D., Urey, D.Y., Kim, K., Sung, Y.J., et al. (2023). Organ aging signatures in the plasma proteome track health and disease. Nature *624*, 164–172. https://doi.org/10.1038/s41586-023-06802-1.

29. Wang, S., Zheng, Y., Li, J., Yu, Y., Zhang, W., Song, M., Liu, Z., Min, Z., Hu, H., Jing, Y., et al. (2020). Single-Cell Transcriptomic Atlas of Primate Ovarian Aging. Cell *180*, 585–600.e19. https://doi.org/10.1016/j.cell.2020.01.009.

30. Fan, Y., Zheng, Y., Zhang, Y., Xu, G., Liu, C., Hu, J., Ji, Q., Zhang, S., Fang, S., Lei, J., et al. (2025). ARID5A orchestrates cardiac aging and inflammation through MAVS mRNA stabilization. Nat CardioVasc Res. *4*, 602–623. https://doi.org/10.1038/s44161-025-00635-z.

31. Gao, Z., Li, M., Li, J., and Song, M. (2026). New paradigm for aging research: aging studies through innovative AI applications and interdisciplinary collaborations. Life Med. *5*, lnaf039. https://doi.org/10.1093/lifemedi/lnaf039.

32. Moqri, M., Herzog, C., Poganik, J.R., Ying, K., Justice, J.N., Belsky, D.W., Higgins-Chen, A.T., Chen, B.H., Cohen, A.A., Fuellen, G., et al. (2024). Validation of biomarkers of aging. Nat. Med. *30*, 360–372. https://doi.org/10.1038/s41591-023-02784-9.

33. Jylhävä, J., Pedersen, N.L., and Hägg, S. (2017). Biological Age Predictors. EBioMedicine *21*, 29–36. https://doi.org/10.1016/j.ebiom.2017.03.046.

34. Pu, F., Chen, W., Li, C., Fu, J., Gao, W., Ma, C., Cao, X., Zhang, L., Hao, M., Zhou, J., et al. (2024). Heterogeneous associations of multiplexed environmental factors and multidimensional aging metrics. Nat. Commun. *15*, 4921. https://doi.org/10.1038/s41467-024-49283-0.

35. Rutledge, J., Oh, H., and Wyss-Coray, T. (2022). Measuring biological age using omics data. Nat. Rev. Genet. *23*, 715–727. https://doi.org/10.1038/s41576-022-00511-7.

36. Bi, C., and Li, M. (2026). Proteomic aging atlas identified senoprotein as vascular and systemic senescent driver. Life Med. *5*, lnag003. https://doi.org/10.1093/lifemedi/lnag003.

37. Di Micco, R., Krizhanovsky, V., Baker, D., and d'Adda di Fagagna, F. (2021). Cellular senescence in ageing: from mechanisms to therapeutic opportunities. Nat. Rev. Mol. Cell Biol. *22*, 75–95. https://doi.org/10.1038/s41580-020-00314-w.

38. Kriukov, D., Efimov, E., Gelfand, M.S., Moskalev, A., and Khrameeva, E.E. (2025). Do we actually need aging clocks? NPJ Aging *12*, 15. https://doi.org/10.1038/s41514-025-00312-2.

39. Cohen, H.Y., Gorbunova, V., Horvath, S., Kennedy, B.K., Li, W., de Magalhães, J.P., Seluanov, A., Song, M., and Suzuki, K. (2025). Perspectives on the essence and drivers of aging. Life Med. *4*, lnaf006. https://doi.org/10.1093/lifemedi/lnaf006.

40. Nam, Y., Kim, J., Jung, S.H., Woerner, J., Suh, E.H., Lee, D.G., Shivakumar, M., Lee, M.E., and Kim, D. (2024). Harnessing Artificial Intelligence in Multimodal Omics Data Integration: Paving the Path for the Next Frontier in Precision Medicine. Annu. Rev. Biomed. Data Sci. *7*, 225–250. https://doi.org/10.1146/annurev-biodatasci-102523-103801.

41. Zheng, Y., Liu, Y., Yang, J., Dong, L., Zhang, R., Tian, S., Yu, Y., Ren, L., Hou, W., Zhu, F., et al. (2024). Multi-omics data integration using ratio-based quantitative profiling with Quartet reference materials. Nat. Biotechnol. *42*, 1133–1149. https://doi.org/10.1038/s41587-023-01934-1.

42. Gao, J., Liu, M., Lu, M., Zheng, Y., Wang, Y., Yang, J., Xue, X., Liu, Y., Tang, F., Wang, S., et al. (2024). Integrative analysis of transcriptome, DNA methylome, and chromatin accessibility reveals candidate therapeutic targets in hypertrophic cardiomyopathy. Protein Cell *15*, 796–817. https://doi.org/10.1093/procel/pwae032.

43. Ren, J., Song, M., Zhang, W., Cai, J.P., Cao, F., Cao, Z., Chan, P., Chen, C., Chen, G., Chen, H.Z., et al. (2023). The Aging Biomarker Consortium represents a new era for aging research in China. Nat. Med. *29*, 2162–2165. https://doi.org/10.1038/s41591-023-02444-y.

44. Li, J., Jiang, M., Wang, Q., Zheng, Z., Shen, J., Li, J., Xiong, M., Zheng, Y., Lu, X., Cai, Y., et al. (2025). The X-Age Project to construct a Chinese aging clock. Nat. Aging *5*, 1669–1685. https://doi.org/10.1038/s43587-025-00935-w.

45. Paszke, A., Chaurasia, A., Kim, S., and Culurciello, E. (2016). Enet: A deep neural network architecture for real-time semantic segmentation. Preprint at arXiv.

46. Li, J., Xiong, M., Fu, X.H., Fan, Y., Dong, C., Sun, X., Zheng, F., Wang, S.W., Liu, L., Xu, M., et al. (2023). Determining a multimodal aging clock in a cohort of Chinese women. Med. *4*, 825–848.e13. https://doi.org/10.1016/j.medj.2023.06.010.

47. Yang, J.H., Hayano, M., Griffin, P.T., Amorim, J.A., Bonkowski, M.S., Apostolides, J.K., Salfati, E.L., Blanchette, M., Munding, E.M., Bhakta, M., et al. (2023). Loss of epigenetic information as a cause of mammalian aging. Cell *186*, 305–326.e27. https://doi.org/10.1016/j.cell.2022.12.027.

48. Seale, K., Horvath, S., Teschendorff, A., Eynon, N., and Voisin, S. (2022). Making sense of the ageing methylome. Nat. Rev. Genet. *23*, 585–605. https://doi.org/10.1038/s41576-022-00477-6.

49. Booth, L.N., and Brunet, A. (2016). The Aging Epigenome. Mol. Cell *62*, 728–744. https://doi.org/10.1016/j.molcel.2016.05.013.

50. Wu, Z., Qu, J., and Liu, G.H. (2024). Roles of chromatin and genome instability in cellular senescence and their relevance to ageing and related diseases. Nat. Rev. Mol. Cell Biol. *25*, 979–1000. https://doi.org/10.1038/s41580-024-00775-3.

51. Garagnani, P., Bacalini, M.G., Pirazzini, C., Gori, D., Giuliani, C., Mari, D., Di Blasio, A.M., Gentilini, D., Vitale, G., Collino, S., et al. (2012). Methylation of ELOVL2 gene as a new epigenetic marker of age. Aging Cell *11*, 1132–1134. https://doi.org/10.1111/acel.12005.

52. Slieker, R.C., Relton, C.L., Gaunt, T.R., Slagboom, P.E., and Heijmans, B.T. (2018). Age-related DNA methylation changes are tissue-specific with ELOVL2 promoter methylation as exception. Epigenetics Chromatin *11*, 25. https://doi.org/10.1186/s13072-018-0191-3.

53. Ahadi, S., Zhou, W., Schüssler-Fiorenza Rose, S.M., Sailani, M.R., Contrepois, K., Avina, M., Ashland, M., Brunet, A., and Snyder, M. (2020). Personal aging markers and ageotypes revealed by deep longitudinal profiling. Nat. Med. *26*, 83–90. https://doi.org/10.1038/s41591-019-0719-5.

54. Moore, A., Chinnaiya, K., Kim, D.W., Brown, S., Stewart, I., Robins, S., Dowsett, G.K.C., Muir, C., Travaglio, M., Lewis, J.E., et al. (2022). Loss of Function of the Neural Cell Adhesion Molecule NrCAM Regulates Differentiation, Proliferation and Neurogenesis in Early Postnatal Hypothalamic Tanycytes. Front. Neurosci. *16*, 832961. https://doi.org/10.3389/fnins.2022.832961.

55. Ren, Y., Wang, X., Zhang, S., Hu, H., Quicksall, Z., Lee, S., Morganti, J.M., Johnson, L.A., Asmann, Y.W., and Zhao, N. (2023). Deconvolution reveals cell-type-specific transcriptomic changes in the aging mouse brain. Sci. Rep. *13*, 16855. https://doi.org/10.1038/s41598-023-44183-7.

56. Pekalski, M.L., García, A.R., Ferreira, R.C., Rainbow, D.B., Smyth, D.J., Mashar, M., Brady, J., Savinykh, N., Dopico, X.C., Mahmood, S., et al. (2017). Neonatal and adult recent thymic emigrants produce IL-8 and express complement receptors CR1 and CR2. JCI Insight *2*, e93739. https://doi.org/10.1172/jci.insight.93739.

57. Zhang, Y., Amaral, M.L., Zhu, C., Grieco, S.F., Hou, X., Lin, L., Buchanan, J., Tong, L., Preissl, S., Xu, X., et al. (2022). Single-cell epigenome analysis reveals age-associated decay of heterochromatin domains in excitatory neurons in the mouse brain. Cell Res. *32*, 1008–1021. https://doi.org/10.1038/s41422-022-00719-6.

58. Tserel, L., Kolde, R., Limbach, M., Tretyakov, K., Kasela, S., Kisand, K., Saare, M., Vilo, J., Metspalu, A., Milani, L., et al. (2015). Age-related profiling of DNA methylation in CD8+ T cells reveals changes in immune response and transcriptional regulator genes. Sci. Rep. *5*, 13107. https://doi.org/10.1038/srep13107.

59. Hardie, D.L., Baldwin, M.J., Naylor, A., Haworth, O.J., Hou, T.Z., Lax, S., Curnow, S.J., Willcox, N., MacFadyen, J., Isacke, C.M., et al. (2011). The stromal cell antigen CD248 (endosialin) is expressed on naive CD8+ human T cells and regulates proliferation. Immunology *133*, 288–295. https://doi.org/10.1111/j.1365-2567.2011.03437.x.

60. Ren, R., Deng, L., Xue, Y., Suzuki, K., Zhang, W., Yu, Y., Wu, J., Sun, L., Gong, X., Luan, H., et al. (2017). Visualization of aging-associated chromatin alterations with an engineered TALE system. Cell Res *27*, 483–504. https://doi.org/10.1038/cr.2017.18.

61. Ping, J., Qiao, Q., Gao, D.D., Li, Y., Fan, Y., Tian, Y., Xiong, M., Zheng, Q., Jiang, B., Li, J., et al. (2026). Human immune aging clock identifies RUNX1 as a decelerator of T cell senescence. Immunity *59*, 1039–1057.e1011. https://doi.org/10.1016/j.immuni.2026.02.007.

62. Bi, G., Wu, L., Huang, P., Islam, S., Heruth, D.P., Zhang, L.Q., Li, D.Y., Sampath, V., Huang, W., Simon, B.A., et al. (2018). Up-regulation of SFTPB expression and attenuation of acute lung injury by pulmonary epithelial cell-specific NAMPT knockdown. FASEB J. *32*, 3583–3596. https://doi.org/10.1096/fj.201701059R.

63. Desroziers, T., Prévot, G., Coulomb, A., Nau, V., Dastot-Le Moal, F., Duquesnoy, P., Héry, M., Le Borgne, A., Amselem, S., Legendre, M., et al. (2023). Hypomorphic pathogenic variant in SFTPB leads to adult pulmonary fibrosis. Eur. J. Hum. Genet. *31*, 1083–1087. https://doi.org/10.1038/s41431-023-01413-w.

64. Enomoto, T., Shirai, Y., Takeda, Y., Edahiro, R., Shichino, S., Nakayama, M., Takahashi-Itoh, M., Noda, Y., Adachi, Y., Kawasaki, T., et al. (2024). SFTPB in serum extracellular vesicles as a biomarker of progressive pulmonary fibrosis. JCI Insight *9*, e177937. https://doi.org/10.1172/jci.insight.177937.

65. Boucherat, O., Yokokawa, T., Krishna, V., Kalyana-Sundaram, S., Martineau, S., Breuils-Bonnet, S., Azhar, N., Bonilla, F., Gutstein, D., Potus, F., et al. (2022). Identification of LTBP-2 as a plasma biomarker for right ventricular dysfunction in human pulmonary arterial hypertension. Nat CardioVasc Res. *1*, 748–760. https://doi.org/10.1038/s44161-022-00113-w.

66. Enomoto, Y., Matsushima, S., Shibata, K., Aoshima, Y., Yagi, H., Meguro, S., Kawasaki, H., Kosugi, I., Fujisawa, T., Enomoto, N., et al. (2018). LTBP2 is secreted from lung myofibroblasts and is a potential biomarker for idiopathic pulmonary fibrosis. Clin. Sci. (Lond.) *132*, 1565–1580. https://doi.org/10.1042/CS20180435.

67. Wyres, K.L., Lam, M.M.C., and Holt, K.E. (2020). Population genomics of Klebsiella pneumoniae. Nat. Rev. Microbiol. *18*, 344–359. https://doi.org/10.1038/s41579-019-0315-1.

68. Wang, G., Zhao, G., Chao, X., Xie, L., and Wang, H. (2020). The Characteristic of Virulence, Biofilm and Antibiotic Resistance of Klebsiella

pneumoniae. Int. J. Environ. Res. Public Health *17*, 6278. https://doi.org/10.3390/ijerph17176278.

69. Hannum, G., Guinney, J., Zhao, L., Zhang, L., Hughes, G., Sadda, S., Klotzle, B., Bibikova, M., Fan, J.B., Gao, Y., et al. (2013). Genome-wide methylation profiles reveal quantitative views of human aging rates. Mol. Cell *49*, 359–367. https://doi.org/10.1016/j.molcel.2012.10.016.

70. Horvath, S. (2013). DNA methylation age of human tissues and cell types. Genome Biol. *14*, R115. https://doi.org/10.1186/gb-2013-14-10-r115.

71. Horvath, S., Oshima, J., Martin, G.M., Lu, A.T., Quach, A., Cohen, H., Felton, S., Matsuyama, M., Lowe, D., Kabacik, S., et al. (2018). Epigenetic clock for skin and blood cells applied to Hutchinson Gilford Progeria Syndrome and ex vivo studies. Aging (Albany, NY) *10*, 1758–1775. https://doi.org/10.18632/aging.101508.

72. Levine, M.E., Lu, A.T., Quach, A., Chen, B.H., Assimes, T.L., Bandinelli, S., Hou, L., Baccarelli, A.A., Stewart, J.D., Li, Y., et al. (2018). An epigenetic biomarker of aging for lifespan and healthspan. Aging (Albany, NY) *10*, 573–591. https://doi.org/10.18632/aging.101414.

73. Patel, R.S., Ghasemzadeh, N., Eapen, D.J., Sher, S., Arshad, S., Ko, Y.A., Veledar, E., Samady, H., Zafari, A.M., Sperling, L., et al. (2016). Novel Biomarker of Oxidative Stress Is Associated With Risk of Death in Patients With Coronary Artery Disease. Circulation *133*, 361–369. https://doi.org/10.1161/CIRCULATIONAHA.115.019790.

74. Patel, R.S., Al Mheid, I., Morris, A.A., Ahmed, Y., Kavtaradze, N., Ali, S., Dabhadkar, K., Brigham, K., Hooper, W.C., Alexander, R.W., et al. (2011). Oxidative stress is associated with impaired arterial elasticity. Atherosclerosis *218*, 90–95. https://doi.org/10.1016/j.atherosclerosis.2011.04.033.

75. Fukuda, M., Hata, A., Niwa, S., Hiramatsu, K., Honda, H., Nakagome, K., and Iwanami, A. (1996). Plasma vanillylmandelic acid level as an index of psychological stress response in normal subjects. Psychiatry Res. *63*, 7–16. https://doi.org/10.1016/0165-1781(96)02527-9.

76. Tohmola, N., Itkonen, O., Turpeinen, U., Joenväärä, S., Renkonen, R., and Hämäläinen, E. (2015). Preanalytical validation and reference values for a mass spectrometric assay of serum vanillylmandelic acid for screening of catecholamine secreting neuroendocrine tumors. Clin. Chim. Acta *446*, 206–212. https://doi.org/10.1016/j.cca.2015.03.041.

77. Malmström, E., Malmström, L., Hauri, S., Mohanty, T., Scott, A., Karlsson, C., Gueto-Tettay, C., Åhrman, E., Nozohoor, S., Tingstedt, B., et al. (2025). Human proteome distribution atlas for tissue-specific plasma proteome dynamics. Cell *188*, 2810–2822.e16. https://doi.org/10.1016/j.cell.2025.03.013.

78. Ding, Y., Zuo, Y., Zhang, B., Fan, Y., Xu, G., Cheng, Z., Ma, S., Fang, S., Tian, A., Gao, D., et al. (2025). Comprehensive human proteome profiles across a 50-year lifespan reveal aging trajectories and signatures. Cell *188*, 5763–5784.e26. https://doi.org/10.1016/j.cell.2025.06.047.

79. Uemura, M., Fujimura, Y., Ko, S., Matsumoto, M., Nakajima, Y., and Fukui, H. (2010). Pivotal role of ADAMTS13 function in liver diseases. Int. J. Hematol. *91*, 20–29. https://doi.org/10.1007/s12185-009-0481-4.

80. Leshchyns'ka, I., and Sytnyk, V. (2016). Synaptic Cell Adhesion Molecules in Alzheimer's Disease. Neural Plast. *2016*, 6427537. https://doi.org/10.1155/2016/6427537.

81. Sakurai, T. (2012). The role of NrCAM in neural development and disorders–beyond a simple glue in the brain. Mol. Cell. Neurosci. *49*, 351–363. https://doi.org/10.1016/j.mcn.2011.12.002.

82. Hodgkinson, C.P., Naidoo, V., Patti, K.G., Gomez, J.A., Schmeckpeper, J., Zhang, Z., Davis, B., Pratt, R.E., Mirotsou, M., and Dzau, V.J. (2013). Abi3bp is a multifunctional autocrine/paracrine factor that regulates mesenchymal stem cell biology. Stem Cells (Dayt. Ohio) *31*, 1669–1682. https://doi.org/10.1002/stem.1416.

83. Palta, S., Saroa, R., and Palta, A. (2014). Overview of the coagulation system. Indian J. Anaesth. *58*, 515–523. https://doi.org/10.4103/0019-5049.144643.

84. Zhang, H., Li, J., Yu, Y., Ren, J., Liu, Q., Bao, Z., Sun, S., Liu, X., Ma, S., Liu, Z., et al. (2023). Nuclear lamina erosion-induced resurrection of endogenous retroviruses underlies neuronal aging. Cell Rep. *42*, 113396. https://doi.org/10.1016/j.celrep.2023.113396.

85. Teschendorff, A.E., and Horvath, S. (2025). Epigenetic ageing clocks: statistical methods and emerging computational challenges. Nat. Rev. Genet. *26*, 350–368. https://doi.org/10.1038/s41576-024-00807-w.

86. Meyer, D.H., and Schumacher, B. (2021). BiT age: A transcriptome-based aging clock near the theoretical limit of accuracy. Aging Cell *20*, e13320. https://doi.org/10.1111/acel.13320.

87. Wang, J., Gao, Y., Wang, F., Zeng, S., Li, J., Miao, H., Wang, T., Zeng, J., Baptista-Hon, D., Monteiro, O., et al. (2024). Accurate estimation of biological age and its application in disease prediction using a multimodal image Transformer system. Proc. Natl. Acad. Sci. USA *121*, e2308812120. https://doi.org/10.1073/pnas.2308812120.

88. Wu, Z., Qu, J., and Liu, G.H. (2024). Roles of chromatin and genome instability in cellular senescence and their relevance to ageing and related diseases. Nat. Rev. Mol. Cell Biol. *25*, 979–1000. https://doi.org/10.1038/s41580-024-00775-3.

89. Wu, Z., Zhang, W., Qu, J., and Liu, G.H. (2024). Emerging epigenetic insights into aging mechanisms and interventions. Trends Pharmacol. Sci. *45*, 157–172. https://doi.org/10.1016/j.tips.2023.12.002.

90. Suryadevara, V., Hudgins, A.D., Rajesh, A., Pappalardo, A., Karpova, A., Dey, A.K., Hertzel, A., Agudelo, A., Rocha, A., Soygur, B., et al. (2024). SenNet recommendations for detecting senescent cells in different tissues. Nat. Rev. Mol. Cell Biol. *25*, 1001–1023. https://doi.org/10.1038/s41580-024-00738-8.

91. Wang, W., Zheng, Y., Sun, S., Li, W., Song, M., Ji, Q., Wu, Z., Liu, Z., Fan, Y., Liu, F., et al. (2021). A genome-wide CRISPR-based screen identifies KAT7 as a driver of cellular senescence. Sci. Transl. Med. *13*, eabd2655. https://doi.org/10.1126/scitranslmed.abd2655.

92. Simpson, D.J., and Chandra, T. (2021). Epigenetic age prediction. Aging Cell *20*, e13452. https://doi.org/10.1111/acel.13452.

93. Kabacik, S., Lowe, D., Fransen, L., Leonard, M., Ang, S.L., Whiteman, C., Corsi, S., Cohen, H., Felton, S., Bali, R., et al. (2022). The relationship between epigenetic age and the hallmarks of aging in human cells. Nat Aging *2*, 484–493. https://doi.org/10.1038/s43587-022-00220-0.

94. Lu, A.T., Quach, A., Wilson, J.G., Reiner, A.P., Aviv, A., Raj, K., Hou, L., Baccarelli, A.A., Li, Y., Stewart, J.D., et al. (2019). DNA methylation GrimAge strongly predicts lifespan and healthspan. Aging (Albany, NY) *11*, 303–327. https://doi.org/10.18632/aging.101684.

95. Bocklandt, S., Lin, W., Sehl, M.E., Sánchez, F.J., Sinsheimer, J.S., Horvath, S., and Vilain, E. (2011). Epigenetic predictor of age. PLoS One *6*, e14821. https://doi.org/10.1371/journal.pone.0014821.

96. Zhang, W., Qu, J., Liu, G.H., and Belmonte, J.C.I. (2020). The ageing epigenome and its rejuvenation. Nat. Rev. Mol. Cell Biol. *21*, 137–150. https://doi.org/10.1038/s41580-019-0204-5.

97. Lappalainen, T., Li, Y.I., Ramachandran, S., and Gusev, A. (2024). Genetic and molecular architecture of complex traits. Cell *187*, 1059–1075. https://doi.org/10.1016/j.cell.2024.01.023.

98. Han, J.J. (2024). The ticking of aging clocks. Trends Endocrinol. Metab. *35*, 11–22. https://doi.org/10.1016/j.tem.2023.09.007.

99. Cipriano, A., Moqri, M., Maybury-Lewis, S.Y., Rogers-Hammond, R., de Jong, T.A., Parker, A., Rasouli, S., Schöler, H.R., Sinclair, D.A., and Sebastiano, V. (2024). Mechanisms, pathways and strategies for rejuvenation through epigenetic reprogramming. Nat Aging *4*, 14–26. https://doi.org/10.1038/s43587-023-00539-2.

100. López-Otín, C., and Kroemer, G. (2021). Hallmarks of Health. Cell *184*, 33–63. https://doi.org/10.1016/j.cell.2020.11.034.

101. Field, A.E., Robertson, N.A., Wang, T., Havas, A., Ideker, T., and Adams, P.D. (2018). DNA Methylation Clocks in Aging: Categories, Causes, and Consequences. Mol. Cell *71*, 882–895. https://doi.org/10.1016/j.molcel.2018.08.008.

102. Dahlbäck, B. (2005). Blood coagulation and its regulation by anticoagulant pathways: genetic pathogenesis of bleeding and thrombotic diseases. J. Intern. Med. *257*, 209–223. https://doi.org/10.1111/j.1365-2796.2004.01444.x.

103. ten Cate, H., Hackeng, T.M., and García de Frutos, P. (2017). Coagulation factor and protease pathways in thrombosis and cardiovascular disease. Thromb. Haemost. *117*, 1265–1271. https://doi.org/10.1160/TH17-02-0079.

104. Zhang, K., Kurachi, S., and Kurachi, K. (2002). Genetic mechanisms of age regulation of protein C and blood coagulation. J. Biol. Chem. *277*, 4532–4540. https://doi.org/10.1074/jbc.M109524200.

105. Kurachi, K., Zhang, K., Ameri, A., Huo, J., Atoda, H., and Kurachi, S. (2000). Genetic and molecular mechanisms of age regulation (homeostasis) of blood coagulation. IUBMB Life *49*, 189–196. https://doi.org/10.1080/713803620.

106. Ferrucci, L., and Fabbri, E. (2018). Inflammageing: chronic inflammation in ageing, cardiovascular disease, and frailty. Nat. Rev. Cardiol. *15*, 505–522. https://doi.org/10.1038/s41569-018-0064-2.

107. Kurachi, S., Deyashiki, Y., Takeshita, J., and Kurachi, K. (1999). Genetic mechanisms of age regulation of human blood coagulation factor IX. Science *285*, 739–743. https://doi.org/10.1126/science.285.5428.739.

108. Cohen, H.J., Harris, T., and Pieper, C.F. (2003). Coagulation and activation of inflammatory pathways in the development of functional decline and mortality in the elderly. Am. J. Med. *114*, 180–187. https://doi.org/10.1016/s0002-9343(02)01484-5.

109. Lei, J., Xin, Z., Liu, N., Ning, T., Jing, Y., Qiao, Y., He, Z., Jiang, M., Yang, Y., Zhang, Z., et al. (2025). Senescence-resistant human mesenchymal progenitor cells counter aging in primates. Cell *188*, 5039–5061.e35. https://doi.org/10.1016/j.cell.2025.05.021.

110. Liu, L., Zheng, Z., You, W., Yang, P., Wen, Y., Qiao, Y., Ma, S., Zhang, H., Zhang, S., Xu, G., et al. (2026). Vitamin C inhibits ACSL4 to alleviate ferroaging in primates. Cell Metab. *38*, 673–693.e17. https://doi.org/10.1016/j.cmet.2026.02.010.

111. Yang, Y., Lu, X., Liu, N., Ma, S., Zhang, H., Zhang, Z., Yang, K., Jiang, M., Zheng, Z., Qiao, Y., et al. (2024). Metformin decelerates aging clock in male monkeys. Cell *187*, 6358–6378.e29. https://doi.org/10.1016/j.cell.2024.08.021.

112. Schneider, C.A., Rasband, W.S., and Eliceiri, K.W. (2012). NIH Image to ImageJ: 25 years of image analysis. Nat. Methods *9*, 671–675. https://doi.org/10.1038/nmeth.2089.

113. Fortin, J.P., Cullen, N., Sheline, Y.I., Taylor, W.D., Aselcioglu, I., Cook, P.A., Adams, P., Cooper, C., Fava, M., McGrath, P.J., et al. (2018). Harmonization of cortical thickness measurements across scanners and sites. Neuroimage *167*, 104–120. https://doi.org/10.1016/j.neuroimage.2017.11.024.

114. Wolf, F.A., Angerer, P., and Theis, F.J. (2018). SCANPY: large-scale single-cell gene expression data analysis. Genome Biol. *19*, 15. https://doi.org/10.1186/s13059-017-1382-0.

115. Wolock, S.L., Lopez, R., and Klein, A.M. (2019). Scrublet: Computational Identification of Cell Doublets in Single-Cell Transcriptomic Data. Cell Syst. *8*, 281–291.e9. https://doi.org/10.1016/j.cels.2018.11.005.

116. Paszke, A. (2019). Pytorch: An imperative style, high-performance deep learning library. Proceedings of the 33rd International Conference on Neural Information Processing Systems, 8026–8037.

117. Kim, D., Paggi, J.M., Park, C., Bennett, C., and Salzberg, S.L. (2019). Graph-based genome alignment and genotyping with HISAT2 and HISAT-genotype. Nat. Biotechnol. *37*, 907–915. https://doi.org/10.1038/s41587-019-0201-4.

118. Chen, T., Li, M., Li, Y., Lin, M., Wang, N., Wang, M., Xiao, T., Xu, B., Zhang, C., and Zhang, Z. (2015). Mxnet: A flexible and efficient machine learning library for heterogeneous distributed systems. Preprint at arXiv.

119. Howard, A.G., Zhu, M., Chen, B., Kalenichenko, D., Wang, W., Weyand, T., Andreetto, M., and Adam, H. (2017). Mobilenets: Efficient convolutional neural networks for mobile vision applications. Preprint at arXiv.

120. Li, X., Morgan, P.S., Ashburner, J., Smith, J., and Rorden, C. (2016). The first step for neuroimaging data analysis: DICOM to NIfTI conversion. J. Neurosci. Methods *264*, 47–56. https://doi.org/10.1016/j.jneumeth.2016.03.001.

121. Esteban, O., Markiewicz, C.J., Blair, R.W., Moodie, C.A., Isik, A.I., Erramuzpe, A., Kent, J.D., Goncalves, M., DuPre, E., Snyder, M., et al. (2019). fMRIPrep: a robust preprocessing pipeline for functional MRI. Nat. Methods *16*, 111–116. https://doi.org/10.1038/s41592-018-0235-4.

122. Jenkinson, M., Beckmann, C.F., Behrens, T.E.J., Woolrich, M.W., and Smith, S.M. (2012). Fsl. Neuroimage *62*, 782–790. https://doi.org/10.1016/j.neuroimage.2011.09.015.

123. Bashyam, V.M., Erus, G., Doshi, J., Habes, M., Nasrallah, I., Truelove-Hill, M., Srinivasan, D., Mamourian, L., Pomponio, R., Fan, Y., et al. (2020). MRI signatures of brain age and disease over the lifespan based on a deep brain network and 14 468 individuals worldwide. Brain *143*, 2312–2324. https://doi.org/10.1093/brain/awaa160.

124. Yao, Z., He, K., Zhou, H., Zhang, Z., Zhu, G., Xing, C., Zhang, J., Zhang, Z., Shao, B., Tao, Y., et al. (2020). Eye3DVas: three-dimensional reconstruction of retinal vascular structures by integrating fundus image features. In Frontiers in Optics/Laser Science (Optica Publishing Group), pp. JTu1B.22.

125. Fu, H., Wang, B., Shen, J., Cui, S., Xu, Y., Liu, J., and Shao, L. (2019). Evaluation of retinal image quality assessment networks in different color-spaces. In Medical Image Computing and Computer Assisted Intervention – MICCAI 2019 - 22nd International Conference, Proceedings (Springer), pp. 48–56.

126. Miyake, M., Akiyama, M., Kashiwagi, K., Sakamoto, T., and Oshika, T. (2022). Japan Ocular Imaging Registry: a national ophthalmology real-world database. Jpn. J. Ophthalmol. *66*, 499–503. https://doi.org/10.1007/s10384-022-00941-0.

127. Simon, N., Friedman, J., Hastie, T., and Tibshirani, R. (2011). Regularization Paths for Cox's Proportional Hazards Model via Coordinate Descent. J. Stat. Softw. *39*, 1–13. https://doi.org/10.18637/jss.v039.i05.

128. Zhou, W., Triche, T.J., Jr., Laird, P.W., and Shen, H. (2018). SeSAMe: reducing artifactual detection of DNA methylation by Infinium BeadChips in genomic deletions. Nucleic Acids Res. *46*, e123. https://doi.org/10.1093/nar/gky691.

129. Liao, Y., Smyth, G.K., and Shi, W. (2014). featureCounts: an efficient general purpose program for assigning sequence reads to genomic features. Bioinformatics *30*, 923–930. https://doi.org/10.1093/bioinformatics/btt656.

130. Love, M.I., Huber, W., and Anders, S. (2014). Moderated estimation of fold change and dispersion for RNA-seq data with DESeq2. Genome Biol. *15*, 550. https://doi.org/10.1186/s13059-014-0550-8.

131. Kong, A.T., Leprevost, F.V., Avtonomov, D.M., Mellacheruvu, D., and Nesvizhskii, A.I. (2017). MSFragger: ultrafast and comprehensive peptide identification in mass spectrometry-based proteomics. Nat. Methods *14*, 513–520. https://doi.org/10.1038/nmeth.4256.

132. Demichev, V., Messner, C.B., Vernardis, S.I., Lilley, K.S., and Ralser, M. (2020). DIA-NN: neural networks and interference correction enable deep proteome coverage in high throughput. Nat. Methods *17*, 41–44. https://doi.org/10.1038/s41592-019-0638-x.

133. Feng, Z., Fang, P., Zheng, H., and Zhang, X. (2023). DEP2: an upgraded comprehensive analysis toolkit for quantitative proteomics data. Bioinformatics *39*, btad526. https://doi.org/10.1093/bioinformatics/btad526.

134. Beghini, F., McIver, L.J., Blanco-Míguez, A., Dubois, L., Asnicar, F., Maharjan, S., Mailyan, A., Manghi, P., Scholz, M., Thomas, A.M., et al. (2021). Integrating taxonomic, functional, and strain-level profiling of diverse microbial communities with bioBakery 3. eLife *10*, e65088. https://doi.org/10.7554/eLife.65088.

135. Langmead, B., and Salzberg, S.L. (2012). Fast gapped-read alignment with Bowtie 2. Nat. Methods *9*, 357–359. https://doi.org/10.1038/nmeth.1923.

136. Blanco-Míguez, A., Beghini, F., Cumbo, F., McIver, L.J., Thompson, K.N., Zolfo, M., Manghi, P., Dubois, L., Huang, K.D., Thomas, A.M., et al. (2023). Extending and improving metagenomic taxonomic profiling with uncharacterized species using MetaPhlAn 4. Nat. Biotechnol. *41*, 1633–1644. https://doi.org/10.1038/s41587-023-01688-w.

137. Breiman, L. (2001). Random Forests. Mach. Learn. *45*, 5–32. https://doi.org/10.1023/A:1010933404324.

138. Newman, A.M., Steen, C.B., Liu, C.L., Gentles, A.J., Chaudhuri, A.A., Scherer, F., Khodadoust, M.S., Esfahani, M.S., Luca, B.A., Steiner, D., et al. (2019). Determining cell type abundance and expression from bulk tissues with digital cytometry. Nat. Biotechnol. *37*, 773–782. https://doi.org/10.1038/s41587-019-0114-2.

139. Zhou, Y., Zhou, B., Pache, L., Chang, M., Khodabakhshi, A.H., Tanaseichuk, O., Benner, C., and Chanda, S.K. (2019). Metascape provides a biologist-oriented resource for the analysis of systems-level datasets. Nat. Commun. *10*, 1523. https://doi.org/10.1038/s41467-019-09234-6.

140. Pang, Z., Zhou, G., Ewald, J., Chang, L., Hacariz, O., Basu, N., and Xia, J. (2022). Using MetaboAnalyst 5.0 for LC-HRMS spectra processing, multi-omics integration and covariate adjustment of global metabolomics data. Nat. Protoc. *17*, 1735–1761. https://doi.org/10.1038/s41596-022-00710-w.

141. Lehallier, B., Gate, D., Schaum, N., Nanasi, T., Lee, S.E., Yousef, H., Moran Losada, P., Berdnik, D., Keller, A., Verghese, J., et al. (2019). Undulating changes in human plasma proteome profiles across the lifespan. Nat. Med. *25*, 1843–1850. https://doi.org/10.1038/s41591-019-0673-2.

142. Hemani, G., Zheng, J., Elsworth, B., Wade, K.H., Haberland, V., Baird, D., Laurin, C., Burgess, S., Bowden, J., Langdon, R., et al. (2018). The MR-Base platform supports systematic causal inference across the human phenome. eLife *7*, e34408. https://doi.org/10.7554/eLife.34408.

143. World Health Organization (2015). World Report on Ageing and Health (World Health Organization).

144. Liu, X., Tong, X., Zou, Y., Lin, X., Zhao, H., Tian, L., Jie, Z., Wang, Q., Zhang, Z., Lu, H., et al. (2022). Mendelian randomization analyses support causal relationships between blood metabolites and the gut microbiome. Nat. Genet. *54*, 52–61. https://doi.org/10.1038/s41588-021-00968-y.

145. Jing, Y., Jiang, X., Ji, Q., Wu, Z., Wang, W., Liu, Z., Guillen-Garcia, P., Esteban, C.R., Reddy, P., Horvath, S., et al. (2023). Genome-wide CRISPR activation screening in senescent cells reveals SOX5 as a driver and therapeutic target of rejuvenation. Cell Stem Cell *30*, 1452–1471.e10. https://doi.org/10.1016/j.stem.2023.09.007.

146. Ma, S., Wang, S., Ye, Y., Ren, J., Chen, R., Li, W., Li, J., Zhao, L., Zhao, Q., Sun, G., et al. (2022). Heterochronic parabiosis induces stem cell revitalization and systemic rejuvenation across aged tissues. Cell Stem Cell *29*, 990–1005.e10. https://doi.org/10.1016/j.stem.2022.04.017.

147. Zhang, X., Zhang, C., Qiao, M., Cheng, C., Tang, N., Lu, S., Sun, W., Xu, B., Cao, Y., Wei, X., et al. (2022). Depletion of BATF in CAR-T cells enhances antitumor activity by inducing resistance against exhaustion and formation of central memory cells. Cancer Cell *40*, 1407–1422.e7. https://doi.org/10.1016/j.ccell.2022.09.013.

148. Rains, J.L., and Jain, S.K. (2011). Hyperketonemia increases monocyte adhesion to endothelial cells and is mediated by LFA-1 expression in monocytes and ICAM-1 expression in endothelial cells. Am. J. Physiol., Endocrinol. Metab. *301*, E298–E306. https://doi.org/10.1152/ajpendo.00038.2011.

149. Nie, C., Li, Y., Li, R., Yan, Y., Zhang, D., Li, T., Li, Z., Sun, Y., Zhen, H., Ding, J., et al. (2022). Distinct biological ages of organs and systems identified from a multi-omics study. Cell Rep. *38*, 110459. https://doi.org/10.1016/j.celrep.2022.110459.

150. Tian, Y.E., Cropley, V., Maier, A.B., Lautenschlager, N.T., Breakspear, M., and Zalesky, A. (2023). Heterogeneous aging across multiple organ systems and prediction of chronic disease and mortality. Nat. Med. *29*, 1221–1231. https://doi.org/10.1038/s41591-023-02296-6.

151. Moon, J., Chung, H., and Jang, I. (2024). Facial Wrinkle Segmentation for Cosmetic Dermatology: Pretraining with Texture Map-Based Weak Supervision. In Pattern Recognition: 27th International Conference, ICPR 2024, Proceedings, Part XXVIII (Springer), pp. 319–334.

152. Guo, J., Deng, J., Lattas, A., and Zafeiriou, S. (2021). Sample and computation redistribution for efficient face detection. Preprint at arXiv.

153. Botvinik-Nezer, R., Holzmeister, F., Camerer, C.F., Dreber, A., Huber, J., Johannesson, M., Kirchler, M., Iwanir, R., Mumford, J.A., Adcock, R.A., et al. (2020). Variability in the analysis of a single neuroimaging dataset by many teams. Nature *582*, 84–88. https://doi.org/10.1038/s41586-020-2314-9.

154. Abraham, A., Pedregosa, F., Eickenberg, M., Gervais, P., Mueller, A., Kossaifi, J., Gramfort, A., Thirion, B., and Varoquaux, G. (2014). Machine learning for neuroimaging with scikit-learn. Front. Neuroinform. *8*, 14. https://doi.org/10.3389/fninf.2014.00014.

155. Desikan, R.S., Ségonne, F., Fischl, B., Quinn, B.T., Dickerson, B.C., Blacker, D., Buckner, R.L., Dale, A.M., Maguire, R.P., Hyman, B.T., et al. (2006). An automated labeling system for subdividing the human cerebral cortex on MRI scans into gyral based regions of interest. Neuroimage *31*, 968–980. https://doi.org/10.1016/j.neuroimage.2006.01.021.

156. Jenkinson, M., and Smith, S. (2001). A global optimisation method for robust affine registration of brain images. Med. Image Anal. *5*, 143–156. https://doi.org/10.1016/s1361-8415(01)00036-6.

157. Jenkinson, M., Bannister, P., Brady, M., and Smith, S. (2002). Improved optimization for the robust and accurate linear registration and motion correction of brain images. Neuroimage *17*, 825–841. https://doi.org/10.1016/s1053-8119(02)91132-8.

158. Montero-Odasso, M., Schapira, M., Soriano, E.R., Varela, M., Kaplan, R., Camera, L.A., and Mayorga, L.M. (2005). Gait velocity as a single predictor of adverse events in healthy seniors aged 75 years and older. J. Gerontol. A Biol. Sci. Med. Sci. *60*, 1304–1309. https://doi.org/10.1093/gerona/60.10.1304.

159. Prince, F., Corriveau, H., Hébert, R., and Winter, D.A. (1997). Gait in the elderly. Gait Posture *5*, 128–135. https://doi.org/10.1016/S0966-6362(97)01118-1.

160. D'Antonio, E., Taborri, J., Palermo, E., Rossi, S., and Patanè, F. (2020). A markerless system for gait analysis based on OpenPose library. In 2020 IEEE International Instrumentation and Measurement Technology Conference (I2MTC) (IEEE), pp. 1–6.

161. Sun, Z., Zhu, X., Lei, Z., and Ma, X. (2022). Caged Monkey Dataset: A New Benchmark for Caged Monkey Pose Estimation. In Pattern Recognition and Computer Vision: 5th Chinese Conference, PRCV 2022 (Springer), pp. 694–706.

162. Yang, S., Chen, Z.-Y., Liang, K.-W., Qin, C.-J., Yang, Y., Fan, W.-X., Jie, C.-L., and Ma, X.-B. (2023). BARN: Behavior-Aware Relation Network for multi-label behavior detection in socially housed macaques. Zool. Res. *44*, 1026–1038. https://doi.org/10.24272/j.issn.2095-8137.2022.485.

163. Liu, Z., Ji, Q., Ren, J., Yan, P., Wu, Z., Wang, S., Sun, L., Wang, Z., Li, J., Sun, G., et al. (2022). Large-scale chromatin reorganization reactivates placenta-specific genes that drive cellular aging. Dev. Cell *57*, 1347–1368.e12. https://doi.org/10.1016/j.devcel.2022.05.004.

164. Zhang, Y., Parmigiani, G., and Johnson, W.E. (2020). ComBat-seq: batch effect adjustment for RNA-seq count data. NAR Genom. Bioinform. *2*, lqaa078. https://doi.org/10.1093/nargab/lqaa078.

165. Bairoch, A., and Apweiler, R. (2000). The SWISS-PROT protein sequence database and its supplement TrEMBL in 2000. Nucleic Acids Res. *28*, 45–48. https://doi.org/10.1093/nar/28.1.45.

166. Angelidis, I., Simon, L.M., Fernandez, I.E., Strunz, M., Mayr, C.H., Greiffo, F.R., Tsitsiridis, G., Ansari, M., Graf, E., Strom, T.M., et al. (2019). An atlas

of the aging lung mapped by single cell transcriptomics and deep tissue proteomics. Nat. Commun. *10*, 963. https://doi.org/10.1038/s41467-019-08831-9.

167. Karp, P.D., Billington, R., Caspi, R., Fulcher, C.A., Latendresse, M., Kothari, A., Keseler, I.M., Krummenacker, M., Midford, P.E., Ong, Q., et al. (2019). The BioCyc collection of microbial genomes and metabolic pathways. Brief. Bioinform. *20*, 1085–1093. https://doi.org/10.1093/bib/bbx085.

168. Davey Smith, G., and Hemani, G. (2014). Mendelian randomization: genetic anchors for causal inference in epidemiological studies. Hum. Mol. Genet. *23*, R89–R98. https://doi.org/10.1093/hmg/ddu328.

169. Sun, J., Zhao, J., Jiang, F., Wang, L., Xiao, Q., Han, F., Chen, J., Yuan, S., Wei, J., Larsson, S.C., et al. (2023). Identification of novel protein biomarkers and drug targets for colorectal cancer by integrating human plasma proteome with genome. Genome Med. *15*, 75. https://doi.org/10.1186/s13073-023-01229-9.

170. Zheng, X., Tian, Z., Che, X., Zhang, X., Xiang, Y., Ge, Z., Zhai, Z., Ma, Q., and Pan, J. (2025). DMRdb: a disease-centric Mendelian randomization database for systematically assessing causal relationships of diseases with genes, proteins, CpG sites, metabolites and other diseases. Nucleic Acids Res. *53*, D1363–D1371. https://doi.org/10.1093/nar/gkae853.

171. Hemani, G., Tilling, K., and Davey Smith, G. (2017). Orienting the causal relationship between imprecisely measured traits using GWAS summary data. PLoS Genet. *13*, e1007081. https://doi.org/10.1371/journal.pgen.1007081.

STAR★METHODS

KEY RESOURCES TABLE

REAGENT or RESOURCE	SOURCE	IDENTIFIER
Antibodies		
PE/Cyanine7 anti-human CD3	BioLegend	Cat# 317334; RRID: AB_2561452
PE/Dazzle™ 594 anti-human CD4	BioLegend	Cat# 344640; RRID: AB_2616993
APC anti-human CD8	BioLegend	Cat# 344722; RRID: AB_2075388
PE anti-human CD197 (CCR7)	BioLegend	Cat# 353204; RRID: AB_10913813
Brilliant Violet 605™ anti-human CD45RA	BioLegend	Cat# 304134; RRID: AB_2563814
APC/Cyanine7 anti-human CD27	BioLegend	Cat# 302816; RRID: AB_571977
Brilliant Violet 421™ anti-human CD28	BioLegend	Cat# 302930; RRID: AB_2561910
eBioscience™ Fixable Viability Dye eFluor™ 506	Thermo Fisher Scientific	Cat# 65-0866-14
CD57 Monoclonal Antibody (TB01 (TBO1))	Thermo Fisher Scientific	Cat# 11-0577-42; RRID: AB_1311193
Donkey anti-Mouse IgG (H+L) Highly Cross-Adsorbed Secondary Antibody, Alexa Fluor 568	Thermo Fisher Scientific	Cat# A10037; RRID: AB_11180865
Donkey anti-Rabbit IgG (H+L) Highly Cross-Adsorbed Secondary Antibody, Alexa Fluor 488	Thermo Fisher Scientific	Cat# A21206; RRID: AB_2535792
Anti-phospho-Histone H2A.X (Ser139) Antibody	Millipore	Cat# 05-636; RRID: AB_309864
Anti-H3K9me3 Antibody	Abcam	Cat# 8898; RRID: AB_306848
Anti-F9 antibody	Abcam	Cat# 236279
Anti-F10 antibody	Abcam	Cat# 79929; RRID: AB_1658723
Anti-F13B antibody	Immunoway	Cat# YT5701
Anti-Ki67 antibody	Abcam	Cat# ab15580; RRID: AB_443209
Anti-LAP2 antibody	Becton, Dickinson and Company	Cat# 611000; RRID: AB_398313
Anti-GAPDH (G-9) antibody	Santa Cruz	Cat# 365062; RRID: AB_10847862
Anti-IL-6 antibody	Abcam	Cat# 9324; RRID: AB_307175
Anti-IL-1 beta antibody	Santa Cruz	Cat# 52012; RRID: AB_629741
Anti-CD45 antibody	Abcam	Cat# 10558; RRID: AB_442810
Anti-CD79b antibody	Cell Signaling Technology, Inc.	Cat# 96024S; RRID: AB_2800254
Anti-S100A8 antibody	Abcam	Cat# 92331; RRID: AB_2050283
Anti-MMTV antibody	Novus	Cat# 44179; RRID: AB_3307963
Anti-P21 antibody	Abcam	Cat# 188224; RRID: AB_2734729
Biological samples		
Human blood samples	Xuanwu Hospital, Beijing; Quzhou People's Hospital, Quzhou; The First Affiliated Hospital, Nanchang; Ningbo Hangzhou Bay Hospital, Ningbo.	N/A
Healthy adult liver tissue	West China Hospital of Sichuan University	N/A
Chemicals, peptides, and recombinant proteins		
Endothelial Cell Medium	ScienCell	Cat# 1001
Collagen	Advanced BioMatrix	Cat# 5005
Accumax	Millipore	Cat# SCR006
Accutase	Gibco	Cat# A11105

(*Continued on next page*)

Please cite this article in press as: Li et al., Multimodal clocks of human aging, Cell (2026), https://doi.org/10.1016/j.cell.2026.04.025

Continued

REAGENT or RESOURCE	SOURCE	IDENTIFIER
Matrigel	Becton, Dickinson and Company	Cat# 354230
Calcium-AM	Invitrogen	Cat# C3099
Donkey serum	Jackson ImmunoResearch	Cat# 017-000-121
Fetal Bovine Serum	Gemini	Cat# 900-108
D-PBS	Gibco	Cat# 21600069
X-gal	MedChemExpress	Cat# HY15934
DMSO	SIGMA	Cat# D2650
4% paraformaldehyde (PFA)	DINGGUO	Cat# AR-0211
TRIzol	Ambion	Cat# 15596018
SYBR qPCR SuperMix Plus	NovoStart	Cat# E096-01A
Ficoll	SIGMA	Cat# F4375
Triton X-100	Solarbio	Cat# T8200
Cell Staining Buffer	BioLegend	Cat# 420201
Fixation Buffer	BioLegend	Cat# 420801
Hoechst 33342	Thermo Fisher Scientific	Cat# H3570
Antifade Mounting Medium	Vector	Cat# H-1000
Coagulation Factor X/F10 Protein	MedChemExpress	Cat# HY-P7860
Coagulation factor IX/F9 Protein	MedChemExpress	Cat# HY-P70231
TFPI	MedChemExpress	Cat# HY-P77227
Coagulation factor XIII B/F13B	MedChemExpress	Cat# HY-P74238
Critical commercial assays		
HiScript III RT SuperMix for qPCR (+gDNA wiper)	Vazyme	Cat# R323
BCA Protein Assay Kit	DINGGUO	Cat# BCA02
Human Coagulation factor XIII B chain (F13B) ELISA kit	CUSABIO	Cat# CSB-EL007922HU
Human TFPI (Tissue Factor Pathway Inhibitor) ELISA Kit	Elabscience	Cat# E-EL-H6163
Human F8 (Coagulation Factor VIII) ELISA Kit	Elabscience	Cat# E-EL-H3641
Human coagulation factor X, FX ELISA Kit	CUSABIO	Cat# CSB-E08440h
Human F9 (Coagulation Factor IX) ELISA Kit	Elabscience	Cat# E-EL-H0760
Human Fibrinogen Gamma Chain (FGG) ELISA Kit	CUSABIO	Cat# CSB-E13319h
Human F5 (Coagulation Factor V) ELISA Kit	ELK Biotechnology	Cat# ELK1765
Human von Willebrand Factor, vWF ELISA Kit	CUSABIO	Cat# CSB-E08437h
ELISA MAX™ Deluxe Set Human IL-6	BioLegend	Cat# 430506
Deposited data		
Raw data for RNA-seq	This study	HRA011466
Raw data for DNA methylation	This study	OMIX010076
Raw data for proteomics analysis	This study	OMIX010129
Raw data for metabolomics analysis	This study	OMIX010131
Raw data for metagenome analysis	This study	CRA025612
Experimental models: Cell lines		
Human Aortic Endothelial Cell (HAEC)	Lonza	Cat# CC-2535
Human Acute Monocytic Leukemia Cell (THP-1)	Pricella	Cat# CL-0233

(*Continued on next page*)

Continued

REAGENT or RESOURCE	SOURCE	IDENTIFIER
Oligonucleotides		
SYT11-F	AGAAGTGCATCAGCAGAGGG	N/A
SYT11-R	TCTTGGCAATGCGCTTTCTG	N/A
MiR34AHG-F	GCCCATCTTTCTTTGCACCT	N/A
MiR34AHG-R	CGGCCTTCTCATCTGGACT	N/A
CDKN2A-F	GCCGACCCCGCCACTCTCACC	N/A
CDKN2A-R	CCCAGGCATCGCGCACGTCCA	N/A
FIGN-F	ATGGCCAGTGTTGAGGTCAG	N/A
FIGN-R	TGGCCACAAGAAAAGAGGCA	N/A
NRCAM-F	TCAGGGCTGGTTCATTGGTC	N/A
NRCAM-R	GGCTTGTGGTCTTCTGCATC	N/A
CACHD1-F	CCAATGCAGAGAACCGAAACCC	N/A
CACHD1-R	TCACTGTCCACCATGCACCA	N/A
ROBO1-F	CGCGGGTATCAGAAAAGTCC	N/A
ROBO1-R	ACAATCAGCTGGGCGAC	N/A
CD248-F	GTATACCACGCCCTTCCACC	N/A
CD248-R	CTCCACACATTCGTGTTCGC	N/A
FBLN2-F	GACCAAGACGAGTGCCTGAT	N/A
FBLN2-R	TGCCTTGTAGCAGTGGAAGG	N/A
18S-F	TCGGTCTTATTTTGCTGGTTT	N/A
18S-R	ATCGCTAGTTGGCATCGTTT	N/A
ACTB-F	CATGTACGTTGCTATCCAGGC	N/A
ACTB-R	CTCCTTAATGTCACGCACGAT	N/A
IL6-F	GCCGAAGACCCTTGGGTTAG	N/A
IL6-R	GCTGGCATTGGGCTGTAGA	N/A
CXCL8-F	TTTTGCCAAGGAGTGCTAAAGA	N/A
CXCL8-R	AACCCTCTGCACCCAGTTTTC	N/A
IL1β-F	AGCTACGAATCTCCGACCAC	N/A
IL1β-R	CGTTATCCCATGTGTCGAAGAA	N/A
MCP1-F	CAGCCAGATGCAATCAATGCC	N/A
MCP1-R	TGGAATCCTGAACCCACTTCT	N/A
VCAM1-F	TTTGACAGGCTGGAGATAGACT	N/A
VCAM1-R	TCAATGTGTAATTTAGCTCGGCA	N/A
ICAM1-F	ATGCCCAGACATCTGTGTCC	N/A
ICAM1-R	GGGGTCTCTATGCCCAACAA	N/A
MMP2-F	CCCACTGCGGTTTTCTCGAAT	N/A
MMP2-R	CAAAGGGGTATCCATCGCCAT	N/A
MMP9-F	AGACCTGGGCAGATTCCAAAC	N/A
MMP9-R	CGGCAAGTCTTCCGAGTAGT	N/A
GAPDH-F	TCGGAGTCAACGGATTTGGT	N/A
GAPDH-R	TTGCCATGGGTGGAATCATA	N/A
Software and algorithms		
ImageJ (version 1.48)	Schneider et al.[112]	https://imagej.nih.gov/ij/
GraphPad Prism (version 9.0.0)	GraphPad Software Inc.	https://www.graphpad.com/
NeuroCombat (version 1.0.14)	Fortin et al.[113]	https://github.com/Jfortin1/neuroCombat_Rpackage
mice R package (version 3.17.0)	Stef van Buuren	https://github.com/amices/mice
Cell Ranger (version 6.0.2)	10x Genomics	https://support.10xgenomics.com/

(*Continued on next page*)

Please cite this article in press as: Li et al., Multimodal clocks of human aging, Cell (2026), https://doi.org/10.1016/j.cell.2026.04.025

Continued

REAGENT or RESOURCE	SOURCE	IDENTIFIER
Scanpy (version 1.9.2)	Wolf et al.[114]	https://scanpy.readthedocs.io/en/stable/
Scrublet	Wolock et al.[115]	https://github.com/swolock/scrublet
Pytorch (version 1.1.0)	Paszke[116]	https://pytorch.org/
ENet	Paszke et al.[45]	https://github.com/davidtvs/PyTorch-ENet
HISAT2 (version 2.0.4)	Kim et al.[117]	https://github.com/DaehwanKimLab/hisat2
MXNet-CU101 framework (version 1.5.0)	Chen et al.[118]	https://pypi.org/project/mxnet-cu101/
MobileNet	Howard et al.[119]	https://pytorch.ac.cn/hub/pytorch_vision_mobilenet_v2/
OpenCV	Open Source Vision Foundation	https://opencv.org/
dcm2niix (version 1.0.20220720)	Li et al.[120]	https://github.com/rordenlab/dcm2niix
fMRIPrep (version 23.1.0)	Esteban et al.[121]	https://fmriprep.org/en/stable/
FSL (version 6.0.7)	Jenkinson et al.[122]	https://github.com/fithisux/FSL
DeepBrainNet	Bashyam et al.[123]	https://github.com/vishnubashyam/DeepBrainNet
CASIA-Gaitlife	This study	http://82.156.141.224/#/software
Retina-VesselNet	Yao et al.[124]	https://github.com/DeepTrial/Retina-VesselNet
EyeQ	Fu et al.[125]	https://github.com/HzFu/EyeQ
Fundus Age Assessment Model	Miyake et al.[126]	http://www.joir.jp/data/joir_model_20221215.zip
glmnet R package (version 4.1.8)	Simon et al.[127]	https://github.com/cran/glmnet
SeSAMe (version 1.26.0)	Zhou et al.[128]	https://github.com/zwdzwd/sesame
TrimGalore (version 0.6.7)	Felix Krueger	https://github.com/FelixKrueger/TrimGalore
FASTQC (version 0.11.9)	Simon Andrews	https://github.com/s-andrews/FastQC
featureCounts (version 2.0.1)	Liao et al.[129]	https://github.com/ShiLab-Bioinformatics/subread
DESeq2 (version 1.46.0	Love et al.[130]	https://bioconductor.org/packages/release/bioc/html/DESeq2.html
MSFragger (version 3.4)	Kong et al.[131]	https://github.com/Nesvilab/MSFragger
DIA-NN (version 1.8)	Demichev et al.[132]	https://github.com/vdemichev/DiaNN
DEP2 (version 0.3.7.3)	Feng et al.[133]	https://github.com/mildpiggy/DEP2
KneadData (version 0.12.0)	Beghini et al.[134]	https://github.com/biobakery/kneaddata
Bowtie2 (version 2.4.1)	Langmead and Salzberg[135]	https://github.com/BenLangmead/bowtie2
MetaPhlAn (version 4.1.1)	Blanco-Míguez et al.[136]	https://github.com/biobakery/MetaPhlAn
HUMAnN3 (version 3.9)	Beghini et al.[134]	https://github.com/biobakery/humann
randomForest (version 4.7.1.2)	Breiman[137]	https://cran.r-project.org/web/packages/randomForest/index.html
Hmisc (version 5.2.2)	Frank Harrell	https://github.com/haxscramper/hmisc
CIBERSORTx	Newman et al.[138]	https://github.com/ysuzukilab/Cibersortx
Metascape	Zhou et al.[139]	http://metascape.org/
MetaboAnalyst (version 5.0)	Pang et al.[140]	https://www.metaboanalyst.ca/
mgcv (version 1.8.42)	Simon Wood	https://github.com/cran/mgcv
DEswan (version 0.0.0.9001)	Lehallier et al.[141]	https://github.com/lehallib/DEswan
TwoSampleMR (version 0.6.9)	Hemani et al.[142]	https://lehallib.github.io/DEswan
Other		
384-well plates	Easybio	Cat# BE6717
LSM 900 confocal microscope	ZEISS	https://www.zeiss.com/microscopy/us/products/light-microscopes/confocal-microscopes/lsm-900-for-materials.html

(*Continued on next page*)

Continued

REAGENT or RESOURCE	SOURCE	IDENTIFIER
Dragonfly Confocal Microscope System 505	Andor	https://andor.oxinst.com/products/dragonfly-confocal-microscope-system
Axio Observer 3	ZEISS	https://www.zeiss.com/microscopy/en/products/light-microscopes/widefield-microscopes/axio-observer-for-life-science-research.html
Incucyte S3	Sartorius	https://www.sartorius.com/en/products/live-cell-imaging-analysis/live-cell-analysis-instruments/s3-live-cell-analysis-instrument
CFX384 Touch Real-Time PCR Detection System	BioRad	https://www.bio-rad.com/zh-cn/product/cfx384-touch-real-time-pcr-detection-system?ID=LJB22YE8Z
Microplate Absorbance Reader (BioTek 800 TS)	BioTeck	https://www.agilent.com.cn/en/product/microplate-instrumentation/microplate-readers/absorbance-microplate-readers/biotek-800-ts-absorbance-reader-1623177
Aperio Versa 200 scanner	Leical	https://www.leicabiosystems.com/zh-cn/digital-pathology/scan/aperio-fl/

EXPERIMENTAL MODEL AND STUDY PARTICIPANT DETAILS

Ethical statement

All human experimental procedures were approved by the Research and Ethical Committees of the following institutions: Quzhou People's Hospital (LSYD-2020-12-001), Ningbo Hangzhou Bay Hospital (KY2019-101-CR-04), Xuanwu Hospital Capital Medical University (LYS-2024-162-001), The First Affiliated Hospital of Nanchang University (IIT-2024-394), Beijing Institute of Genomics (China National Center for Bioinformation) of the Chinese Academy of Sciences (2023H001, 2024H022, 2024H023, 2024H032), and Institute of Zoology of Chinese Academy of Sciences (DYLZ-2024-024, DYLZ-2024-025, DYLZ-2024-027). Human liver samples were obtained from West China Hospital, Sichuan University, with approval from the Ethics Committee of West China Hospital, Sichuan University (NO. 2023-801).[78] Mouse experiments were approved by the Research and Ethical Committees of Institute of Zoology of Chinese Academy of Sciences (IOZ-IACUC-2025-316).

Human participants

Participants for the aging study cohort were recruited from four cities in China, including Beijing, Ningbo, Quzhou, and Nanchang. Volunteers, with an average age of 45 years and a gender distribution of 45% male, were selected based on stringent screening criteria and underwent comprehensive clinical examinations. To systematically establish an aging assessment framework, additional potential aging-related indicators were collected, including functional capacity, facial and gait assessment, and extensive biological sample evaluations (see method details). Ethical compliance was ensured through voluntary participation, with all volunteers required to sign informed consent forms. Detailed information for individuals whose biological samples were used for experimental validation is listed in Table S6.

EXPERIMENTAL MOUSE MODELS

Wild-type male C57BL/6J mice (8 months old) used here were obtained from a Beijing-based biotechnology company. All animals were maintained in SPF-grade barrier facilities. Environmental conditions were tightly controlled: temperature ranged from 20 to 25 °C, relative humidity ranged from 30% to 70%, and a 12-hour light-dark cycle was enforced. Animals were randomly assigned to either the control cohort or the experimental cohort for follow-up assessments.

METHOD DETAILS

Establishment of the standard cohort for the aging study

The recruitment of volunteers for the aging study cohort was conducted through a rigorous process. Initially, basic information from potential volunteers was obtained via an online pre-screening questionnaire to ensure that the population met the study criteria. Eligible volunteers for the aging study cohort were required to meet the following criteria: (1) healthy adults aged 18 years or older;

(2) no serious addictive behaviors, such as alcohol abuse, heavy smoking, or drug use; (3) no serious medical conditions, including cancer, severe cardiovascular diseases, autoimmune disorders, liver/kidney failure, diabetes, or infectious diseases; (4) no use of chemotherapy drugs, anti-platelet drugs, or acetylcholinesterase inhibitors for Alzheimer's disease; (5) no history of surgery or participation in other clinical studies within the last three months; (6) no long-term use of medications reported to have aging intervention effects, such as vitamin C, metformin, rapamycin, etc. To be noted, recruitment of participants aged 60 and above was conducted under the guidance of the WHO criteria for "healthy ageing".[143] In brief, older adults with preserved functional independence, intact cognitive and emotional regulation, and normal social engagement were included. The inclusion and exclusion criteria mentioned above were applied, but well-controlled hypertension and diabetes were permitted.

Subsequently, volunteers who met the inclusion criteria were enrolled and asked to sign an informed consent form. Detailed instructions were provided to each participant, including: (1) maintaining a normal daily routine while avoiding strenuous exercise for one month prior to participation to prevent acute injuries or abnormal physical conditions; (2) following a standardized diet the day before the assessment to minimize dietary variability; and (3) wearing comfortable clothing suitable for physical testing, while avoiding makeup and accessories on the day of participation.

On the day of the project, volunteers underwent systematic and comprehensive clinical examinations, functional capacity tests, and biological sample collection under the guidance of trained professionals. Clinical examinations included anthropometric measurements, blood tests (including routine, biochemistry, and hormone levels), urine routine, heart and lung function, maximal oxygen uptake (VO_{2max}), bone density, hearing tests, and ultrasound. Additionally, comprehensive behavioral capacity assessments were conducted to evaluate aging-related behavioral characteristics, including the Purdue Pegboard test, the single-leg balance test, the grip strength test, the 30-second chair stand test, and the gait analysis. Furthermore, considering the skin and facial changes associated with aging, facial images were captured under standardized conditions, without makeup or adornments (see Table S1).

Collection and storage of biological samples

All biological samples from participating research centers in this study were collected and stored in accordance with standardized protocols.[46] Specifically, blood and stool samples were collected from eligible volunteers following a standardized overnight fasting protocol. These samples were immediately refrigerated and transported to the laboratory for further processing and storage. Stool samples were divided into clearly labeled cryogenic vials for preservation. For plasma samples, blood was collected into EDTA-coated anticoagulant tubes. The anticoagulated blood samples were centrifuged at 400 $\times$ *g* for 15 minutes at 4°C to separate plasma from the supernatant. All aliquoted plasma, whole blood, and stool samples were stored long-term at -80°C and were protected from freeze-thaw cycles. Peripheral blood mononuclear cells (PBMCs) were isolated from peripheral blood collected into EDTA-coated tubes. The blood was diluted with an equal volume of PBS and separated using Ficoll density gradient centrifugation. The PBMCs obtained from each volunteer were divided into three portions: one for cryopreservation in cell freezing medium (stored in liquid nitrogen), one preserved in TRIzol reagent (stored at -80°C), and one as cell pellets (stored at -80°C). Hematological, biochemical, and hormonal parameters were measured from blood samples. Fecal samples were collected from participants on-site and immediately placed on ice packs before transport to the laboratory for storage at -80°C. Subsequently, the samples were transported to BGI Genomics in Shenzhen, China, for metagenomic analysis.

Liver tissues encompassing an age range of 14-68 years were obtained posthumously through the West China Hospital of Sichuan University.[78] Written informed consent for research use was secured from donors' immediate family members. All experimental protocols were conducted in strict accordance with the guidelines of the Research and Ethical Committee of West China Hospital of Sichuan University.

DNA methylation microarray

Genomic DNA was extracted from whole blood samples using the TIANamp Genomic DNA Kit (Tiangen, China; Cat. No. DP304-03). DNA quality was assessed by measuring the OD260/OD280 ratio (1.8-2.0) using a spectrophotometer and verifying integrity via agarose gel electrophoresis. Genomic DNA (gDNA) samples were bisulfite-converted using the EZ DNA Methylation™ Kit (Zymo Research, USA) according to the manufacturer's protocol. Subsequently, bisulfite-converted DNA was hybridized to the Infinium MethylationEPIC v2.0 BeadChip array (Illumina, USA), with cases and controls randomly distributed across arrays to minimize batch effects. The BeadChip arrays were processed using single-base extension, fluorescent staining, and, finally, scanned on an Illumina iScan system according to standard protocols.

RNA isolation and bulk RNA-sequencing

RNA sequencing library construction and sequencing were conducted as previously described.[78] Total RNA was isolated from PBMC samples using TRIzol reagent. Then, Oligo (dT) magnetic beads were used to enrich mRNA from total RNA. After fragmentation, the first - strand cDNA was synthesized using random hexamer primers. Then, the second - strand cDNA was synthesized using dUTP instead of dTTP. Following end-repair, A - tailing, adapter ligation, fragment selection, USER enzyme digestion, amplification, and purification, the strand-specific library was ready. Post-quality assessment, libraries meeting the acceptance criteria were pooled according to effective concentrations and specified data volume requirements. The library was then phosphorylated at the 5' end and circularized. Rolling circle amplification was performed on the circularized library, and finally, DNA nanoballs (DNB) were formed and loaded onto the flow cell.[111] After that, high-throughput sequencing was conducted on the MGI DNBSEQ-T7 platform with PE150.

Please cite this article in press as: Li et al., Multimodal clocks of human aging, Cell (2026), https://doi.org/10.1016/j.cell.2026.04.025

Proteomics analysis

For protein extraction, the 14 most abundant proteins were removed using the Pierce Top 14 Abundant Protein Depletion Spin Columns Kit (ThermoFisher Scientific). Protein concentration was measured using the BCA kit according to the manufacturer's instructions. For digestion, the protein solution was treated with 5 mM dithiothreitol at 56°C for 30 minutes to reduce disulfide bonds, followed by alkylation with 11 mM iodoacetamide for 15 minutes at room temperature in the dark. Urea was replaced three times with 8 M urea, followed by displacement buffer. Proteins were enzymatically digested overnight with trypsin at a 1:50 (protease: protein, m/m) ratio. Peptides were collected by centrifugation at 12,000 × *g* for 10 min. The sample was fractionated by high-pH reverse-phase high-performance liquid chromatography (HPLC) using an Agilent 300 Extend C18 column (5 μm particles, 4.6 mm ID, 250 mm length). Peptides were further separated on an EASY-nLC 1200 UPLC system (ThermoFisher Scientific) with mobile phase A (0.1% formic acid, 2% acetonitrile in water) and mobile phase B (0.1% formic acid, 90% acetonitrile in water). The fractionated peptides were introduced into an NSI ion source for ionization and analyzed using an Orbitrap Exploris 480 mass spectrometer (ThermoFisher Scientific). Mass spectrometry parameters were set as follows: ion source voltage at 2.3 kV and FAIMS compensation voltage (CV) between -45 V and -70 V. Both precursor ions and their fragments were detected and analyzed with high-resolution Orbitrap. The primary mass spectrometry scan range was set to 390-810 m/z with a resolution of 30,000. Secondary mass spectrometry scans started at 200 m/z, also at a resolution of 30,000. A data-independent acquisition (DIA) mode was applied, with fragmentation energies of 25, 30, and 35. To enhance mass spectrometry efficiency, Automatic Gain Control (AGC) was set to 3×10^6, and the maximum injection time was set to Auto. Proteomics analysis services were provided by PTM Biolabs, Inc.

Untargeted metabolomic analysis

Calibra Lab at DIAN Diagnostics (Hangzhou, Zhejiang, China) conducted the non-targeted metabolomic analysis using its proprietary CalOmics metabolomics platform. The samples were homogenized and extracted with methanol in a 1:4 ratio, then shaken for 3 minutes and centrifuged at 4000 × *g* for 10 minutes at 20°C. Four 100 μL aliquots of the supernatant were transferred to 4 separate sample plates, dried under nitrogen gas blow, and re-dissolved in reconstitution solutions for injection into UPLC-MS/MS systems. The instruments used were an ACQUITY 2D UPLC system (Waters, Milford, MA, USA) coupled with a Q Exactive hybrid Quadrupole-Orbitrap mass spectrometer (Thermo Fisher Scientific, San Jose, USA) operated at a mass resolution of 35000 and a scan range of 70-1000 m/z. The four UPLC-MS/MS methods employed different configurations: the first method was operated in positive ESI mode with a C18 reverse-phase column (UPLC BEH C18, 2.1×100 mm, 1.7 μm; Waters) and a mobile phase of water (A) and methanol (B) containing 0.05% PFPA and 0.1% FA; the second method was operated in negative ESI mode with the same C18 column and a mobile phase of water (A) and methanol (B) containing 6.5 mM ammonium bicarbonate at pH 8; the third method was operated in positive ESI mode with a C18 column and a mobile phase of water (A) and a mixture of methanol/acetonitrile/water (B) containing 0.05% PFPA and 0.01% FA; and the fourth method was operated in negative ESI mode with a HILIC column (UPLC BEH Amide, 2.1×150 mm, 1.7 μm; Waters) and a mobile phase of water (A) and acetonitrile (B) with 10 mM ammonium formate.

Metagenome DNA extraction and sequencing

Metagenomic DNA (metaDNA) was extracted as described previously.[144] Briefly, 200 mg of fecal sample was aliquoted into a 2 mL homogenization tube. After centrifugation at 14,000 × *g* for 5 minutes at 4°C, the supernatant was discarded. Then, 300 μL of glass beads and 600 μL of kit-provided lysis buffer were added, followed by homogenization in a tissue grinder (QIAGEN) at 30 r/s for 5 min. The sample was briefly centrifuged, incubated at 70°C for 20 minutes in a dry incubator, and cooled to room temperature in a fume hood. Next, 600 μL of Buffer PCI was added, and the mixture was inverted manually for 2-3 minutes until emulsified. After centrifugation (14,000 × *g*, 5 min, 4°C), the supernatant was transferred to a deep-well plate for magnetic bead-based purification.

An automated pipetting workstation (MGISP-960) dispensed wash and elution buffers (AE) into the plate, which was then loaded into an MGINE-384 nucleic acid extraction system for automated processing. Purified DNA was transferred to labeled PCR plates using the MGISP-960 and stored at -20°C.

For library preparation, 500 ng of metaDNA was sheared (Covaris E220; Covaris, UK) to 300–700 bp fragments. These were end-repaired, A-tailed, and ligated to indexed adapters (T4 DNA Ligase). After PCR amplification, fragments were hybridized with exon probes, circularized, and enzymatically digested. Quality-controlled libraries were converted to DNA nanoballs (DNBs) via rolling circle amplification (RCA), loaded onto a Pattern Array chip, and sequenced (DNBSEQ platform).

Single-cell RNA sequencing (scRNA-seq) for PBMCs

scRNA-seq for PBMCs were performed as previously described.[46] In brief, PBMCs were thawed and resuspended in medium containing 10% fetal bovine serum (FBS). PI-negative cells were sorted using FACS (BD Influx) and counted with a dual-fluorescence cell counter (Luna-FL™, Logos Biosystems). The cells were then processed for single-cell capture using the 10x Genomics Single-Cell 3' system. Approximately 10,000 cells per sample were captured following the standardized 10x Genomics protocol and subjected to library preparation. Sequencing was performed using the DNBSEQ-T7 Sequencing System with a PE150 configuration.

Quantified reverse-transcription PCR (RT-qPCR)

RT-qPCR was performed as previously described.[145] Briefly, total RNA was extracted from PBMCs with TRIzol reagent (Ambion) followed by cDNA synthesis using HiScript III RT SuperMix for qPCR (plus gDNA wiper) (Vazyme). qPCR was performed by CFX384 Real-Time System (BioRad). All data were normalized relative to the internal control and quantified using the $2^{-\Delta Cq}$ method. The primer sequences are provided in the key resources table.

Recombinant protein treatment in mice

To model the chronic elevation of endogenous F13B observed in tissues and fluids in aged humans, while accounting for the rapid clearance of exogenously delivered proteins *in vivo*, we used a dosage roughly three times the reported physiological level. Injections were given every five days to better replicate an aging-related state. Briefly, 8-month-old male C57BL/6J mice were randomly divided into two experimental groups. These animals received either PBS as the vehicle control or human F13B at a dose of 1 mg/kg body weight via intravenous tail-vein injection every five days for a total of nine doses.. After the final injection, tissues were harvested for downstream analyses.

Flow cytometric analyses

Flow cytometric analyses were performed according to established protocols.[146,147] In brief, PBMCs were thawed and resuspended in 10% FBS. The cell suspension was stained with Fixable Viability Dye eFluor™ 506 (Thermo Fisher) for 30 minutes at 4°C in the dark. After washing with cell staining buffer (BioLegend), the cells were incubated with fluorophore-conjugated primary antibodies for 30 minutes at room temperature, protected from light. Then, cells were fixed using fixation buffer (BioLegend) for 15 minutes at room temperature, protected from light. Finally, the cells were washed with cell staining buffer, analyzed on the LSRFortessa (BD Biosciences), and the data were processed and analyzed using FlowJo software. The antibodies and reagents used in this study were as follows: CD3-PE/Cyanine7 (BioLegend), CD4-PE/Dazzle™ 594 (BioLegend), CD8-APC (BioLegend), CD45RA-Brilliant Violet 605™ (BioLegend), CCR7-PE (BioLegend), CD27-APC/Cyanine7 (BioLegend), CD28-Brilliant Violet 421™ (BioLegend), CD57-FITC (Thermo Fisher).

Immunofluorescence (IF) and immunohistochemistry (IHC) stainingr

For paraffin-embedded tissues, sections were deparaffinized, rehydrated, and subjected to antigen retrieval as reported previously.[23] For cell samples, samples were fixed with paraformaldehyde (PFA) for 10 min and used directly in subsequent experiments. After permeabilization with 0.4% Triton X-100 (Solarbio) for 10-30 minutes, nonspecific binding was blocked with 5% donkey serum (Jackson ImmunoResearch) in PBS for 1 hour at room temperature. The samples were incubated with primary antibodies overnight at 4°C, then washed with PBS and incubated with fluorophore-conjugated secondary antibodies for 1 hour at room temperature. Nuclei were stained with Hoechst 33342 (Thermo Fisher Scientific). Imaging was performed using a ZEISS LSM 900 confocal microscope, and fluorescence intensity was quantified using ImageJ.

For PBMCs, the cells were thawed and resuspended in 10% FBS. Then, a cytospin centrifuge was used to immobilize cells onto a glass microscope slide. After fixation with 4% PFA at room temperature for 20 minutes, the slides were incubated with 0.4% Triton X-100 for 20 minutes and blocked with 5% donkey serum in PBS for 1 hour at room temperature. Subsequently, the slides were incubated with primary antibodies overnight at 4°C. The slides were then incubated with fluorophore-conjugated secondary antibodies and Hoechst 33342 for nuclear staining for 1 hour at room temperature. Finally, high-resolution images were captured using the Andor Dragonfly 505.

For immunohistochemical analysis, paraffin-embedded tissue arrays were deparaffinized and rehydrated, followed by antigen retrieval and permeabilization as previously described. Endogenous peroxidase in human tissues was eliminated using 3% H_2O_2 dissolved in methanol. Following a 1-hour blocking step with 10% donkey serum, sections were incubated with primary antibodies at the optimal concentration overnight at 4°C, followed by incubation with matching HRP-conjugated secondary antibodies for 1 hour at room temperature. Subsequent steps included DAB-HRP chromogenic reaction and hematoxylin counterstaining. Imaging was conducted with the PerkinElmer Vectra Polaris automated quantitative pathology platform.

Detailed antibody information is provided in the key resources table.

Western blotting

Western blotting was performed as previously described.[30] Cultured cells were lysed in 1× SDS lysis buffer, and the lysates were boiled at 95°C for 10 min. Total protein concentration was determined using a BCA assay kit (Dingguo Changsheng Biotech, Cat. No. BCA02). After protein concentration adjustment, approximately 40 μg of protein per lane was separated by SDS-PAGE and transferred to methanol-pre-treated PVDF membranes. The membranes were blocked with 5% non-fat milk, then incubated with primary antibodies overnight at 4°C, followed by incubation with corresponding secondary antibodies at room temperature for 1 h. Image acquisition was performed with a ChemiDoc XRS+ Gel Imaging System (Bio-Rad), and quantitative analysis was performed with ImageJ.

Hematoxylin-eosin (HE) staining

For HE staining, liver sections (4 μm) were deparaffinized, rehydrated, and stained with Mayer's hematoxylin for 5 min, followed by rinsing in water for bluing. Sections were then counterstained with eosin for 1 min, dehydrated through graded ethanol, cleared in xylene, and mounted with neutral balsam. Whole-slide images were acquired on a Leica Aperio Versa 200 scanner, and the area of inflammatory lesions was quantified using ImageJ software.

Cell culture

Human Aortic Endothelial Cells (HAECs) (Lonza, CC-2535) were purchased from Lonza and cultured in an incubator at 37 °C with 5% CO_2. The HAECs were seeded onto culture dishes pre-coated with collagen (Advanced BioMatrix), and the Endothelial Cell Medium (ScienCell) was replaced every two days. Upon reaching full confluence, the cells were harvested using Accumax (Millipore), counted, and passaged. At the sixth passage (P6), the cells were cultured in medium supplemented with coagulation factors, including F9 (MCE, 650 ng/ml), F10 (MCE, 40 μg/ml), F13B (MCE, 20 μg/ml), and TFPI (MCE, 30 ng/ml) for one week prior to further experimental analysis.

HAEC tube-formation assay

The HAEC tube-formation assay was performed according to previously published protocols.[30] Briefly, Matrigel was thawed and diluted 1:1 with Endothelial Cell Medium. 200 μL of volume per well was added to a 24-well plate and incubated at 37°C for 1 hour to allow Matrigel polymerization. After trypsinization and counting, HAECs were seeded at a density of 6×10^4 cells per well onto the Matrigel-coated 24-well plate and cultured at 37 °C for 4 hours. The cells were stained with Calcium-AM (Invitrogen) to visualize the vascular network. Fluorescence images were captured with a ZEISS fluorescence microscope (ZEISS, Axio Observer 3), and the vascular network was quantitatively analyzed in ImageJ.

Cell-adhesion assay

Adhesion assays were conducted on endothelial cells treated with coagulation factors.[148] The cells were seeded at a density of 5×10^4 cells per well in 24-well plates pre-coated with collagen. When confluence reached 90%, the endothelial cells were stained with Hoechst 33342, and THP-1 cells labeled with Calcium-AM (Invitrogen) were added for co-culture for 30 minutes. Unattached cells were removed by rinsing with PBS. Fluorescence images were captured with a microscope (ZEISS, Axio Observer 3), and the data were analyzed using ImageJ.

SA-β-Gal staining

The SA-β-Gal staining experiment was performed as previously described.[78] Cells were washed twice with PBS, fixed with a solution containing 2% formaldehyde and 0.2% glutaraldehyde at room temperature for 5 minutes, and then stained overnight at 37 °C with a 1 mg/ml X-gal working solution. Nuclei were counterstained with Hoechst 33342. Imaging was performed with a Nikon Y-TV55 microscope, and the percentage of SA-β-Gal-positive cells was quantified in ImageJ.

Enzyme-linked immunosorbent assay (ELISA)

The ELISA experiment was performed following the manufacturer's instructions. Samples (plasma or cell culture supernatant) and standard proteins were diluted proportionally and incubated with antigens or antibodies pre-coated on plates. After thorough washing of the plates, detection antibodies were applied, followed by avidin-HRP solution to bind with the antibodies. Color development was achieved by adding tetramethylbenzidine (TMB) substrate solution. The reaction was terminated with the stop solution once the positive wells turned blue. Absorbance was measured at 570 nm using a microplate absorbance reader (BioTek 800 TS). The concentration of target proteins was determined from a standard curve, and the results were visualized in GraphPad Prism.

Quality control and preprocessing of physical examination data

Physical examination data were collected from four centers. For each center, indicators with less than 20% missing values and individuals with less than 20% missing data were retained. To correct for unwanted technical variation caused by differences in measurement instruments across centers, the harmonization of multi-center examination data was performed using the R package neuroCombat (v1.0.14).[113] Missing data were imputed using the R package mice (v3.17.0) with the classification and regression trees (CART) method (https://github.com/amices/mice). The physiological indicators were manually grouped into organ-associated functional modules (e.g., circulatory transport, endocrine regulation, immune defense, neural and cognitive modulation) using prior evidence and expert knowledge.[149,150] The complete mapping of each indicator to its corresponding functional subclass is listed in Table S1.

Anthropometric and body composition measurements

For anthropometric measurements, barefoot height, body weight, waist circumference, and hip circumference were measured on the day of examination following standardized protocols. In addition, spinal and hip bone mineral density (BMD) assessments were performed on a voluntary basis. For body composition analysis, parameters including trunk fat mass, body water proportion, and impedance were recorded using a bioelectrical impedance analysis (BIA) device. Briefly, participants were asked to stand barefoot on the

BIA platform while holding the device handles with both hands. Detailed indices for anthropometry and body composition are summarized in Table S1.

Facial image acquisition

Each participant was required to provide five facial photographs from different angles: frontal, left profile, right profile, 45 degrees left-front, and 45 degrees right-front. All images were captured under uniform lighting and background conditions, with participants maintaining a neutral expression to minimize external interference in facial feature recognition.

Facial wrinkle detection

To detect and localize facial wrinkles, we employed the ENet model,[45] trained on the FFHQ-Wrinkle dataset, which comprises 1,000 manually annotated images depicting facial wrinkle features.[151] We partitioned the dataset into training and testing subsets at a 4:1 ratio. Using cross-entropy as the loss function, we trained the model until convergence. Subsequently, the trained ENet model was applied to detect wrinkles in volunteer facial images. The model generates segmentation masks that delineate wrinkle regions, thereby effectively achieving wrinkle detection and localization. Subsequently, we computed the wrinkle ratio as the ratio of wrinkle area to facial area.

Face-Clock construction

As previously reported, the facial age prediction model was trained on three Asian facial image datasets: AFAD, MegaAge, and AgeDB using the MXNet-CU101 framework (v1.5.0) and customizing MobileNet via the insightFace module.[152] Input images underwent standardized OpenCV preprocessing, including alignment and normalization (https://github.com/opencv/opencv). The model then generated age estimates for volunteers.

Neural and cognitive regulation

For the Purdue pegboard test, participants were instructed to perform four subtests: assembly tasks with the left or right hand individually, a bilateral assembly task using both hands simultaneously (each for 30 seconds), and a composite assembly task (for 60 seconds). Participants were allowed to practice each task 2-3 times prior to formal testing. The final score was calculated as the sum of scores from all four subtests.

For the Trail Making Test, participants were instructed to connect all the dots on the paper, starting from any point, without overlapping or crossing lines. The total time to completion was recorded.

Magnetic resonance imaging analyses

Imaging data were acquired using a SIGNA Premier 3.0T. For each volunteer, high-resolution T1-weighted whole-brain and axial brain anatomical images were captured. The whole-brain T1-weighted images were acquired via a magnetization-prepared rapid gradient echo (MPRAGE) sequence with the following parameters: echo time (TE) = 2.7 ms, repetition time (TR) = 6 ms, flip angle = 8°. The axial T1-weighted images were obtained with the following parameters: TR = 120 ms, flip angle = 70°.

BOLD data acquisition was also performed on the SIGNA Premier 3.0T system. Resting-state functional magnetic resonance imaging (fMRI) was conducted for each participant, employing an axial acquisition orientation and an echo-planar imaging (EPI) sequence. The specific imaging parameters were as follows: flip angle = 83°, repetition time (TR) = 2000 ms, echo time (TE) = 33.1 ms. The imaging volume was positioned axially at the superior aspect of the lateral ventricles.

All MRI data were converted into Brain Imaging Data Structure (BIDS) using dcm2niix (version v1.0.20220720) (https://github.com/rordenlab/dcm2niix). Results reported in this manuscript were obtained from preprocessing using fMRIPrep (version 23.1.0).[121] Global signals from CSF, WM, and VM masks were extracted using FSL (version 6.0.7).[122]

Functional connectivity computation

As previously reported,[153] fMRIprep output data were loaded using Nilearn (version 0.10.3)[154] and BOLD time series were extracted using the Harvard-Oxford atlas.[155] Functional connectivity networks were subsequently calculated, followed by the derivation of Spearman correlation coefficients between regional connections and age.

MRI-Clock construction

The DeepBrainNet model was used for brain age prediction. T_1-weighted MRI data were processed in a manner similar to prior studies.[123] Initially, skull stripping was performed to eliminate non-brain tissues. Subsequently, FMRIB's Linear Image Registration Tool (FLIRT), leveraging an affine transformation, was employed to register the processed images to a shared atlas space.[156,157] Built on this foundation, the DeepBrainNet model was fine-tuned using transfer learning to adapt to the cohort data. This step aimed to enhance the model's adaptation to the unique brain structural and age-related traits inherent in the cohort under investigation.

Motor coordination assessment

For the grip strength test, participants were instructed to hold a dynamometer (Jamar Plus+) with their forearm positioned at a 90-degree angle relative to the upper arm. The maximum grip strength of both the left and right hands was recorded.

For the sit-to-stand test, participants were asked to repeatedly sit down and stand up from a chair for 30 seconds, with both arms crossed in front of the chest. The total number of complete sit-to-stand cycles was recorded.

For the single-leg stance test, participants were instructed to extend both arms horizontally and lift one leg backward, bending the knee to 90 degrees. The maximum duration of single-leg balance for both the left and right legs was recorded.

For the maximal oxygen consumption (VO_2max) test, participants performed an incremental cycling test to exhaustion on a stationary bike (Ergoline Ergoselect 100P). During the exercise, physiological parameters including VO_2max, vital capacity, and heart rate were continuously recorded. All measurements are summarized in Table S1.

The motor coordination ability aging clock (motoClock) developed in this study integrates the grip strength test, the sit-to-stand test, the single-leg stance test, and the pegboard test. Detailed modeling procedures for this aging clock follow the protocol described in the "Single-layered multi-omics aging clock construction" section.

Gait feature analysis

To investigate the impact of aging on individual motor capabilities, we established a systematic data-acquisition protocol for motor performance based on prior research.[158–160] A 4K XTU motion camera was employed for data acquisition, configured at 30 FPS to ensure temporal continuity and at 1920 × 1080 to maintain sufficient image clarity.

To quantitatively evaluate the impact of aging on the body, this study introduces 45 feature metrics across multiple dimensions, including temporal, spatial, and dynamic domains, as shown in Table S1 and referenced in the relevant literature. To automate the extraction of these features, we utilized our self-developed gait analysis software, CASIA-Gaitlife (http://82.156.141.224/#/software). Initially, we combined RGB image features with skeletal constraint information guided by binary masks to extract 17 key human joint points using a global spatiotemporal encoding network,[22,161,162] achieving high-precision modeling of human motion states, as illustrated in Figure 2K. Building on this, CASIA-Gaitlife employs a global spatiotemporal modeling mechanism to fuse the coordinate sequences of joint points, integrating geometric and interpolation operations along with dynamic pattern extraction of joint trajectories, thereby accurately calculating gait cycle and other characteristic parameters.

Cardiovascular aging clock construction

The cardiovascular aging clock integrates multimodal data from resting 12-lead electrocardiography (ECG), transthoracic echocardiography, carotid ultrasound, and brachial blood pressure measurements, including systolic blood pressure (SBP) and diastolic blood pressure (DBP). From the ECG, we extracted heart rate, P-wave duration, PR interval, QRS duration, QT and QTc intervals, T-wave duration, QT dispersion, electrical axes (P, QRS, T), and left ventricular voltage indices (RV5, SV1, RV5/SV1, RV5+SV1). Transthoracic echocardiography provided a comprehensive assessment of cardiac structure and function, including left and right ventricular dimensions, wall thickness and motion amplitudes, atrial and aortic root diameters, valvular excursion and peak velocities across major valves, as well as key functional parameters such as ejection fraction (EF), end-diastolic volume (EDV), stroke volume (SV), and cardiac output (CO). Diastolic function was further characterized by mitral and tricuspid inflow E/A ratios. Carotid ultrasound was performed with participants in the supine position to enable pulsed-wave Doppler recording of blood flow velocities in the bilateral common carotid arteries (CCA), internal carotid arteries (ICA), carotid bulbs (BULB), and subclavian arteries (SubA). Additionally, intima-media thickness (IMT) was measured on the far wall of the distal common carotid artery, approximately 1 cm proximal to the bifurcation, yielding separate values for the left (L-CIMT) and right (R-CIMT) sides. In total, 53 cardiovascular-related clinical metrics were used to construct the cardiovascular aging clock. An Elastic Net regression model was used to construct a cardiovascular aging clock. The dataset was split into two parts: 50% for model training and 50% for validation.

Retinal color fundus image collection

In this study, retinal fundus color images were captured using a Canon digital fundus camera CR-2 Plus AF. Without the use of mydriatics, digital fundus images were obtained under natural pupil dilation at a 45-degree angle. During the acquisition process, the fundus camera was first adjusted to align with the volunteer's eye, and the pupil position was aligned with the positioning circle on the monitor. Subsequently, the joystick was adjusted for focusing, and the image was captured after successful focusing. The captured image was then subjected to a preliminary inspection. If the image was not in clear focus or had exposure errors, it was retaken until a clear, high-quality fundus image was obtained. The final images were saved as JPG files.

Retinal blood vessel segmentation

In this study, we developed a computational approach to quantify retinal vessel density and detect vascular branch points from retinal fundus images. The segmentation of retinal vessels was initially performed using the Retina-VesselNet model, which is a variant of the U-Net architecture specifically tailored for retinal vessel segmentation.[124] This model effectively identifies and delineates vascular structures from the background, resulting in a binary mask. Based on the binary mask obtained from segmentation, two key features were extracted: vessel density and the number of branch points. Vessel density was defined as the proportion of vessel pixels relative to the total pixels within the segmentation mask, yielding a quantitative metric of retinal vascular coverage. For branch point detection, a morphological approach was employed. Specifically, the segmentation mask was first skeletonized using the thinning algorithm from the OpenCV library, which reduces vascular structures to single-pixel-wide lines while preserving their topological

structure. Subsequently, branch points were identified by analyzing the connectivity of pixels in the skeletonized image. A pixel was considered a branch point if it had more than three connected neighbors within its 8-connected neighborhood.

Retina aging clock construction

The fundus age assessment model utilized in this study was previously developed by the Japanese Ophthalmological Society and the National Institute of Informatics.[126] The model leverages a Swin Transformer architecture pre-trained on ImageNet, which was subsequently trained using a dataset of 15,000 fundus images collected from healthy volunteers across various age groups. Given that the accuracy of age prediction is highly dependent on image quality, we first assessed the retinal image quality using the EyeQ method (Retinal Image Quality Assessment, RIQA).[125] Only retinal images rated "Good" or "Usable" by EyeQ were included in the analysis to predict physiological age. After quality control, the retinal images were cropped to 384×384 pixels using the Image class from the Python Imaging Library (PIL) (version 10.4.0). All images from the left eye were horizontally flipped to align with the coordinate system of the right eye images. Subsequently, the fundus age assessment model was used to estimate the volunteers' biological age.

Pulmonary function testing

Pulmonary function tests were conducted to evaluate respiratory mechanics, including lung volumes and airflow limitation. All assessments were performed using a standardized spirometry system. Prior to testing, participants were instructed to avoid bronchodilators or vigorous exercise for at least 12 hours. Each subject underwent spirometry to measure forced vital capacity (FVC), forced expiratory volume in one second (FEV_1), and the FEV_1/FVC ratio. The highest of three acceptable measurements was recorded.

Core capacity clock (CC-clock) construction

To develop the CC-clock, we utilized elastic net regression using the glmnet R package (version 4.1.8).[127] Initially, we identified age-associated characteristics using Spearman correlation analysis. . Samples were randomly split into training and test sets at a 1:1 ratio.

Within the training set, we performed 10-fold cross-validation to determine the optimal lambda (regularization parameter) for each candidate alpha (with mixed parameters ranging from 0.1 to 0.9). The final model was selected based on the alpha-lambda combination that achieved the lowest mean absolute error (MAE) on the test set. The aging clock's performance was gauged by computing the Pearson correlation coefficient (R), *P* value, and MAE between predicted and actual ages.

DNA methylome data analysis

DNA methylation data for each sample were first processed with SeSAMe (version 1.26.0)[128] using the openSesame function to mask non-uniquely mapped probes, perform channel inference and dye bias correction, calculate detection P-values and conduct background subtraction, filter low-quality loci, and impute missing values with the k-nearest neighbor (KNN) method (https://bioconductor.org/packages/impute).

Transcriptome data analysis

The steps for strand-specific RNA-seq data processing have been reported previously.[163] In detail, raw reads were first trimmed and filtered with TrimGalore (version 0.6.7) to remove adaptors and low-quality reads. FASTQC (version 0.11.9) was then used to evaluate the qualities of the remaining reads. Cleaned reads were mapped to the hg38 reference genome from the UCSC Genome Browser using HISAT2 (version 2.0.4).[117] Counting high-quality mapped reads for each annotated gene was processed using featureCounts (version 2.0.1).[129] ComBat-seq was then used to remove the potential batch effects for RNA-seq count data.[164] For downstream analyses, gene counts were normalized using variance stabilizing transformation via vst function in DESeq2 (version 1.46.0).[130]

Proteomics data analysis

For spectral library generation, DDA data were processed using MSFragger (version 3.4) and searched against the human SwissProt database.[131,165] Trypsin/P was specified as the cleavage enzyme, with up to 2 missed cleavages allowed. The mass tolerance was set to 20 ppm. Carbamidomethylation on cysteine was designated as a fixed modification, while acetylation on the protein N-terminus and methionine oxidation were considered variable modifications. The false discovery rate (FDR) was controlled at < 1%. DIA data were analyzed using DIA-NN (version 1.8) with the generated library and default settings.[132] Raw density was first divided by the median of each protein within a batch to remove the potential batch effect. Proteins detected in more than 50% of individuals were retained and then subjected to the DEP2 (version 0.3.7.3) package for normalization and missing-value imputation.[133] The obtained matrix was then divided by each sample's median to obtain normalized intensities for downstream analysis.

Metabolomics data analysis

After pre-processing raw data and data quality control inspection, ion peaks were extracted and identified by searching an in-house library generated from running reference standards from commercial sources and in-house sources. Identification of metabolites in

samples required strict matching of three criteria between experimental data and library entry: narrow window retention index (RI), accurate mass with variation less than 10 ppm, and MS/MS spectra with high forward and reverse searching scores. Peak area for each metabolite was calculated using the area under the curve.

Before statistical analysis, normalize the original peak area based on batch information to adjust for systematic fluctuations between batches. Then perform logarithmic transformation (log_{10}) on the normalized peak area to reduce the skewness of the data distribution and make it approximate a normal distribution (Gaussian distribution).

Metagenomic data analysis

KneadData (version 0.12.0) was used to process metagenomic reads (in fastq format) by trimming the reads and removing adapters (https://github.com/biobakery/kneaddata). The KneadData integrated Bowtie2 (version 2.4.1) to remove reads that aligned to the human genome (GRCh37/hg19). Taxonomic composition of metagenomes was profiled by MetaPhlAn (version 4.1.1) using the MetaPhlAn database of marker genes mpa_v23_Jan21.[136] Profiling of genes encoding microbial pathways was performed using the HUMAnN3 (version 3.9) based on UniRef90 protein database and ChocoPhlAn pan-genome database (version 201901b).[134]

Dyshomeostatic index (DHI) calculation

The DHI calculation method in this study modifies previous protocols.[166] Initially, samples are categorized into six age groups: <30, 30-40, 40-50, 50-60, 60-70, and >70 years, based on age information. To equalize sample sizes, down-sampling is applied to each group. With the <30 age group serving as the baseline reference, features were stratified into 10 ascending bins based on expression levels, excluding the top and bottom bins to minimize outlier effects. For remaining bins, mean (μ) and standard deviation (σ) are computed, along with the coefficient of variation (CV = σ/μ). From each bin, the top 1% of features with the lowest CV values were selected as stably expressed features. Finally, for samples in other age groups, the dyshomeostatic index was determined by calculating the Euclidean distance of these low-variability features relative to the 20-30 reference group, formulated as follows:

$$DHI_s = \sqrt{\sum_{i=1}^{n} \left(x_{s,i} - \mu_i\right)^2}$$

where $x_{s,i}$ denotes the expression value of the i-th low-variability feature in sample s, and μ_i represents the mean expression of the same feature in the 20-30 years group. The index i runs over n features that were selected based on their low CV within the reference group. This method quantifies the degree of systemic dysregulation in individual by calculating the coefficient of variation in feature expression and Euclidean distances across different age groups. A larger DHI indicates more severe systemic dysregulation associated with biological aging.

Aging-related differential feature identification

To identify age-associated features, we calculated the Spearman correlation coefficient between each feature and chronological age using the rcorr function from the Hmisc (version 5.2.2) package in R, which provides both the correlation coefficient (R) and the corresponding *P* value. In general, features with an absolute Spearman correlation coefficient (|R|) greater than 0.2 and an adjusted *P* value less than 0.05 were considered significantly associated with age. For the clinical parameters of the human body morphology and composition and core capacity modules, we additionally used the Wilcoxon rank-sum test to calculate the changes in aging-related differences between the elderly (over 70 years old) and the young (under 30 years old). Notably, for features from DNA methylation data, a stricter threshold of $|R| > 0.3$ was applied, while for metagenomic features, a more relaxed threshold of $|R| > 0.1$ was used, reflecting the distinct characteristics and expected effect sizes of different omics layers. These thresholds were determined based on the overall distribution of correlation coefficients and the biological relevance of each omics type (see Table S1 for details).

scRNA-seq data analysis

Raw data generated with the 10x Genomics Chromium platform were processed with Cell Ranger (version 6.0.2) and mapped to the GRCh38 reference genome. The obtained expression matrix was processed using the Scanpy package (version 1.9.3).[114] For each sample, cells with fewer than 400 detected genes or with > 20% mitochondrial transcript content were excluded. Doublets were identified and removed using the Scrublet module.[115] Gene expression matrices were normalized per cell to a total count of 10,000, followed by ln(1 + x) transformation.

Highly variable genes were selected based on dispersion and mean expression thresholds, and total UMI counts and mitochondrial percentage were regressed out. The resulting data were scaled and subjected to principal component analysis (PCA). Batch effects across samples were corrected using BBKNN based on the top 100 principal components.

Uniform Manifold Approximation and Projection (UMAP) was performed for visualization. Cell clustering was conducted using the Leiden algorithm at multiple resolutions, and marker genes for each cluster were identified using the Wilcoxon rank-sum test. Clusters were manually annotated based on the expression of canonical marker genes.

Bulk RNA-seq deconvolution for PBMC cell types

Cell type deconvolution was conducted using CIBERSORTx.[138] To construct a reference profile from scRNA-seq data, we randomly sampled 200 cells per cell type. Raw count data from these downsampled scRNA-seq datasets were then used to generate the signature matrix. Subsequently, the signature matrix and the raw bulk RNA-seq count data were input into the "Impute Cell Fractions" module of CIBERSORTx, with 500 permutations specified. The estimated cell-type fractions were further analyzed using correlation and statistical testing.

Pathway enrichment analysis

Pathway enrichment analysis of genes and proteins was performed via the Metascape web tool.[139] MetaboAnalyst (version 5.0) was used to annotate metabolites with pathway information with SMPDB as the library.[140] For the metagenomics dataset, pathway enrichment was performed based on Humann3.[134] The microbial pathways were annotated by the MetaCyc database.[167]

Single-layered multi-omics aging clock construction

To construct aging clocks across different omics layers, we applied elastic net regression with the glmnet R package (version 4.1.8) or a random forest algorithm with the randomForest R package (version 4.7.1.2). For each omics dataset, we first selected age-associated features based on Spearman correlation analysis, as described above. The modeling procedure was implemented using a customized pipeline, in which samples were randomly split into training and test sets at a 1:1 ratio.

Within the training set, we performed 10-fold cross-validation to determine the optimal lambda (regularization parameter) for each candidate alpha (mixing parameter ranging from 0.1 to 0.9). The final model was selected based on the alpha-lambda combination that yielded the lowest MAE on the test set. For the fecal metagenomics dataset, we performed 10-fold cross-validation to determine the best decision trees to select relevant features to construct and evaluate the performance of age-based predictive models. The performance of the aging clock was evaluated by calculating the correlation coefficient (R), the P value, and the MAE between the predicted and chronological ages. The entire analysis was parallelized across multiple cores to improve computational efficiency.

Multimodal clock (MM-clock) construction

To predict biological age from multimodal data, we designed a modular deep learning framework that integrated omics-specific attention mechanisms and inception-style feature abstraction. The model received a dictionary of omics-specific feature matrices, and each omics type is processed independently through a two-stage pipeline: attention weighting and a nonlinear transformation.

Model Architecture

Each omics dataset (e.g., transcriptome, proteome, phenome) was first fed into a feature weighting module, which computed an importance score for each input feature within that modality. These scores were derived from the feature vector using a small neural network, followed by sigmoid activation. The scores were then used to rescale each feature, allowing the model to emphasize biologically relevant signals. To improve stability and retain baseline information, the reweighted features were combined with the original inputs through a residual connection, and the result was normalized across the feature dimension.

Next, each omics-specific representation was passed through a multi-branch transformation block composed of three parallel fully connected sub-networks of varying depth. The first branch performs a shallow transformation (single linear layer), the second uses two layers with an intermediate activation function, and the third applies a deeper three-layer structure with multiple nonlinear activations. These branches are designed to capture patterns at different levels of complexity. The outputs of the three branches were concatenated to form a comprehensive representation of each omics modality.

Representations from all omics types were then concatenated across modalities and passed through a shared feedforward neural network with a hidden layer and a final regression layer to produce a single age prediction.

Training Procedure

Training was performed using the mean squared error (MSE) loss between predicted and actual chronological age. The model was optimized with Adam (learning rate = 1e-4, weight decay = 1e-4) and a ReduceLROnPlateau scheduler that halved the learning rate when validation loss plateaued. To avoid overfitting, we employed early stopping (patience = 10 epochs, delta = 0.001).

Repeated Modeling and Attention Extraction

To improve stability and enable feature interpretation, we repeated the training process 10 times with different random seeds. For each repeat, the trained model and loss history were saved, and predictions were generated on the test set. In addition, attention weights from each omics-specific attention module were extracted and stored for downstream analysis.

The best-performing model, defined as the one with the lowest test MAE, was selected as the final model. The attention weights from this run were used to rank features by relative importance, facilitating omics-level interpretation of aging relevance.

Feature importance analysis

To assess the contribution of each feature to the aging clock models, we performed a feature importance analysis (FIA) using a leave-one-feature-out strategy. For each omics-specific model, we first built a primary elastic net model using all selected age-associated features. Then, we iteratively excluded one feature at a time and rebuilt the model using the remaining features.

Please cite this article in press as: Li et al., Multimodal clocks of human aging, Cell (2026), https://doi.org/10.1016/j.cell.2026.04.025

The importance of each feature was quantified as the change in prediction accuracy, measured as the increase in MAE between the primary model and the corresponding leave-one-feature-out model. A higher MAE increment indicated a greater contribution of the feature to the model's predictive performance. See Table S2 for details.

Generalized additive model (GAM) fitting and trajectory clustering

To characterize the age-related dynamics of multi-omics features, we applied generalized additive models (GAMs) to each dataset with the mgcv package (version 1.8.42). For each omic layer (phenome, transcriptome, proteome, metabolome, and metagenome), we first preprocessed and filtered to ensure valid age annotations and to remove excluded samples. GAM fitting was conducted separately for all individuals and stratified by sex (male and female).

For each feature, a GAM was fitted using the mgcv R package with the model formula feature $\sim$ s(age), where s(age) represents a smooth spline term. The model was fitted under a scaled t-distribution (scat family) to accommodate potential non-Gaussian residuals. From the fitted models, we extracted the estimated degrees of freedom (edf), p-values, and adjusted p-values (Benjamini-Hochberg correction). Features with adjusted P value < 0.01 and edf > 3 were retained as significantly nonlinear age-associated features.

For each retained feature, predicted values across the age range were generated, and z-score normalized across features to construct a scaled feature–age matrix. Predicted trajectories were then concatenated across all omics layers to obtain an integrated multi-omics age–feature matrix.

This matrix was subjected to unsupervised clustering using hierarchical clustering with k-means partitioning (k = 5-10). The optimal clustering resolution was selected based on interpretability and robustness of the clusters. Clusters were manually grouped into biologically meaningful trajectory types based on the temporal patterns (see Table S3 for details).

Organ-associated aging clock construction

First, organ-associated proteins were identified from human organ proteome data,[77,78] which were defined as proteins with an expression level at least 10-fold higher in a specific organ compared to any other organ. These proteins were cross-referenced with the plasma proteome to identify plasma-detectable organ-associated proteins. These proteins, together with phenotypic and imaging data, were used as input for constructing the organ Multi-Modal clock. An ElasticNet regression model was used to construct the multimodal organ Multi-Modal clock. The dataset was split into two parts: 50% for model training and 50% for validation. Feature importance was evaluated as described above (see Table S2 for details).

Fluctuation wave analysis of aging-associated clinical indicators and proteins

DE-swan (Differential Expression - Sliding Window Analysis, version 0.0.0.9001) algorithm was used to identify temporal inflection points at the molecular level during the aging process.[141] DE-swan algorithm detects non-linear changes by comparing molecular levels between groups of individuals within specific age windows. Specifically, a window width of 5-years was employed. Within each window, the Wilcoxon rank-sum test was utilized to compare molecular levels between individuals younger and older than the center age, thereby assessing differential expression. To ensure adequate sample sizes for statistical analysis, the evaluated center ages ranged from 25 to 80 years, and the windows were shifted in 5-year increments. P values were adjust using the Benjamini-Hochberg method.

Proxy clock construction

The construction of the multimodal proxy clock employed a strategy similar to that described as above, distinguished by using the previously obtained multimodal age as the target rather than chronological age. The original clock training set was repartitioned into training and testing sets for the proxy clock at a 1:1 ratio. The model was trained using the glmnet R package (version 4.1.4) with alpha set to 0.1-0.9.[127] Ten-fold cross-validation was applied on the training set to determine the optimal lambda value. The model with the smallest mean absolute error (MAE) in the validation set was selected as the final model. Feature importance was evaluated as described above (see Table S2 for details).

Fast ager and slow ager classification

To classify the fast agers and slow agers, we calculated the age pace of all aging clocks for each volunteer. A linear regression model was built using chronological and predicted age, and the residual between the predicted age and the regressed value of chronological age was defined as the age pace. The "rcorr" function from the R package Hmisc (version 5.2.2) was used to calculate the correlation between age paces generated by different age estimators.

The fast agers and slow agers were then defined as the top and bottom 20% of age pace for each aging clock. Representative fast agers and slow agers were further defined using Δclock, defined as the difference between the number of times an individual was classified as a fast ager and the number of times as a slow ager across all clocks. Individuals with $|\Delta\text{clocks}| \geq 3$ were considered high-confidence representatives.

AA- and DA-related lifestyle identification

At recruitment, participants completed a self-administered questionnaire that included instruments to measure illness burden and lifestyle factors. To evaluate the risk of lifestyle factors for the outcome of accelerating aging, we used binary logistic regression modeling to calculate the odds ratios for the likelihood of fast agers or slow agers by lifestyle factor, adjusting for age and sex. The lifestyle factors with an odds ratio (OR) greater than 1 and a P value less than 0.05 were considered as AA-related lifestyles. The lifestyle factors with an OR value less than 1 and a P value less than 0.05 were considered as DA-related lifestyles (see Table S4 for details).

Clinical and proteomic characterization of fast and slow agers

To characterize clinical parameters in fast and slow agers, we used binary logistic regression to estimate odds ratios for the likelihood of being a fast or slow ager for each clinical parameter, adjusting for age and sex. Clinical measurements with OR > 1 and BH-adjusted P < 0.05 were considered AA-related clinical parameters, and clinical parameters with OR < 1 and BH-adjusted P < 0.05 were considered DA-related.

To detect AA- and DA-related proteins, partial correlation between age pace and protein expression levels was calculated, adjusting for age. Proteins with a partial correlation coefficient > 0 and a BH-adjusted P < 0.05 were considered as AA-related proteins, and those with a coefficient < 0 and a BH-adjusted P < 0.05 were considered as DA-related proteins (see Table S5 for details).

Mendelian randomization analysis

To detect significant causal associations between age-associated AA- or DA-related proteins and diseases, the genomic associations were further explored using protein-disease MR analysis.[168] For genetic instruments in MR analysis, well-collected protein quantitative trait loci (pQTLs) data were obtained from previous studies.[169] For genetic outcomes in MR analysis, 6640 high-quality disease genome-wide association studies (GWAS) were downloaded from the DMRdb database.[170] The Wald ratio was used to estimate MR effects if only a single instrument was available, and the inverse variance weighted (IVW) method was used if two or more instruments were available. The TwoSampleMR R package (version 0.6.9) was used to conduct Mendelian randomization analysis.[142,171] The protein-disease associations with a BH-adjusted P < 0.05 and an OR > 1 were considered as positively causal protein-disease pairs.

Age-accumulated coagulation factor score calculation

To quantify individual-level coagulation activity in an age-weighted manner, we constructed an age-accumulated coagulation factor score based on five coagulation-accumulated proteins (F5, F7, F8, F9, and F13B). Protein expression data were extracted and combined with the corresponding Spearman's correlation coefficients derived from age-association analysis. Each individual's score was calculated as the weighted sum of protein expression values, each multiplied by its age correlation coefficient.

To correct for confounding factors, linear model residuals were obtained, and individuals were stratified into three groups based on residual values: High (> 0.5), Low (< –0.5), and Normal (between –0.5 and 0.5). For downstream comparisons, we constructed a balanced analysis cohort by matching the sample size of the High group with an equal number of individuals from the Normal group, stratified by sex. These individuals were combined with all individuals in the high-score group to construct the final cohort used in downstream phenotypic and molecular comparisons.

Supplemental figures

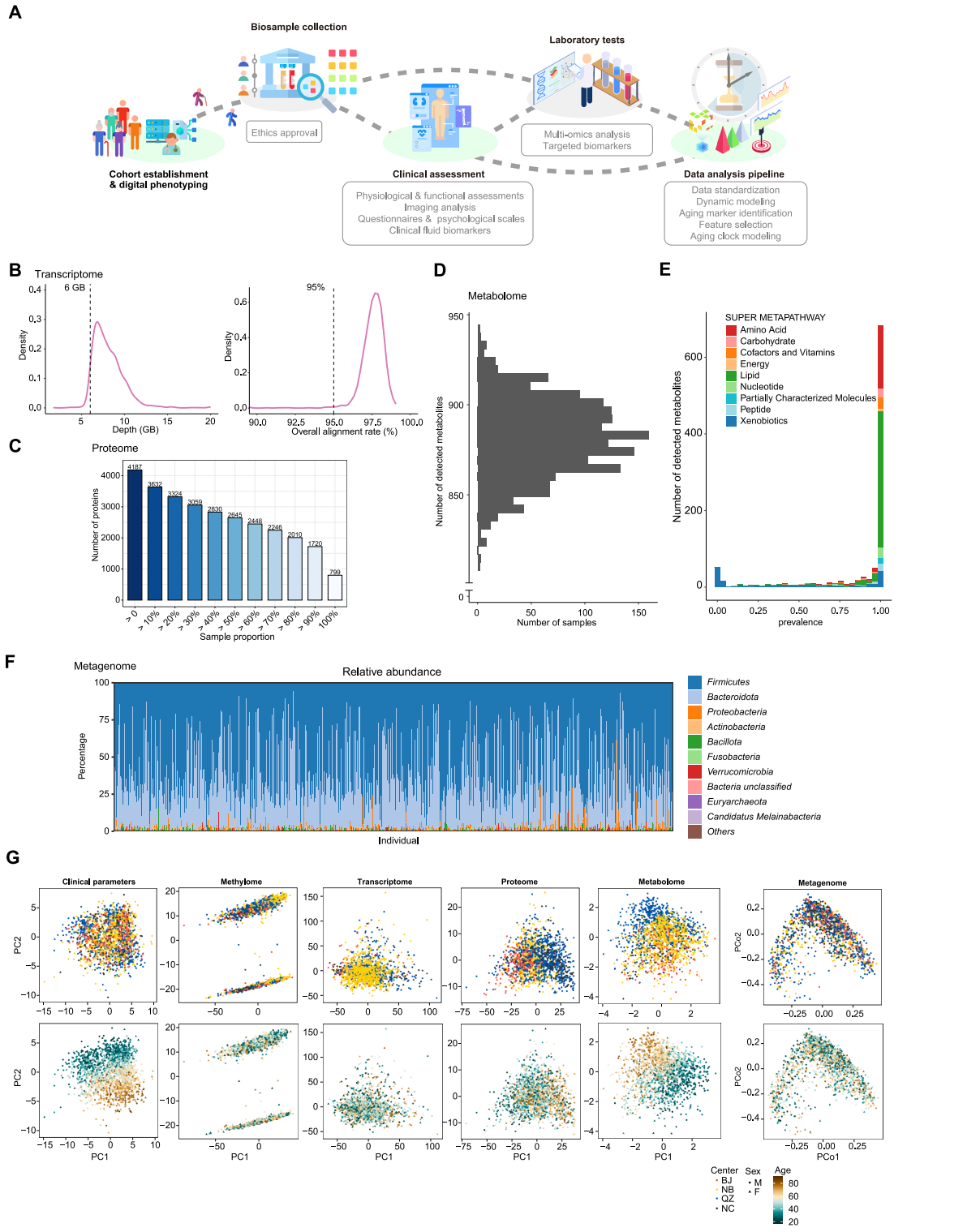

(legend on next page)

Figure S1. Cohort overview and multi-omics data quality control, related to Figure 1

(A) Schematic flow chart showing the procedures of volunteer recruitment.

(B) Density plots showing the sequencing depth and alignment rate of bulk RNA-seq data.

(C) Proteomic data coverage showing the number of proteins retained at different sample prevalence thresholds.

(D) Distribution of detected metabolites across samples in the metabolomic dataset.

(E) Prevalence distribution of metabolite detection across samples, grouped by superclass taxonomy.

(F) Composition of the gut metagenome across samples, illustrated by the relative abundance of dominant phyla.

(G) Principal-component analysis (PCA) of five omics layers: clinical parameters, methylome, transcriptome, proteome, and metabolome, and principal-coordinates analysis (PCoA) of metagenome data based on the Bray-Curtis distance. The first two PCs are shown, colored by center (top row) and age and sex (bottom row).

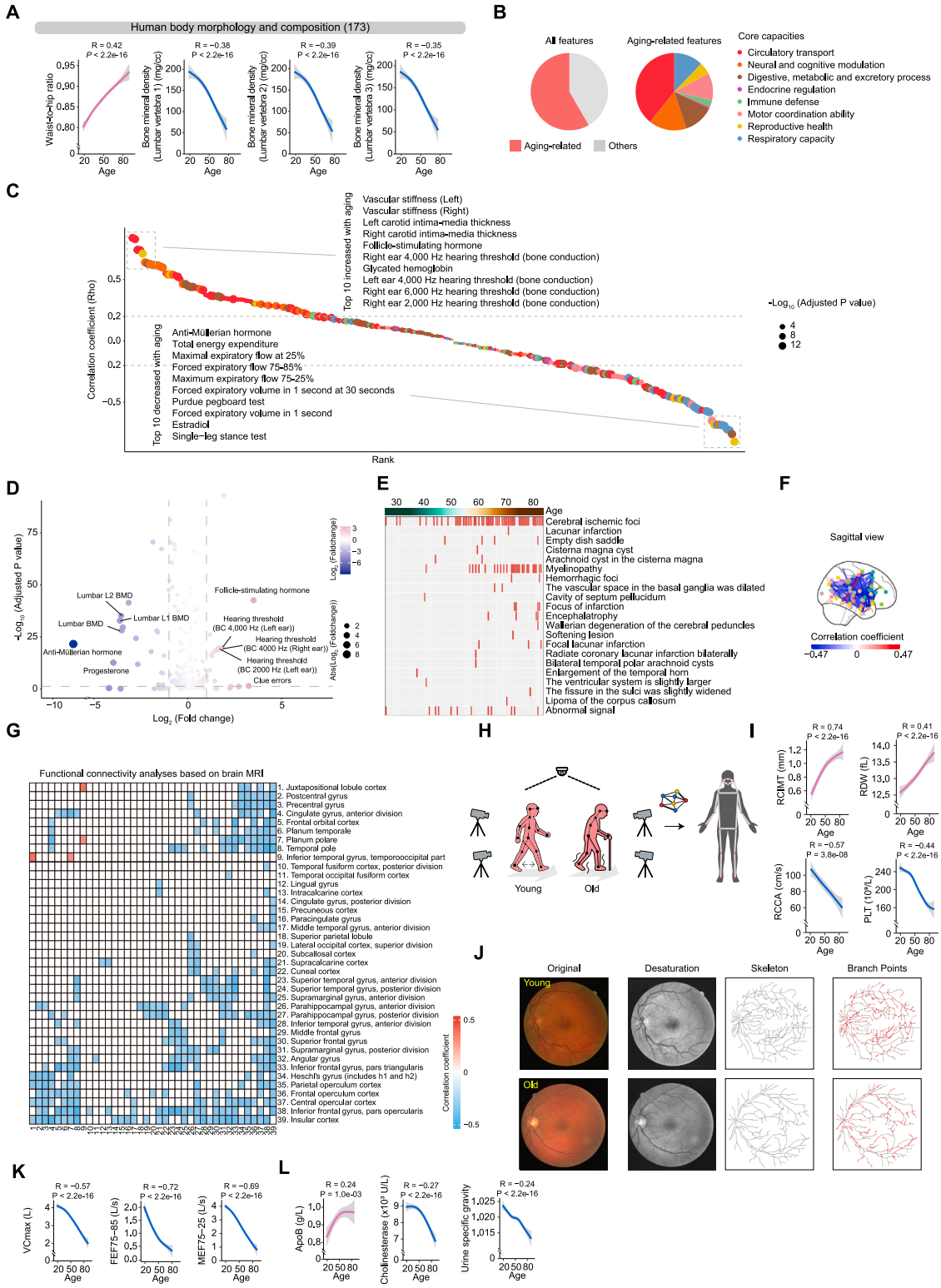

Figure S2. Comprehensive age-related changes in core physiological parameters, related to Figure 2

(A) Curve graphs showing the increased waist-to-hip ratio and decreased bone mineral density changes during aging, including lumbar vertebra 1, 2, and 3.

(B) Pie charts showing the age-related proportion of the core capabilities parameters from human body physiological modules (top), and the ratio of age-related core capabilities parameters and their classes (bottom).

(legend continued on next page)

(C) Dot plot showing the Spearman's correlation of 240 core capabilities parameters from human body physiological modules with aging. The dashed line indicates the thresholds of the age-related features.
(D) Dot plot showing the core capabilities parameters of the increase (pink) and decrease (blue) in the elderly. The dashed line indicates the thresholds of the aging-related differences.
(E) Heatmap showing the brain-related diseases diagnosed clinically. The color bar, from green to brown, indicates age from young to old.
(F) The correlation between the strength of functional connectivity groups (sagittal plane) in different brain regions with aging. The color bar, from blue to red, indicates the correlation coefficient between functional connectivity and age.
(G) Heatmap showing the characteristics of functional connectivity groups in different brain regions that change with age. The color bar from blue to red indicates the relationship between functional connectivity and aging.
(H) Schematic diagram showing the synchronous collection of walking features from multiple angles.
(I) The curve graphs showing the characteristics of the circulatory transport module changing with age. RCIMT, right carotid intima-media thickness; RCCA, right common carotid artery diameter; PLT, platelet count; RDW, red blood cell volume distribution width.
(J) Representative diagrams showing the distribution of retinal blood vessels in the young and the old.
(K) Curve graphs showing decreased lung function with age. The maximum vital capacity (VC_{max}), forced expiratory flow at 75%–85% of vital capacity (FEF75–85), and maximum mid-expiratory flow at 75%–25% of vital capacity (MEF75–25) decrease with age.
(L) Curve graphs showing the characteristics of changes in blood and urine components with age. Blood lipid (ApoB) increases with age, while liver function (cholinesterase) decreases with age. Urine specific gravity decreased with age.
For curve plots showing a single-feature value, Spearman's rank correlation coefficient (rho) and adjusted *p* value were indicated. Benjamini-Hochberg was used to calculate the adjusted *p* value. The trend lines (red, increased with age; blue, decreased with age) represent the generalized additive model fits obtained from the scatter plot, with a shaded 95% confidence interval band.

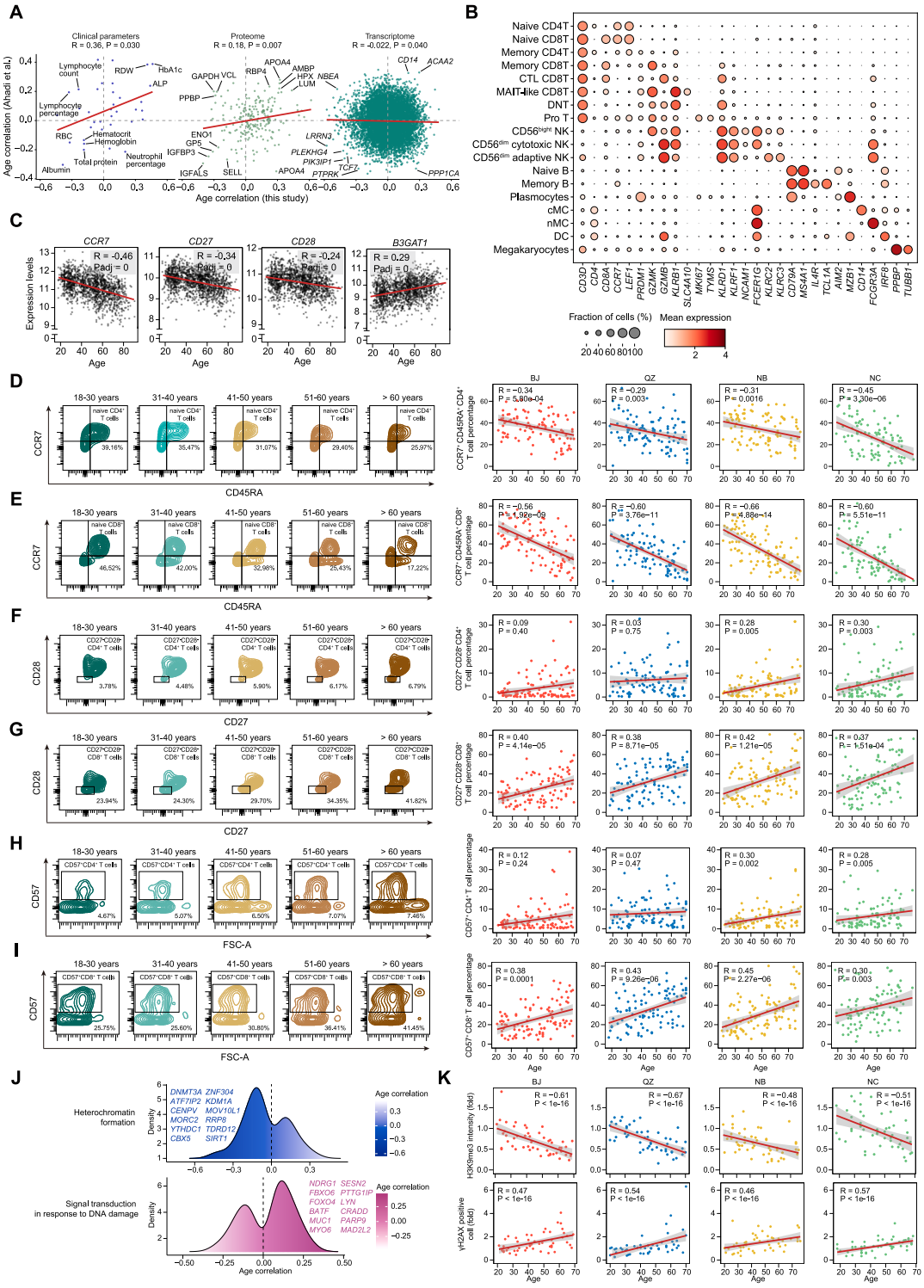

Figure S3. Multi-omics age-related features and validation across centers, related to Figure 3

(A) Point plot showing the age correlation between this study (*x* axis) and the study of Ahadi et al.[53] (*y* axis) in phenome, proteome, and transcriptome. The top features were denoted. Red lines represent the linear fitting results.

(B) Dot plot showing the expression of marker genes for different cell types in scRNA-seq data.

(C) Correlation between age and the indicated genes in PBMCs detected with bulk RNA-seq. Correlation coefficients and *p* values (Spearman's correlation) are denoted. Red lines represent the linear fitting results.

(legend continued on next page)

(D) Representative flow cytometry plots showing the age-related decline in the proportion of naive $CD4^+$ T cells among total $CD4^+$ T cells in PBMCs (left). naive $CD4^+$ T cells, $CD3^+CD4^+CCR7^+CD45RA^+$; changing proportions of naive $CD4^+$ T cells with aging in four research centers (right). n = 99 individuals in BJ center, 100 individuals in QZ center, 100 individuals in NB center, and 98 individuals in NC center. Correlation coefficients (Spearman's correlation) are denoted.
(E) Representative flow cytometry plots showing the age-related decline in the proportion of naive $CD8^+$ T cells among total $CD8^+$ T cells in PBMCs (left). naive $CD8^+$ T cells, $CD3^+CD8^+CCR7^+CD45RA^+$; changing proportions of naive $CD8^+$ T cells with aging in four research centers (right). n = 99 individuals in BJ center, 100 individuals in QZ center, 100 individuals in NB center, and 98 individuals in NC center. Correlation coefficients and p values (Spearman's correlation) are denoted. Red lines represent the linear fitting results.
(F) Representative flow cytometry plots showing the age-related increase in the proportion of $CD27^-CD28^-CD4^+$ T cells among total $CD4^+$ T cells in PBMCs (left). Changing proportions of $CD27^-CD28^-CD4^+$ T cells with aging in four research centers (right). n = 99 individuals in BJ center, 100 individuals in QZ center, 100 individuals in NB center, and 98 individuals in NC center. Correlation coefficients and p values (Spearman's correlation) are denoted. Red lines represent the linear fitting results.
(G) Representative flow cytometry plots showing the age-related increase in the proportion of $CD27^-CD28^-CD8^+$ T cells among total $CD8^+$ T cells in PBMCs (left). Changing proportions of $CD27^-CD28^-CD8^+$ T cells with aging in four research centers (right). n = 99 individuals in BJ center, 100 individuals in QZ center, 100 individuals in NB center, and 98 individuals in NC center. Correlation coefficients and p values (Spearman's correlation) are denoted. Red lines represent the linear fitting results.
(H) Representative flow cytometry plots showing the age-related increase in the proportion of $CD57^+CD4^+$ T cells among total $CD4^+$ T cells in PBMCs (left). Changing proportions of $CD57^+CD4^+$ T cells with aging in four research centers (right). n = 99 individuals in BJ center, 100 individuals in QZ center, 100 individuals in NB center, and 98 individuals in NC center. Correlation coefficients and p values (Spearman's correlation) are denoted. Red lines represent the linear fitting results.
(I) Representative flow cytometry plots showing the age-related increase in the proportion of $CD57^+CD8^+$ T cells among total $CD8^+$ T cells in PBMCs (left). Changing proportions of $CD57^+CD8^+$ T cells with aging in four research centers (right). n = 99 individuals in BJ center, 100 individuals in QZ center, 100 individuals in NB center, and 98 individuals in NC center. Correlation coefficients and p values (Spearman's correlation) are denoted. Red lines represent the linear fitting results.
(J) Distribution of age correlation of genes related to heterochromatin formation and signal transduction in response to DNA damage.
(K) Quantitative data showing the mean fluorescence intensity of H3K9me3 and the percentage of γH2AX-positive cells in human PBMCs from BJ, QZ, NB, and NC centers. n = 50 per center. Correlation coefficients and p values (Spearman's correlation) are denoted. Red lines represent the linear fitting results.

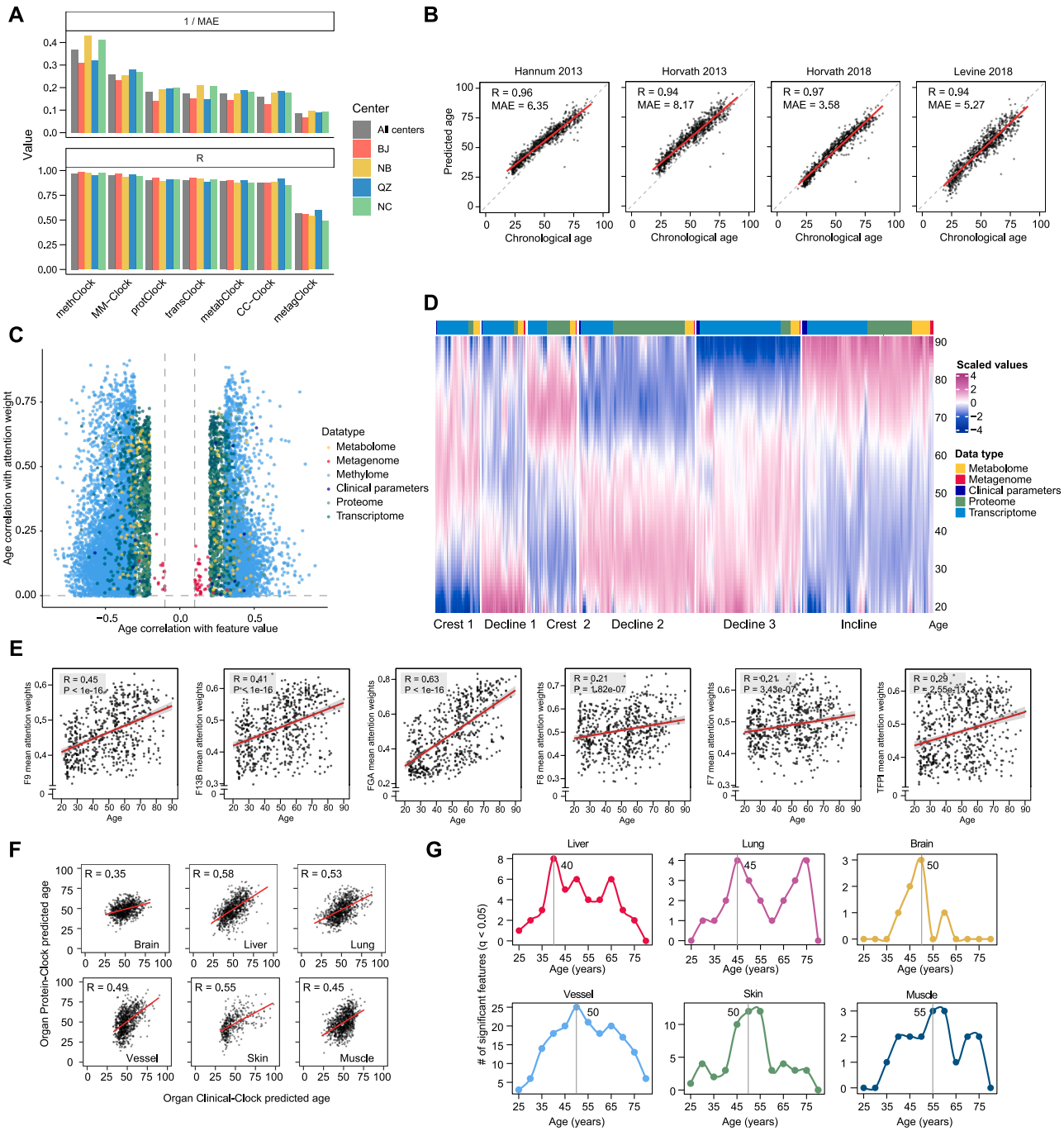

Figure S4. MM-clock performance and aging trajectory analysis, related to Figures 4 and 5

(A) Comparison of prediction performance across different aging clocks in all-center and single-center settings. (Top) Inverse of mean absolute error (1/MAE). (Bottom) Pearson correlation coefficient (R) between predicted and chronological age.

(B) Dot plot showing the correlation between biological age and chronological age based on the published aging clock, including Hannum et al.[69], Horvath[70], Horvath et al.,[71] and Levine et al.[72] Correlation coefficients (Pearson's correlation) and MAE are denoted. Red lines represent the linear fitting results.

(C) Point plot showing the attention weight of features in MM-clock and their correlation with age.

(D) Heatmap showing scaled predicted values of age-associated features across five omics layers, ordered and grouped into six distinct aging trajectory clusters. Each row represents a feature, and each column represents age. Colors indicate the scaled value (blue, low; pink, high).

(E) Point plots showing the attention weights for coagulation-factor proteins in MM-clock. Correlation coefficients (Pearson's correlation) and MAE are denoted. Red lines represent the linear fitting results.

(legend continued on next page)

(F) Point plots showing the linear relationship between organ clinical-clock and organ protein-clock. Correlation coefficients and MAE are denoted. Red lines represent the linear fitting results.
(G) Waves in differentially expressed clinical parameters and protein quantities across different organs with age. The gray line indicates the age corresponding to the inflection point of aging-related feature changes.

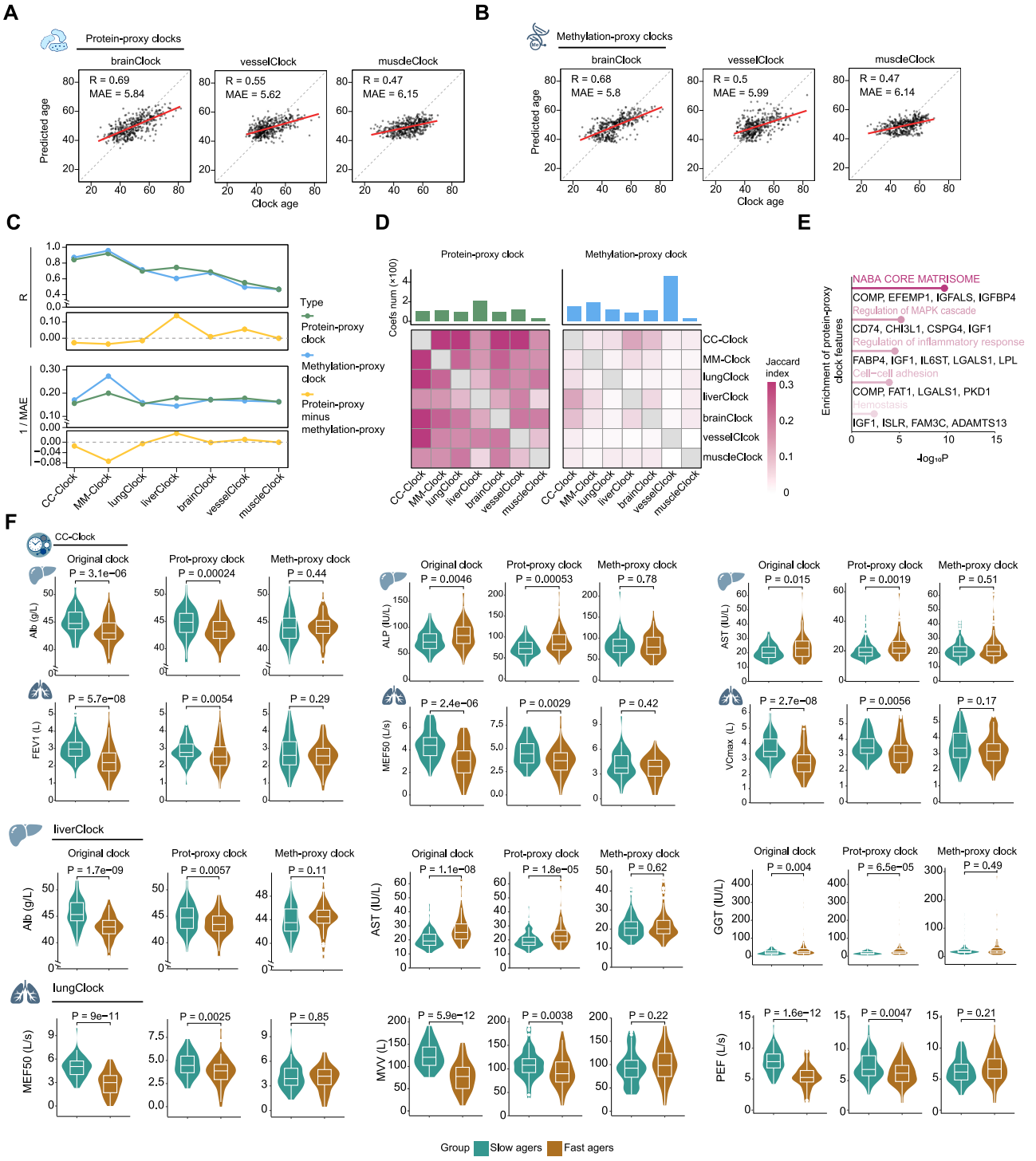

Figure S5. Proxy clock performance and feature analysis, related to Figure 5

(A) Scatterplots showing the predicted age of the age estimators and their linear relationship with original clock age and predicted age by protein data. Linear fits are indicated by the red line. Correlation coefficients (Pearson's correlation analysis) and MAE are shown.

(B) Scatterplot showing the predicted age of the age estimators and their linear relationship with original clock age and predicted age by DNA methylation data. Linear fits are indicated by the red line. Correlation coefficients (Pearson's correlation analysis) and MAE are shown.

(legend continued on next page)

(C) Line charts illustrating the correlation coefficients (Pearson's correlation analysis) (top) and 1/MAE values (bottom) of different proxy clocks, and the difference between protein-proxy clocks and methylation-proxy clocks with different colors representing various omics layers.
(D) Bar plots showing the number of features used by different proxy clocks (top). Heatmap illustrating the similarity between proxy clock features, with the color intensity representing the Jaccard index values (bottom).
(E) Bar plots showing enriched pathways of protein-proxy clock-related proteins.
(F) Violin plots showing the phenotypic differences between the population with AA and the population with DA for CC-clock, liverClock, and lungClock.

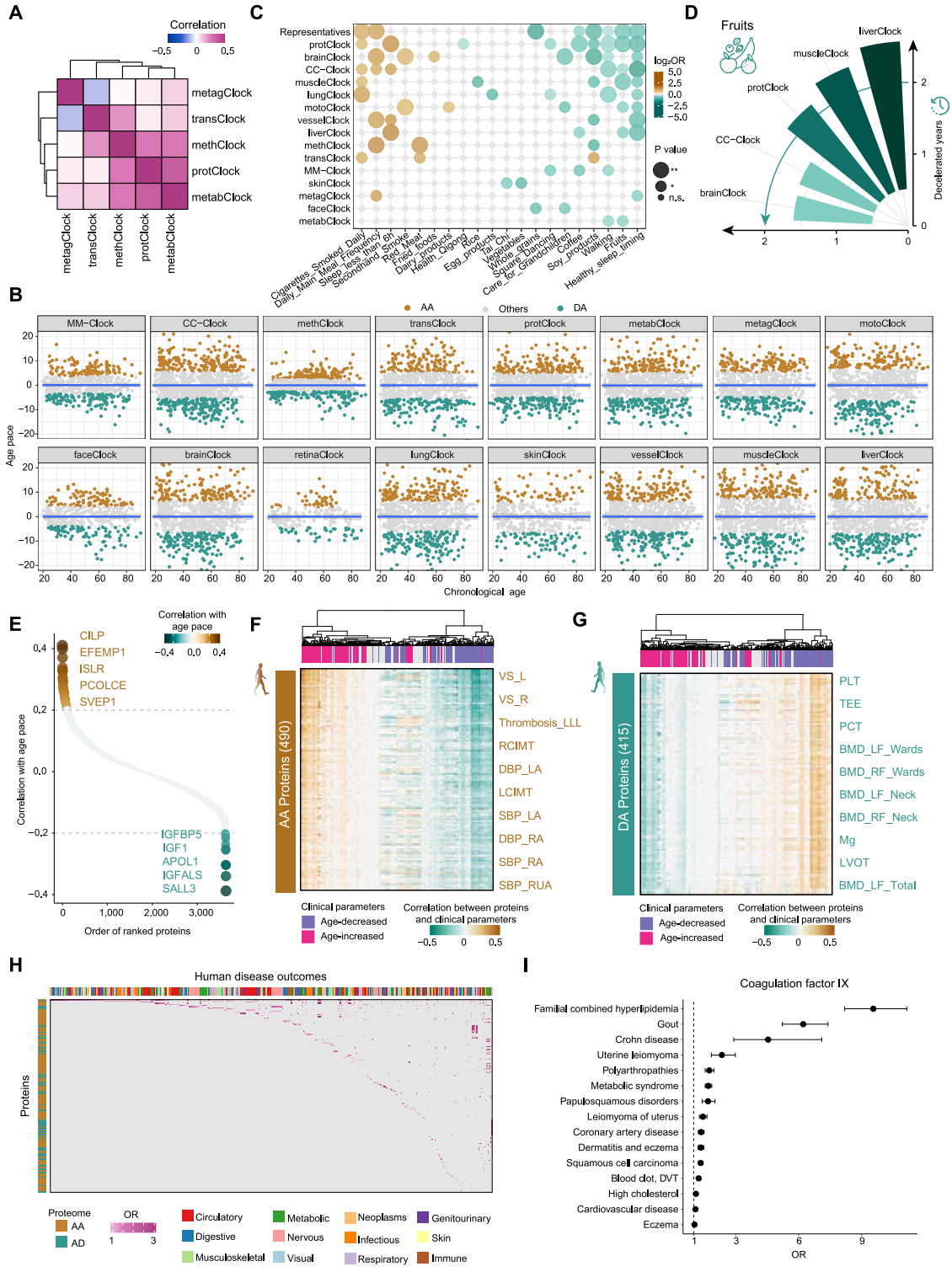

Figure S6. Proteomic signatures of accelerated and decelerated aging, related to Figure 6

(A) Correlation analysis based on age pace for micro-clocks. The color key, from dark blue to dark purple, shows the correlation from low to high.

(B) Dot plots showing the distribution of fast agers and slow agers for the indicated aging clocks. The green and brown dots indicate fast agers and slow agers, respectively.

(C) Dot plots showing the DA-related lifestyles were identified using logistic regression, adjusted for age and sex for each clock.

(D) Bar plot showing the decelerated years by individuals who often eat fruits for the indicated aging clocks.

(legend continued on next page)

(E) Dot plots showing the AA-related proteins and DA-related proteins identified by partial correlation. The green and brown dots indicate negative and positive correlation with age pace.
(F) Heatmap showing the relationship between AA-related proteins and clinical parameters. The color key from green to brown showing the correlation from negative to positive.
(G) Heatmap showing the relationship between DA-related proteins and clinical parameters. The color key from green to brown showing the correlation from negative to positive.
(H) Heatmap showing the positive causal associations between disease outcomes for age-associated AA-/DA-related proteins identified using Mendelian randomization analysis.
(I) Forest plot illustrating the significant associations between coagulation-factor IX (F9) and various diseases based on Mendelian randomization analysis. The dots present the OR, and horizontal bars present the confidence intervals.

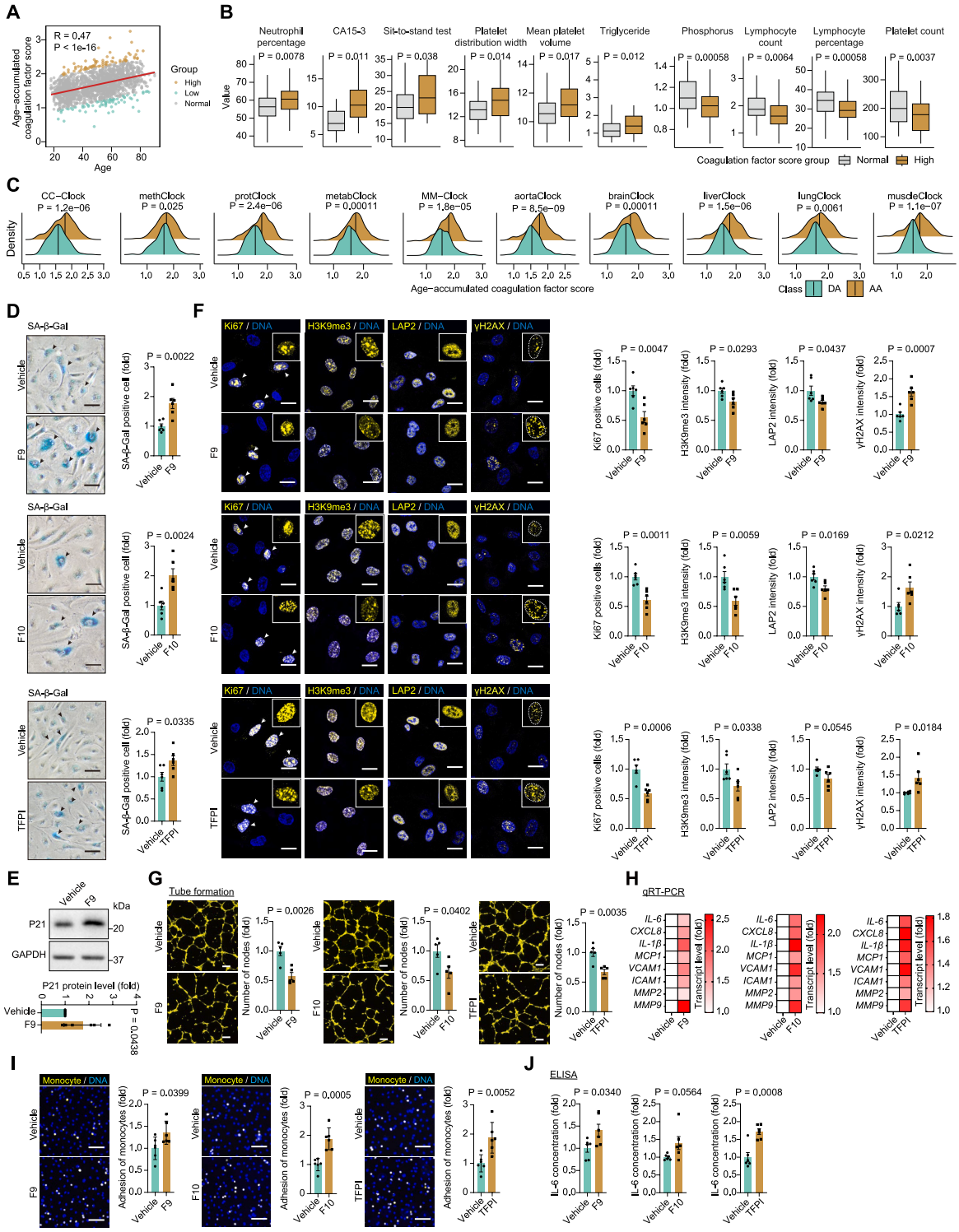

Figure S7. Coagulation factors induce endothelial cell senescence, related to Figure 7

(A) Point plot showing the age-accumulated coagulation-factor score and its relationship with age. Colors of the points indicate the score group. Red lines represent the linear fitting results.

(B) Clinical measurements with significant differences between normal and high-coagulation-factor-score groups.

(C) Density plots showing the age-accumulated coagulation-factor score between AA and DA groups. *n* = 39 individuals per group. The lines indicate the median values.

(legend continued on next page)

(D) SA-β-Gal staining of HAECs treated with F9, F10, or TFPI. *n* = 6 independent experiments. Scale bars, 50 μm.
(E) Western blot analysis of P21 expression in HAECs treated with F9. GAPDH was used as a loading control. *n* = 6 independent experiments.
(F) IF staining analysis of Ki67, H3K9me3, LAP2, and γH2AX in HAECs treated with F9, F10, or TFPI. *n* = 6 independent experiments. Scale bars, 20 μm.
(G) Tube formation analysis of HAECs treated with F9, F10, or TFPI. *n* = 5 independent experiments. Scale bars, 200 μm.
(H) RT-qPCR analysis of SASP-related genes in HAECs treated with F9, F10, or TFPI. *n* = 3 independent experiments.
(I) Monocyte adhesion ability analysis of HAECs treated with F9, F10, or TFPI. *n* = 6 independent experiments. Scale bars, 100 μm.
(J) ELISA analysis of IL-6 expression in cell culture supernatant of HAECs treated with F9 or TFPI. *n* = 6 independent experiments.
For (A), data were analyzed with Spearman's correlation. For (B) and (C), P values were calculated with the Wilcoxon rank-sum test. For (D)–(L), P values were calculated with a two-tailed unpaired Student's *t* test, and data are presented as means ± SEM.

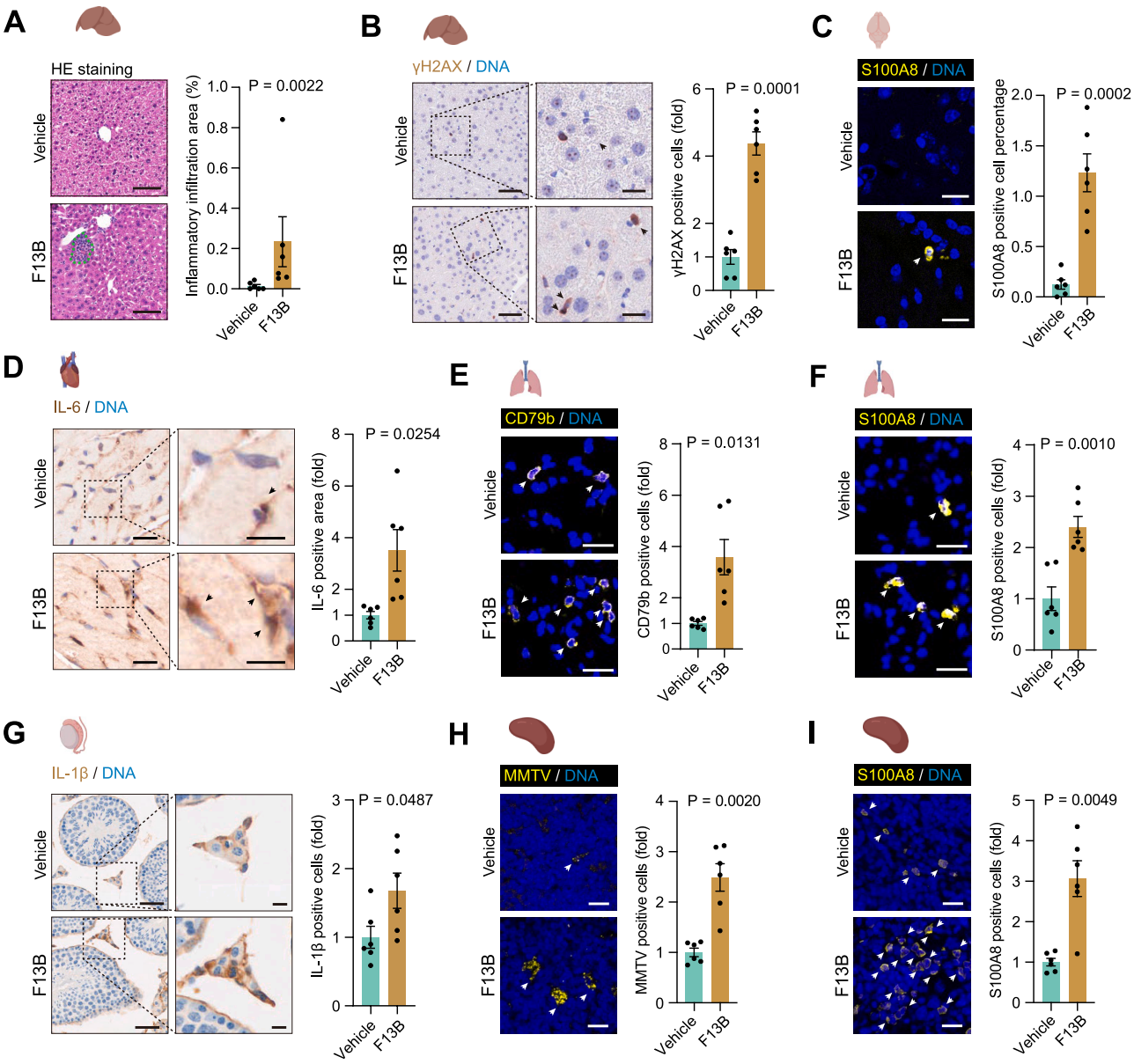

Figure S8. F13B promotes multi-organ senescence and inflammation *in vivo*, related to Figure 7

(A) HE staining analysis of mouse liver tissues. Scale bars, 100 μm.
(B) IHC staining analysis of γH2AX in mouse liver tissues. Scale bars, 60 and 20 μm.
(C) IF staining analysis of S100A8 in mouse brain tissues. Scale bars, 20 μm.
(D) IHC staining analysis of IL-6 in mouse heart tissues. Scale bars, 20 and 10 μm.
(E) IF staining analysis of CD79b in mouse lung tissues. Scale bars, 20 μm.
(F) IF staining analysis of S100A8 in mouse lung tissues. Scale bars, 20 μm.
(G) IHC staining analysis of IL-1β in mouse testis tissues. Scale bars, 50 and 10 μm.
(H) IF staining analysis of MMTV in mouse spleen tissues. Scale bars, 20 μm.
(I) IF staining analysis of S100A8 in mouse spleen tissues. Scale bars, 20 μm.
Data are presented as means ± SEM. Statistical analyses were performed using two-tailed unpaired Student's *t* test (B, F, and G) or two-tailed unpaired Welch's *t* test (C–E, H, and I) or two-tailed unpaired Wilcoxon test (A). *n* = 6 mice.